COASTAL EVOLUTION MODEL

Scripps Institution of Oceanography Technical Report No. 58

Submitted by:
Scott A. Jenkins and Joseph Wasyl
Marine Physical Laboratory
Scripps Institution of Oceanography

Submitted to:
Directors Office
Scripps Institution of Oceanography

30 NOVEMBER 2005

Sponsored by The Kavli Institute, Santa Barbara, CA 93101

ACKNOWLEDGEMENT:

This report documents the CEM computer code development performed by the authors under sponsorship of the Kavli Institute over the period February 2002 to 15 April 2005. This documentation was developed from our working notes. We acknowledge the contributions of Douglas L. Inman and Patricia Masters to many of the graphics and some of the text presented herein. We also thank Gerald D'Spain for his encouragement to complete this report.

TABLE OF CONTENTS:

TABLE OF CONTENTS (continued):

1. General Description of Architecture of the Coastal Evolution Model (CEM)

Here, we describe the basic architecture of a 3-dimensional coastal evolution model developed under funding from the Kavli Institute. The Coastal Evolution Model (CEM) is a process-based numerical model. It consists of a Littoral Cell Model (LCM) and a Bedrock Cutting Model (BCM), both coupled and operating in varying time and space domains (Figure 1) determined by sea level and the coastal boundaries of the littoral cell at that particular sea level and time. At any given sea level and time, the LCM accounts for erosion of uplands by rainfall and the transport of mobile sediment along the coast by waves and currents, while the BCM accounts for the cutting of bedrock by wave action in the absence of a sedimentary cover. During stillstands in sea level, the combined effect of bottom erosion under breaking waves and cliffing by wave runup carves the distinctive notch in the shelf rock known as a wave-cut terrace (Figure 2).

In both the LCM and BCM, the coastline of the littoral cell is divided into a series of coupled control cells (Figure 3). Each control cell is a small coastal unit of uniform geometry where a balance is obtained between shoreline change and the inputs and outputs of mass and momentum. The model sequentially integrates over the control cells in a down-drift direction so that the shoreline response of each cell is dependent on the exchanges of mass and momentum between cells, giving continuity of coastal form in the down-drift direction. Although the overall computational domain of the littoral cell remains constant throughout time, there is a different coastline position at each time step in sea level. For each coastline position there exists a similar set of coupled control cells that respond to forcing by waves and current. Time and space scales used for wave forcing and shoreline

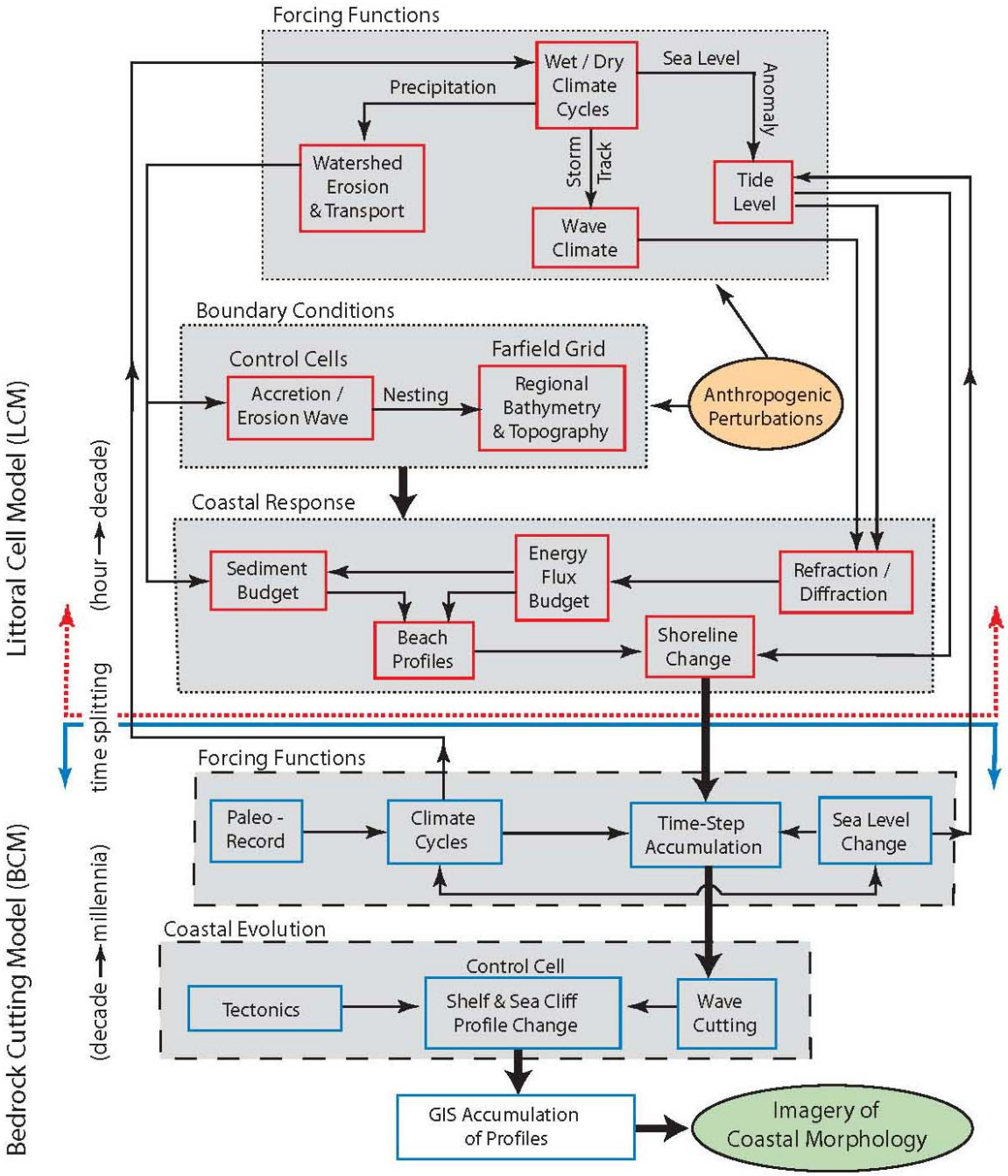

Figure 1. Architecture of the Coastal Evolution Model consisting of the Littoral Cell Model (above) and the Bedrock Cutting Model (below). Modules (shaded areas) are formed of coupled primitive process models.

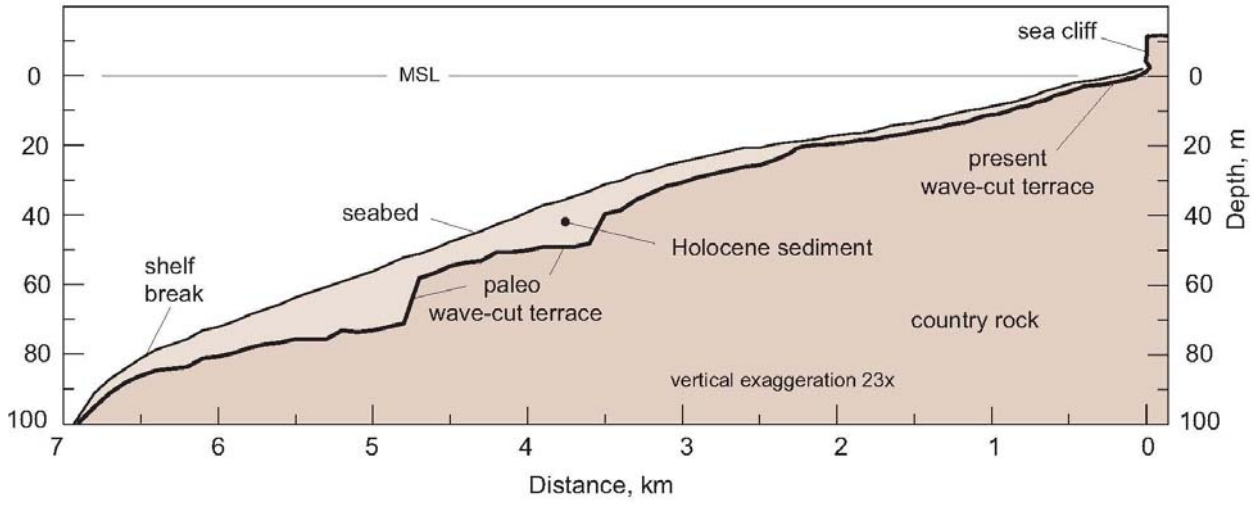

Figure 2. Generalized seismic profile relative to present mean sea sevel (MSL) across the continental shelf of the northern part of the Oceanside littoral cell.

response (applied at 6 hour intervals) and sea level change (applied annually) are very different. To accommodate these different scales, the model uses multiple nesting in space and time, providing small length scales inside large, and short time scales repeated inside of long time scales.

The LCM (Figure 1, upper) has been used to predict the change in shoreline width and beach profile resulting from the longshore transport of sand by wave action where sand source is from river runoff or from tidal exchange at inlets (e.g., Jenkins and Inman, 1999). More recently it has been used to compute the sand level change (farfield effect) in the prediction of mine burial (Jenkins and Inman, 2002; Inman and Jenkins, 2002). Time-splitting logic and feedback loops for

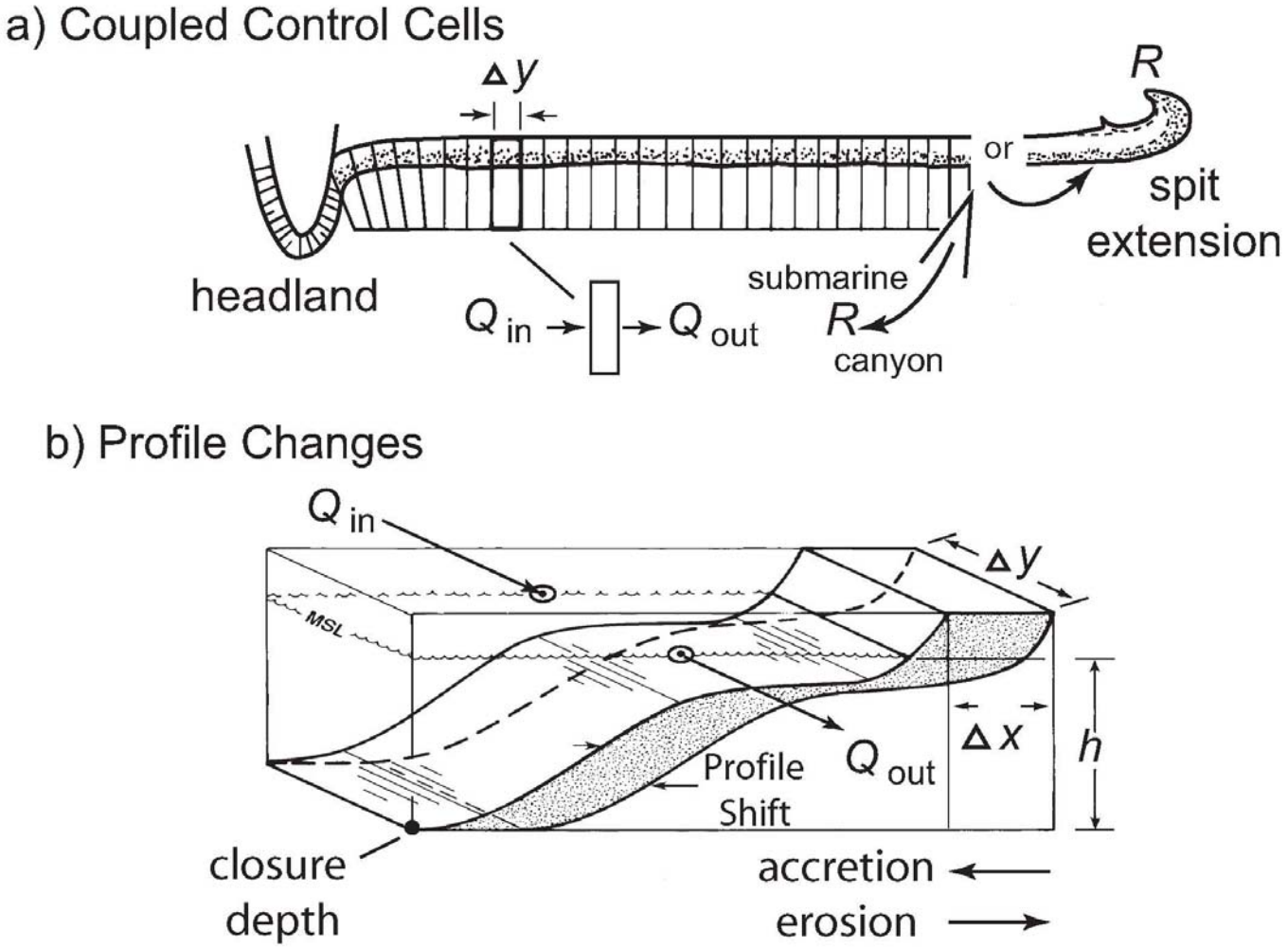

Figure 3: Computational approach for modeling shoreline change [after Inman et al., 2002].

climate cycles and sea level change were added to the LCM together with long run time capability to give a numerically stable couple with the BCM.

The BCM (Figure 1, lower) is a new effort to model the erosion of country rock by wave action during transgressions, regressions, and stillstands in sea level. Because bedrock cutting requires the near absence of a sediment cover, the boundary conditions for cutting are determined by the coupled mobile sediment model, LCM. When LCM indicates that the sediment cover is absent in a given area, then BCM kicks in and begins cutting. BCM cutting is powered by the wave climate input to LCM but applied only to areas where mobile sediment is absent. Bedrock cutting involves the action of wave energy flux *ECn* to perform the work required to abrade and notch the country rock. Both abrasion and notching mechanisms are computed by the newly developed wave-cutting algorithms. These algorithms use a general solution for the recession *R* (in meters) of the shelf and sea cliff. The recession rate dR/dt is a function of the incident wave energy flux,

$$\frac{dR}{dt} = \frac{\rho}{\rho_S} f_e \, ECn \qquad (1)$$

where ρ is the density of seawater; ρ_s is the density of the bedrock, and f_e is a function that varies from 0 to 1 and is referred to as the erodibility. The units of the erodibility are the reciprocal of the wave force per unit crest length (m/N). The erodibility is given separate functional dependence on wave height for the platform abrasion and wave notching of the sea cliff. For abrasion, the erodibility varies with the local shoaling wave height $H_{(x)}$ as

$$f_e = K_a q_{ij} \, H_{(x)}^{1.63} \quad \text{(abrasion)} \qquad (2)$$

where q_{ij} is the bedrock failure shape function and K_a is an empirical constant. Consequently, recession by abrasion is a maximum at the wave breakpoint (at a depth of about 5/4 the breaking wave height, H_b) and decreases in both the seaward and shoreward directions. In contrast, the erodibility of the notching mechanism is a force-yield relation associated with the shock pressure of the bore striking the sea cliff (Bagnold, 1939; Trenhaile, 2002). The shock pressure is proportional to the runup velocity squared, which is limited by wave runup elevation. Wave pressure solutions (Havelock, 1940) give

$$f_e = K_n q_{ij} \eta_r^2 \text{ (notching)} \quad (3)$$

where K_n is an empirical constant and the runup elevation η_r is dependent on the tidal level η_o and the breaking wave height by Hunt's formula,

$$\eta_r = \eta_o + \Gamma H_b \quad (4)$$

Here Γ is an empirical constant from Hunt's formula (*Hunt*, 1959).

1.1 Sea Level and Paleoclimate

The position of the paleocoastline changed from near the present 50 m depth contour to the position of the modern coastline over the span of 12,000 years. Mean sea level (Figure 4) becomes the moving surface where forcing by waves, tides, and weather operates. The model addresses sequential time intervals over the past 12,000 years (Holocene) forward to the present and 200 years into the future. The rate of sea level rise varied widely since the last glaciation with three known periods of stillstand, one associated with the Younger Dryas cold climate

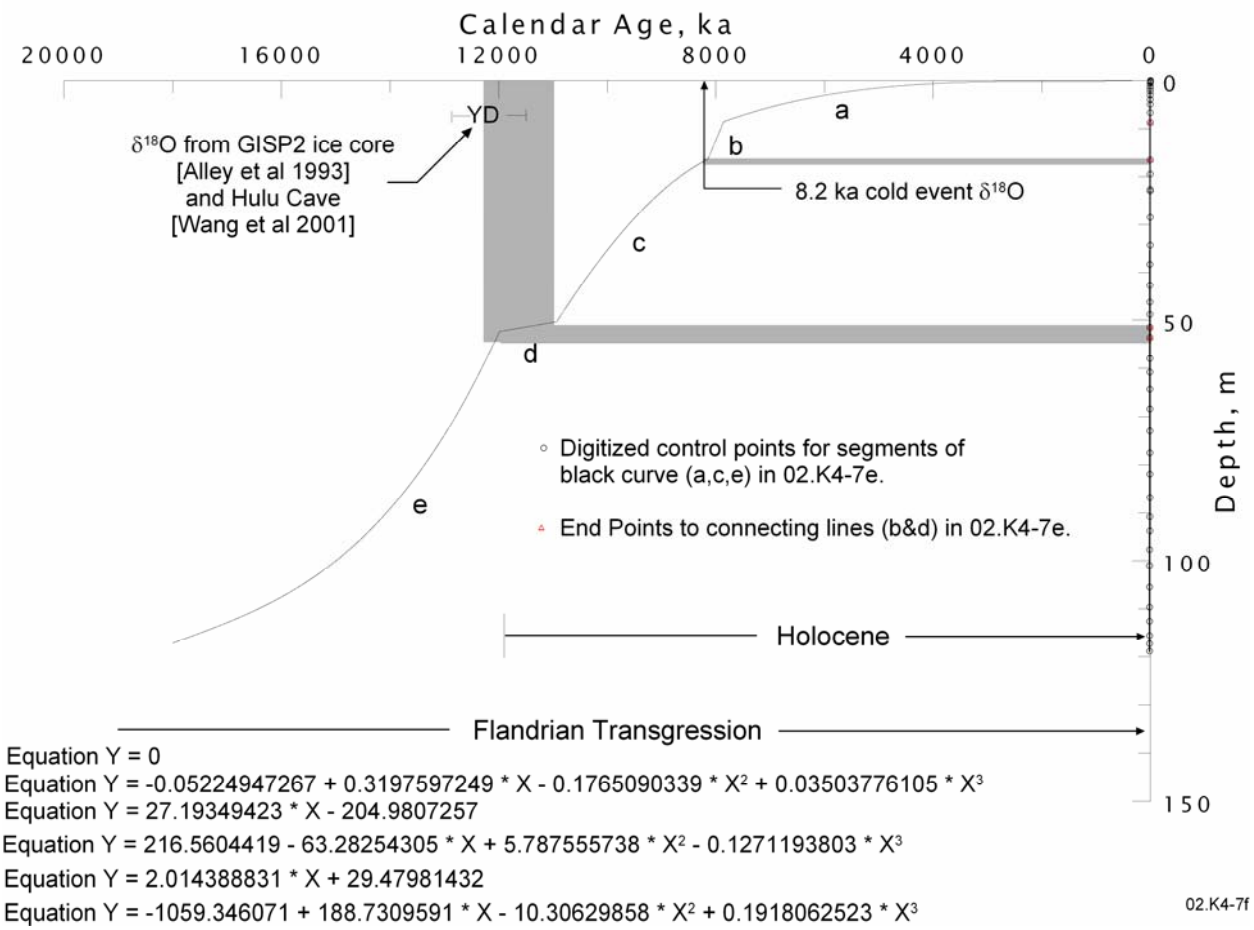

Figure 4: Sea level curve with polynomial fits used for coastal evolution modeling

about 12 thousand years before present (ka), one about 8.2 ka, and the modern stillstand. Paleo wave-cut terraces are notched into the shelf and are now found by seismic (subbottom) profiling beneath the cover of surface sediment. The two paleo-terraces provide relatively precise time and depth markers for model calibration. Also, the low sea level during the Younger Dryas event exposed large areas of offshore banks and caused significant modification in the shoaling patterns of waves and currents of the bight. The polynomial equations in Figure 4 are used to define the relationship between sealevel and time and the rate of sea level change for these various paleo events.

1.2 Littoral Cell

The model is functionally based on a geographic unit known as a littoral cell. A littoral cell is a coastal compartment that contains a complete cycle of sedimentation including sources, transport paths, and sinks. The universality of the littoral cell makes the model easily adaptable to other parts of the world by adjusting the boundary conditions of the model to cells characteristic of different coastal types (e.g., Inman, 2003).

We apply our coastal evolution model to the Oceanside littoral cell (figure 5) first because it has been studied extensively and is tectonically the most stable of the five cells of the Southern California Bight. The computational area for the Oceanside littoral cell extends for 130 km in an on-offshore direction from the mountains of the coastal watersheds, rising to elevations of about 2000 m, seaward to the San Diego Trough in water depth of about 1200 m. The cell extends 84 km along the coast from Dana Point south to Point La Jolla. The sediment sources for the cell are the soil eroded from the watersheds that is carried to the coast by streams and the erosion of sea cliffs by wave energy. The sand moves along the coast as a river of sand powered by wave action. Scripps and La Jolla submarine canyons cut across the shelf and intercept the river of sand. The sand is transported episodically down the submarine canyons by turbidity currents and deposited on the floor of San Diego Trough. Longshore transport and loss down the Scripps-La Jolla submarine canyons is about 200,000 m^3/yr. Of this quantity, about 10%-20% is from sea cliff erosion and the rest is from streams and terraces (Inman and Masters, 1991; CDBW and SCC, 2002).

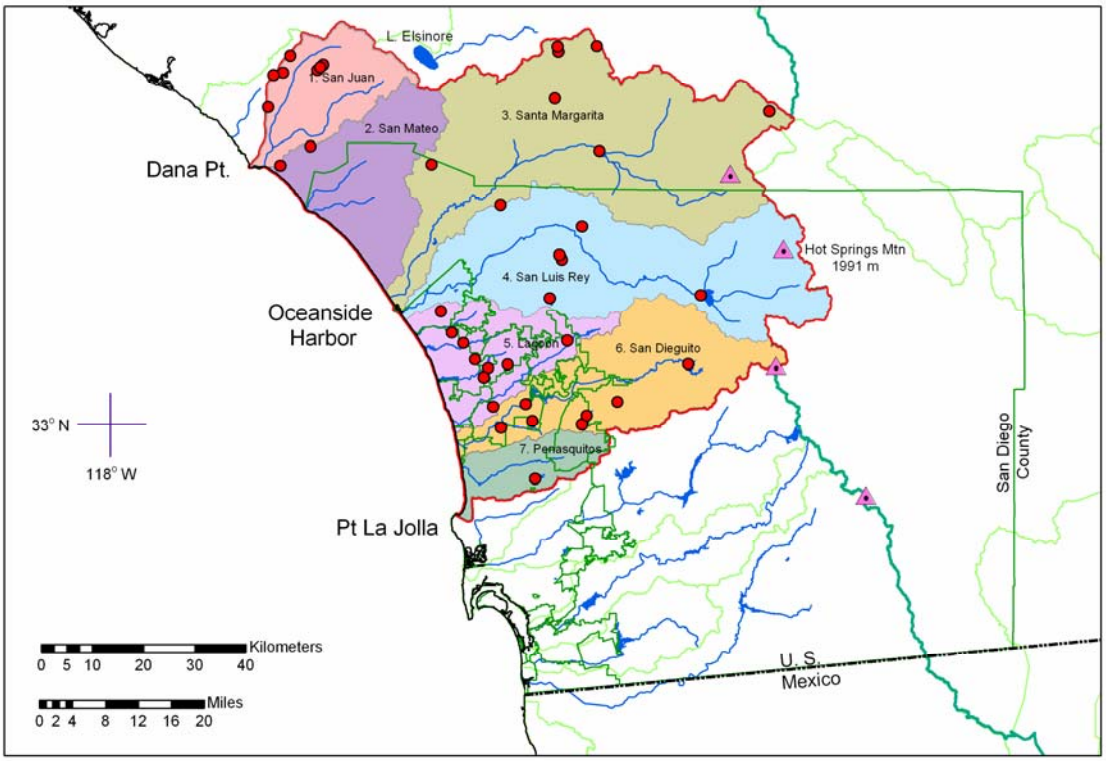

Figure 5: Oceanside Littoral Cell with drainage basins indicated by colored shading and dams by red circles

2. Littoral Cell Model (LCM) Algorithms and Code Documentation

The variation of the sediment cover with time is modeled by time-stepped solutions to the sediment continuity equation (otherwise known as the *sediment budget*) applied to the boundary conditions of the coupled control cell mesh diagramed schematically in Figure 3. The sediment continuity equation is written:

$$\frac{\partial Q}{\partial t} = \frac{\partial}{\partial y}\left(\varepsilon \frac{\partial Q}{\partial y}\right) - V_l \frac{\partial Q}{\partial y} + J(t) - R(t) \qquad (5)$$

Where q is the sediment volume per unit length of shoreline (m^3/m), ε is the mass diffusivity, V_l is the longshore current, *J(t)* is the flux of new sediment into the littoral cell from watrersheds and *R(t)* is the flux of sediment lost to sinks, typically submarine canyons, lagoons, spits and harbors. The first term in (5) is the

surf diffusion while the second is divergence of drift For any given control cell in Figure 3, (5) may be discretized in terms of the rate of change of beach volume, V, in time t, given by:

$$\frac{dV}{dt} = J(t) + Q_{L1} + Q_{RE} - Q_{L2} \qquad (6)$$

Sediment is supplied to the control cell by the sediment yield from the rivers, $J(t)$, by the influx littoral drift from up-coast sources, Q_{L1} and by new sediment that recharges the system Q_{RE} as a consequence of bluff erosion within the control cell. Sediment is lost from the control cell due to the action of wave erosion and expelled from the control cell by exiting littoral drift, Q_{L2}. Here fluxes into the control cell ($J(t)$ and Q_{L1}) are positive and fluxes out of the control cell (Q_{RE} and Q_{L2}) are negative. The beach sand volume change, dV/dt, is related to the change in shoreline position, dX/dt, according to:

$$\frac{dV}{dt} = \frac{dX}{dt} \cdot Z \cdot l \qquad (7)$$

where

$$Z = Z_1 + h_c \qquad (8)$$

Here, Z is the height of the shoreline flux surface equal to the sum of the closure depth below mean sea level, h_c, and the height of the berm crest, Z_1, above mean sea level; and l is the length of the shoreline flux surface. The shoreline flux surface is the landward boundary of the Oceanside Cell (Figure 1). Hence, beaches and the local shoreline position remain stable if a mass balance is maintained such that the flux terms on the right-hand side of equation (5) sum to zero.

In the following sections, we proceed with prescribing the computational methods and codes for each of the terms appearing on the right hand sides of (5) and (6).

2.1 Sediment Flux Input from Watersheds:

Long-term sediment yield data induced by rainfall variation was derived by applying sediment rating curves to the annual mean stream flow of the seven major rivers of the Oceanside Littoral Cell (Figure 5). The rating curves were derived in a two step procedure [e.g., Brownlie and Taylor, 1981a&b]. This procedure utilized a limited amount of daily sediment flux measurements available under two separate USGS monitoring programs, namely: 1) the Hydrologic Benchmark Network; and 2) the National Stream Quality Accounting Network. Rather than seeking rating curves between annual flow volume and annual sediment flux per Brownlie and Taylor (1981a), better correlations were obtained between daily cumulative flow volume, (V_i, m^3/day) and daily sediment yield (J_i, tons/day). These data were fitted to a power function $J_i = aV_i^b$, where a and b are statistically derived constants. The code which reads the USGS streamflow data bases and generates structured time series of V_i is **usgs_riv.for** found in Appendix-A. The input parameters output files which are required by **usgs_riv.for** are:

sncl6881.txt……*USGS daily flow rate file
36 ……..*number of lines of header (nhead)
1968……* first water year in record (ist_yr)
1981……* last water year in record (iend_yr)
sncl6881.wyr……..*output file water year average flow rate cfs
sncl6881.dta……*output file numerical daily flow rate only
sncl6881.mon……..*output file of monthly averages oct-sep wy

The second step of the procedure applies the daily sediment rating curves to the daily stream flow volumes, $\boldsymbol{V}_{\mathrm{i}}$, measured by USGS over the entire period of record. The results were then summed by water year to give the year-by-year annual flow volumes, $\boldsymbol{V}$, and annual sediment fluxes J. The sediment rating curve derived by this procedure based upon the USGS sediment monitoring data reported in Inman and Jenkins, 1998. The sediment yield is generally quite sensitive to river flow rate, increasing as $1.4 < b < 2.2$ (Inman and Jenkins, 1999). These rating curves were built from Brownlie and Taylor (1981b), supplemented by best fit power law curves of the form $J_i = aV_i^{\,b}$ applied to additional USGS measurements. These are found in (Inman and Jenkins, 1999).

Pronounced effects of the alternate series of La Niña (cool-dry) and El Niño (warm-wet) periods can also be found on sediment yield of the watersheds of the Oceanside Littoral Cell. This is a consequence of variability in local rainfall accompanying La Niña (cool-dry) and El Niño (warm-wet) periods (Figure 6). Climatic trends become more apparent when the rainfall and river sediment yield data are expressed in terms of cumulative residuals Q_{n}, taken as the continued cumulative sum of departures of annual values of a time series Q_{i} from their long-term mean values $\overline{Q}$, such that $Q_n = \sum_{o}^{n} (Q_i - \overline{Q})$ where n is the sequential value of a time series of $\boldsymbol{n}$ years. This method was first used by Hurst (1951; 1957) to determine the storage capacity of reservoirs on the Nile River, where the range of the cumulative residual Q_{n} gives the needed deficit or credit storage capacity necessary for runs of excessively dry or wet years. The Hurst method has since been widely used to show trends in natural phenomena such as rainfall [e.g., Flick, 1993], river flow [Reihl and Meitin, 1979], river sediment flux [Inman and Jenkins, 1997], and turbulent flow intensity [Van Atta and Helland, 1977]. We use the Hurst method to determine the periods of ENSO-induced climate change

reflected in sediment yield of rivers [i.e., Inman and Jenkins, 1997]. In making this calculation we use the USGS flow rate histories measured on the Oceanside Cell river stations (USGS gage station #11012000) during water years 1984-89, and then supplement those measurements with hindcasted flow rate history due to Chang (2004). Daily flow rate estimates were generated from the Chang (2004) hindcasts of peak flow and flow volume by assuming a triangular hydrograph. In applying the rating curve to the historic daily flow rates reconstructed from the Chang (2004) hindcasts, it was assumed that 63% of the calculated yield was sand sized if the peak flow rate was greater than 1000 cfs, and 100% wash load if the sediment fluxes calculated from rating curves and flow rate histories are plotted as cumulative residuals vs time (Figures 7 - 9), the Oceanside Cell rivers displayed a clear change from wet to dry climate beginning in 1944. Note that periods of low sediment yield representing dry climate appear as intervals of decreasing residual (negative slope), while high sediment yield (wet periods) are represented by intervals of increasing residual (positive slope). Within the 52-year period (1944-1995), the data in Figures 6-9 showed a uniform dry period lasting for about 25 years from 1944 through 1977. However, there was a relatively weak El Niño embedded in 1944-77 drought period that occurred in 1969, which had a peak SOI of -0.8. A storm associated with the 1969 El Niño caused significant flooding and high sediment yield on the Oceanside Cell rivers.

Beginning in 1978, the southern California climate began transitioning into a warmer wetter period characterized by a succession of powerful El Niños, particularly those in, 1978, 1980, 1983, 1993 and 1995, [Inman & Jenkins, 1997]. The floods brought by each of these El Niño events delivered

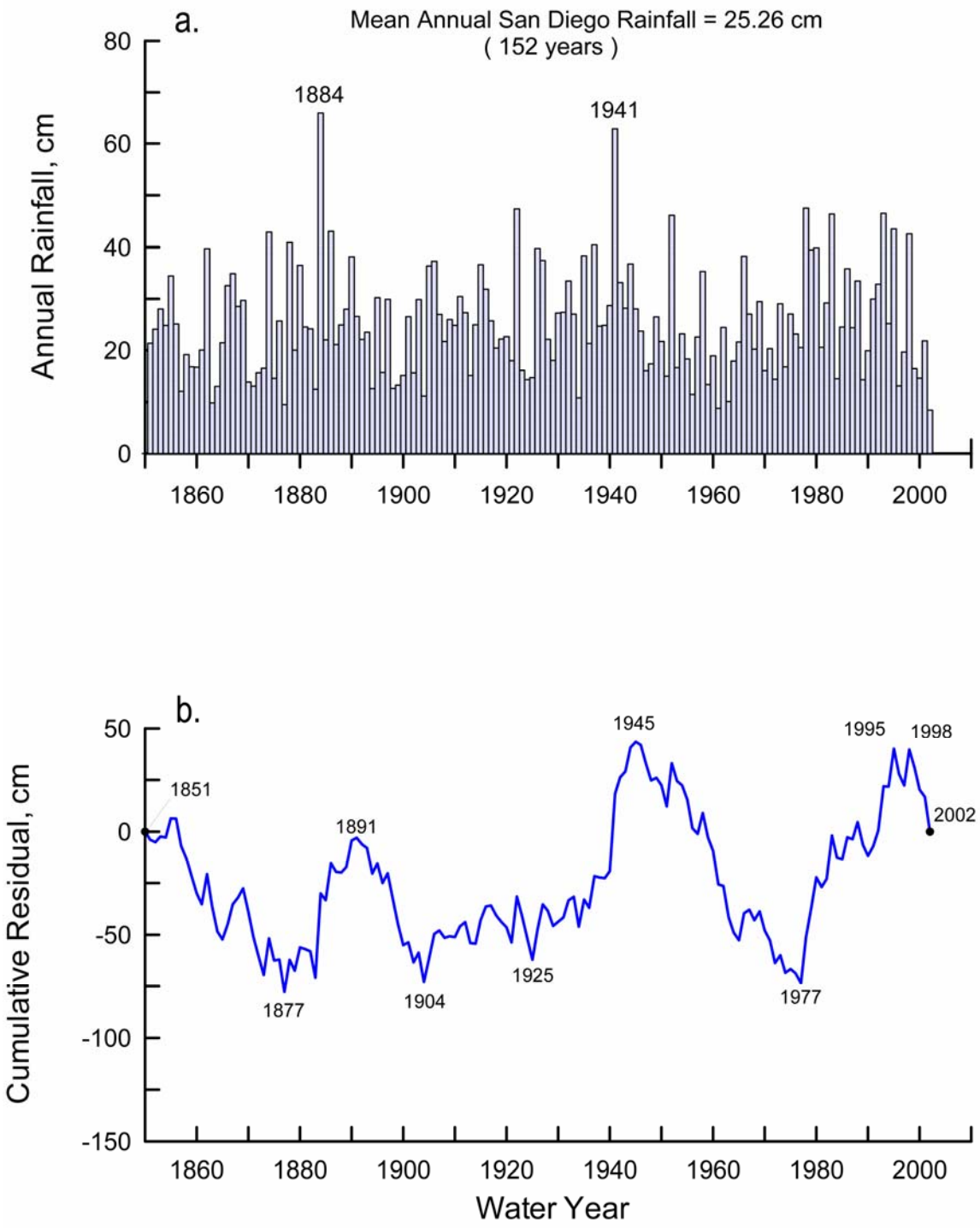

Figure 6. a) Period of record of San Diego rainfall and b) cumulative residual.

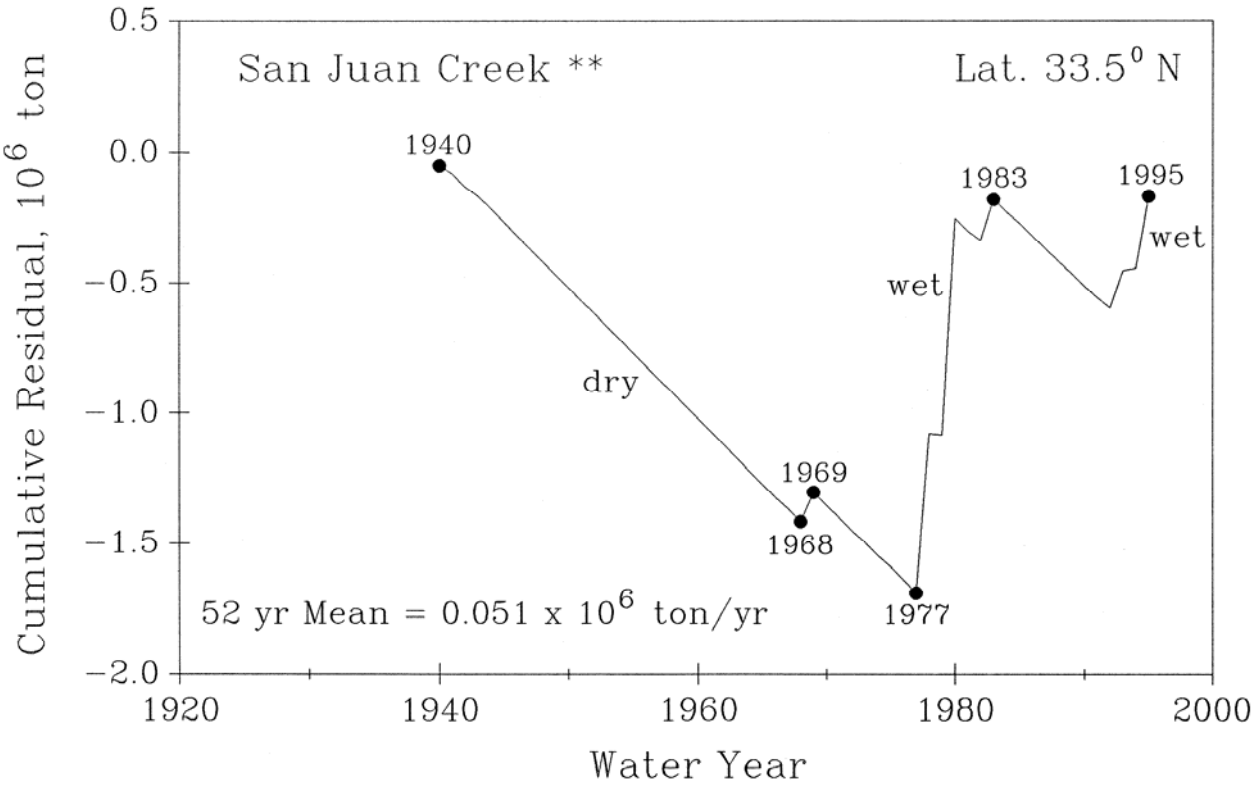

Figure 7. Cumulative residual time series of sediment flux for the San Juan Creek calculated using a 56-year mean (1940-1995).

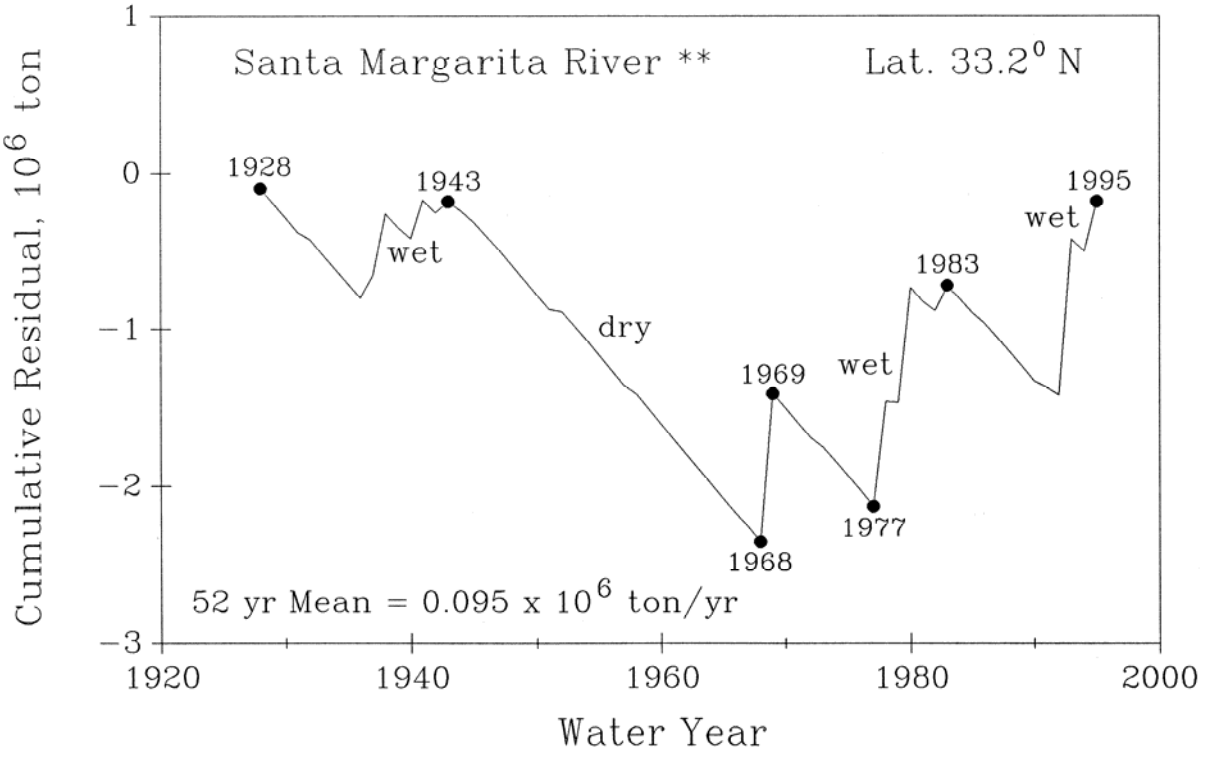

Figure 8. Cumulative residual time series of sediment flux for the Santa Margarita Rriver calculated using a 68-year mean (1928-1995)

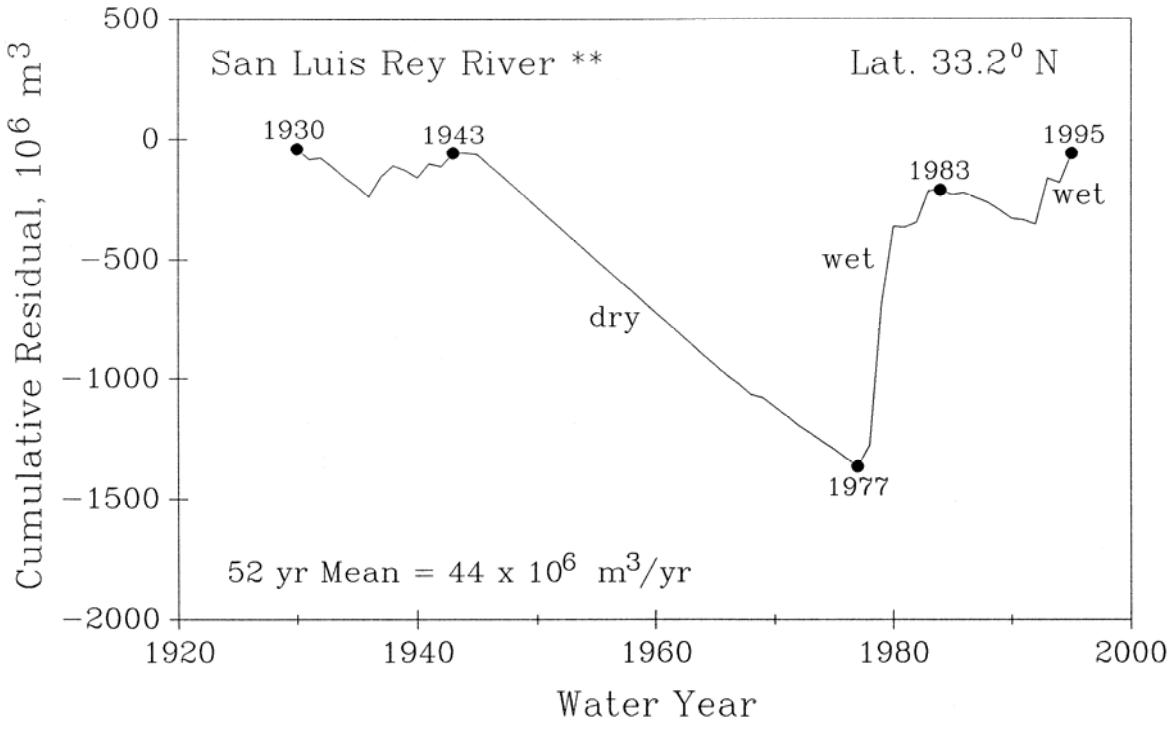

Figure 9. Cumulative residual time series of sediment flux for San Luis Rey River calculated using a 66-year mean (1930-1995)

many times the long term mean for all the major tributaries of the Oceanside Cell rivers, causing the cumulative residuals in Figure 6-9 to abruptly increase. A similar succession of El Niño floods also preceded the cool/dry period of 1944-77, causing major episodes of sediment yield in 1927, 1937, 1938, 1941 and 1943. The cumulative residual of the historic sediment yield of the Oceanside Cell rivers in Figure 6-9 reveals a number of significant features having particular importance to the nourishment and long-term stability of the Oceanside Cell beaches. These features are independent of the computational techniques; regardless of whether the rating curve from USGS measurements and Chang (1995) flow rate hindcasts are used, or whether an independent set of calculations by Simon and Li (1988) are used. While the long-term average is between 210,000 tons/yr. depending upon the data used, this long-term average is the result of a relative few number of events. The peak annual discharge of sediment (100-year storm) is 990,000 tons/yr. In a cool/dry La Niña dominated climate period there is no sediment yield whatsoever.

Because of upstream intervention by man, the sediment yield of the most recent series of floods during the current warm/wet El Niño dominated climate is only a fraction of what it once was during the previous warm/wet period prior to 1943. Consequently, it is critical that sediment yield by the Oceanside Cell rivers not be restricted any further by the proposed restoration project if adequate local sources of beach nourishment for Oceanside Cell are to be maintained Thus, an inter-decadal pattern of sediment yield has persisted for the Oceanside Cell rivers during the last 75 years, characterized by alternating cool/dry La Niña dominated periods with little or no sediment yield, followed by warm/wet El Niño dominated periods when most of the total sediment yield is produced. These same inter-

decadal cool/dry and warm/wet cycles in sediment yield are found for all the other major rivers of the Southern California Bight, see Inman & Jenkins (1997). Inter-decadal climate variability is observed throughout the west coast of the Americas and is now known as the ***Pacific Interdecadal Oscillation (PDO)***, see Mantua et al (1997) and Zhang et al (1997). As a consequence of PDO, the unrestricted sediment yield of a few major flood years re-supplies the beaches of the Oceanside Littoral Cell and provides a significant reserve of sand that helps these beaches to survive the erosion from waves during protracted drought periods when no new sand is received from stream sources. Under natural conditions, beach sediment supplies during these protracted droughts were maintained by bluff and dune failures. However, hardening of these formations with coastal structures eliminates this auxiliary source, making the river sediment yield during warm/wet periods even more critical to maintaining the beaches.

The sediment flux's from Oceanside Littoral Cell watersheds, and their related cumulative residuals, are calculated by the model code **sed_rate.for** found in Appendix-B. The input parameters output files which are required by **sed_rate.for** are:

sd_rfr85.txt ……*USGS daily flow rate input file
36……*number of lines of header (nhead)
2.03422……...*expon b from rating curve fit $J_i = aV_i^{\,b}$
0.02526……...*coeff a from rating curve fit $J_i = aV_i^{\,b}$
sd_sed85.dat……....*output file water year: day, daily flow rate (cfs), sed (tons), cum_sed

2.2 Longshore Transport and Erosion Potential

In this section we calculate the flux terms $Q_{L1,}$ Q_{L2}, i.e., the flux of sand into or out of a ***near-field computational sub-cell*** due to longshore transport using a series of coupled control cells as shown Figure 3. We use a portion of the Oceanside Cell for this computational sub cell and refer to it as the Torrey Pines Sub-Cell (Figure 10).

The potential longshore transport rate can be computed using the wave records measured during the Coastal Data Information Program, (CDIP). This program routinely monitored waves at several locations in the lower Southern California Bight since 1980 by the Coastal Data Information Program. The nearest CDIP directional wave monitoring sites for the Oceanside Cell and Torrey Pines Sub-Cell are:

a) Oceanside Array

- Station ID: 00401
- Location:
  - 33 11.4□North, 117 23.4□West
    - 500 feet SW of pier
- Water Depth (m): 10
- Instrument Description:
  - Underwater Directional Array
- Measured Parameters:
  - Wave Energy
    - Wave Period
    - Wave Direction

b) San Clemente

- Station ID: 05201
- Location:
  - 33 25.2□North, 117 37.8□West
    - 1000 ft NW of San Clemente Pier
- Water Depth (m): 10
- Instrument Description:
  - Underwater Directional Array

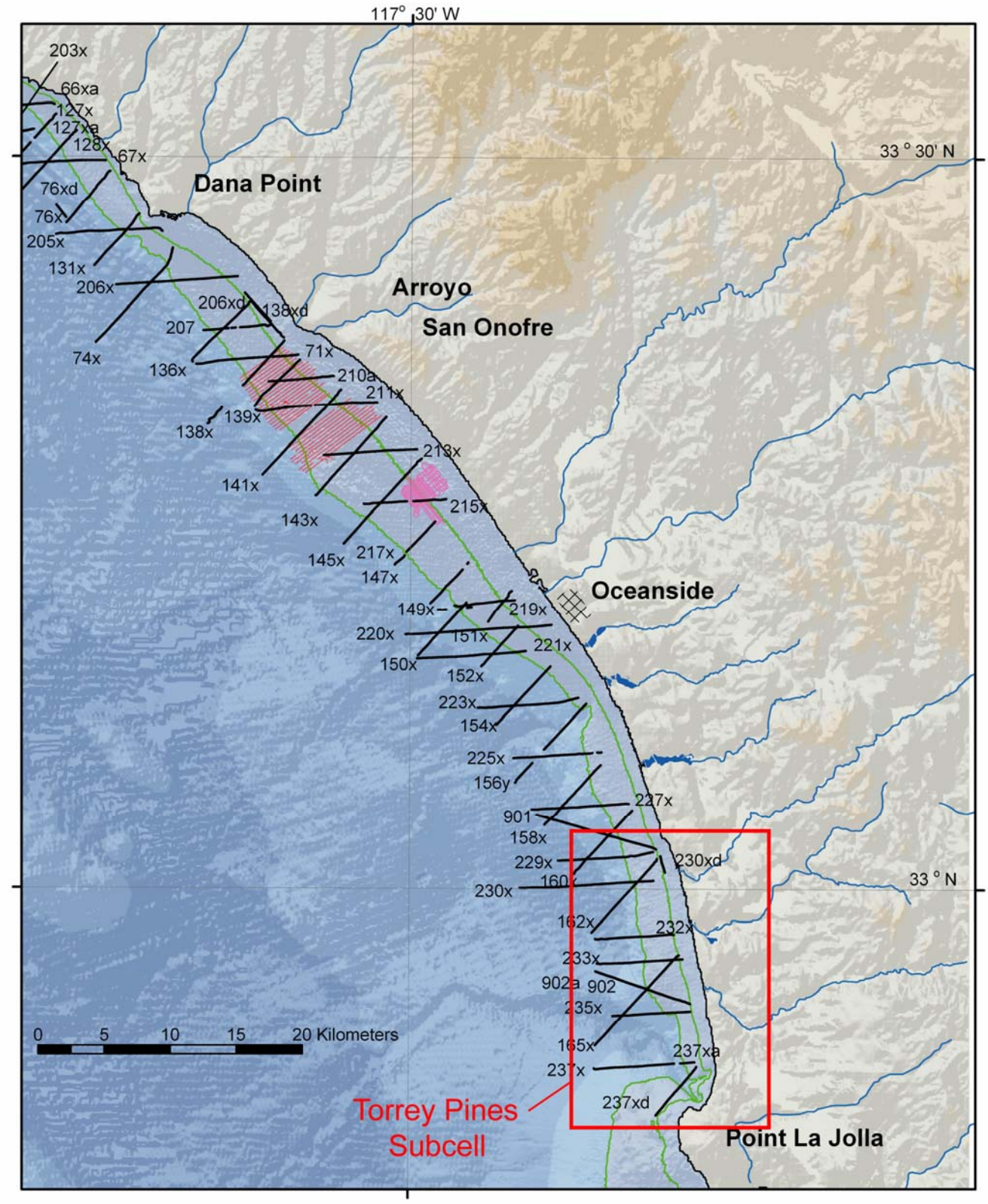

Figure 10: Torrey Pines Sub-Cell. USGS survey lines shown in black.

Measured Parameters:

- Wave Energy
- Wave Period
- Wave Direction

c) Huntington Beach Array

- Station ID: 07201
- Location:
  - 33 37.9 North, 117 58.7 West
    - Approximately 1 mile west of lifeguard headquarters at Huntington Beach, CA
- Water Depth (m): 10
- Instrument Description:
  - Underwater Directional Array
- Measured Parameters:
  - Wave Energy
  - Wave Period
  - Wave Direction

In addition to these CDIP sites waves have been monitored at Torrey Pines Beach from 1972 until 1984 by the SAS Stations deployed by Scripps Institution of Oceanography, (SIO), Pawka (1982). These data sets possessed gaps at various times due to system failure and a variety of start ups and shut downs due to program funding and maintenance. The undivided data sets were pieced together into a continuous record from 1980-2000 and entered into a structured preliminary data file. The data in the preliminary file represent partially shoaled wave data specific to the local bathymetry around each monitoring site. To correct these data to the nearshore of Torrey Pines, they are entered into a refraction/diffraction numerical code, back-refracted out into deep water to correct for local refraction and island sheltering, and subsequently forward refracted into the immediate neighborhood of Torrey Pines. Hence, wave data off each monitoring site was used to hindcast the waves at Torrey Pines. Data from the reports beginning

January 1980 through March 2002 [CDIP, 2004] were compiled and entered into a structured preliminary data file.

The data in the preliminary file represent partially shoaled wave data specific to the local bathymetry around Oceanside. To correct these data to the near-field computational cell, they are entered into a refraction/diffraction numerical code, back-refracted out into deep water, and subsequently brought onshore into the immediate neighborhood of Oceanside as shown in Figure 10a. Hence, wave data off Oceanside was used to hindcast the waves at Oceanside. CDIP wave data are shoaled into the beaches near the project site using a numerical refraction-diffraction computer codes called **OCEANRDS**. The primitive equation for this code are lengthy, so a listing of the FORTRAN codes of OCEANRDS appear in Appendix C and D. These codes calculate the simultaneous refraction and diffraction patterns propagating over a Cartesian depth grid. "OCEANRDS" uses the parabolic equation method (PEM), Radder (1979), applied to the mild-slope equation, Berkhoff (1972). To account for very wide-angle refraction and diffraction relative to the principle wave direction, "OCEANRDS" also incorporates the high order PEM Pade approximate corrections modified from those developed by Kirby (1986a-c). Unlike the recently developed REF/DIF model due to Dalrymple et al (1984), the Pade approximates in "OCEANRDS" are written in tesseral harmonics, per Jenkins and Inman (1985); in some instances improving resolution of diffraction patterns associated with steep, highly variable bathymetry along the shelf break. These refinements allow calculation of the evolution and propagation of directional modes from a single incident wave direction; which is a distinct advantage over the more conventional directionally integrated ray methods that are prone to caustics (crossing rays) and other singularities in the solution domain where bathymetry varies rapidly over several wavelengths.

There is a family of OCEANRDS codes, with each specific to particular grid domains. For the back refraction problems and other far field applications the **oceanrds_socal.for** version (Appendix-C) is used on a 2,405 x 4,644 raster formatted grid that encompasses the entire Southern California Bight. The input parameters output files which are required by **oceanrds_socal.for** are

graham_m.grd *……...* (name.grd) bathymetry input file
-1.0…….*(gis) if data is parsed GIS data gis= -1.0, if NOS data gis=1.0
1……..* wave exposure 1=west, 2=north, 3=east, 4=south (icoast)
0.0 …….* sea level adjustment MSL meters (sealev) (+ = deeper water)
77.5 ……..* outer grid dimensions in meters perpendicular to coast (sx)
92.6……...* outer grid dimensions in meters parallel to coast (sy)
4644 .....* number of grid cells in from deep water perpendicular to coast raster (nx)
2405…….* number of grid cells along coast from top edge (ny)
17.0…….* wave period in seconds (persw)
270.0……...* wave direction degress clockwise from true north (asw)
10.0……* wave height meters (hsw)

An example of a reconstruction of the wave field throughout the Bight is shown in Figure 11 using the back refraction calculation of the CDIP data from the San Clemente array. Wave heights are contoured in meters according to the color bar scale and represent 6 hour averages, not an instantaneous snapshot of the sea surface elevation. Note how the sheltering effects of Catalina and San Clemente

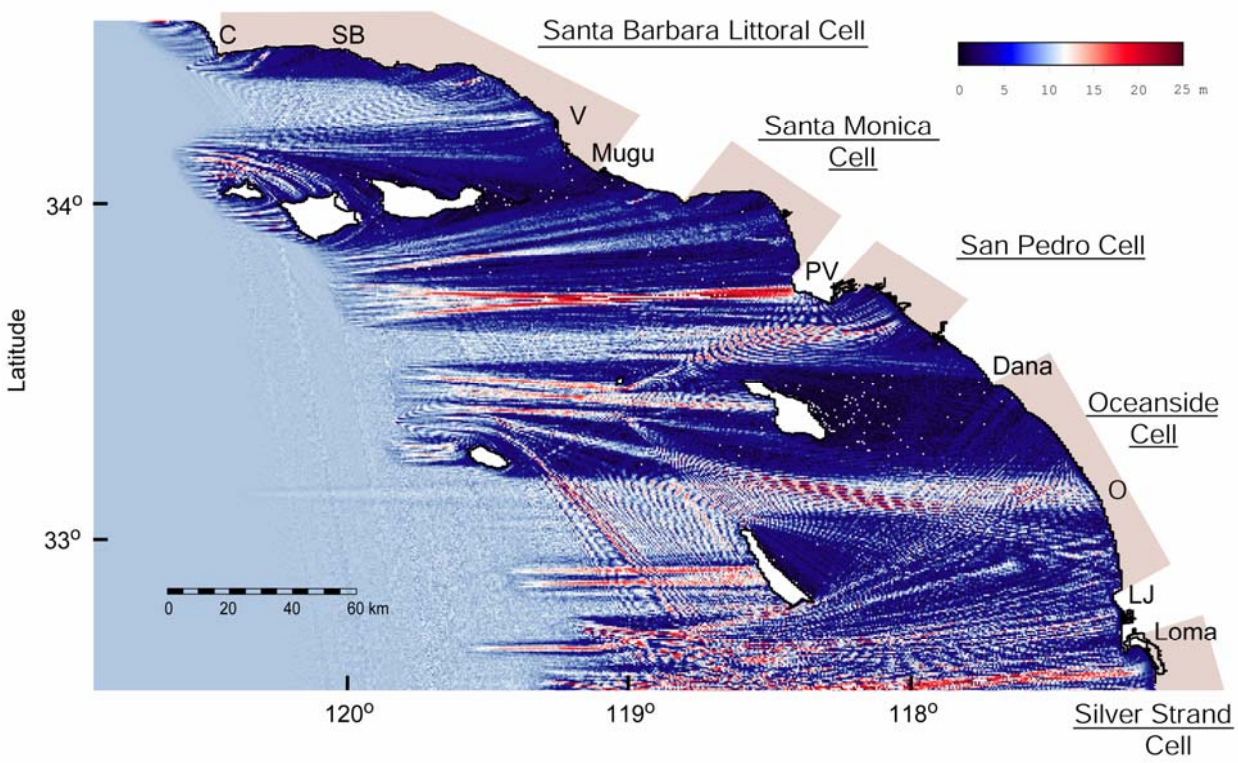

Figure 11: Back-refraction using *oceanrds_socal.for* with waves measured by San Clemente CDIP station during the storm of 17 January 1988 with 10m high waves at 17 second period approaching the Southern California Bight from 270^0

Islands have induced longshore variations in wave height throughout the Southern California Bight. These variations (referred to as shadows and bright spots) induce longshore transport away from areas of high waves (bright spots, red) and toward areas of low waves (shadows, dark blue). Figure 12 shows the deep water significant wave heights, periods and directions resulting from the series of back-refraction calculations for the complete CDIP and SIO data set at Δt = 6 hour intervals over the 1980-2000 period of record. The data in Figure 12 are the values used as the deep water boundary conditions of the forward refraction computations into the Torrey Pines Sub Cell (Figure 10). The deep water wave angles are plotted with respect to the direction (relative to true north) from which the waves

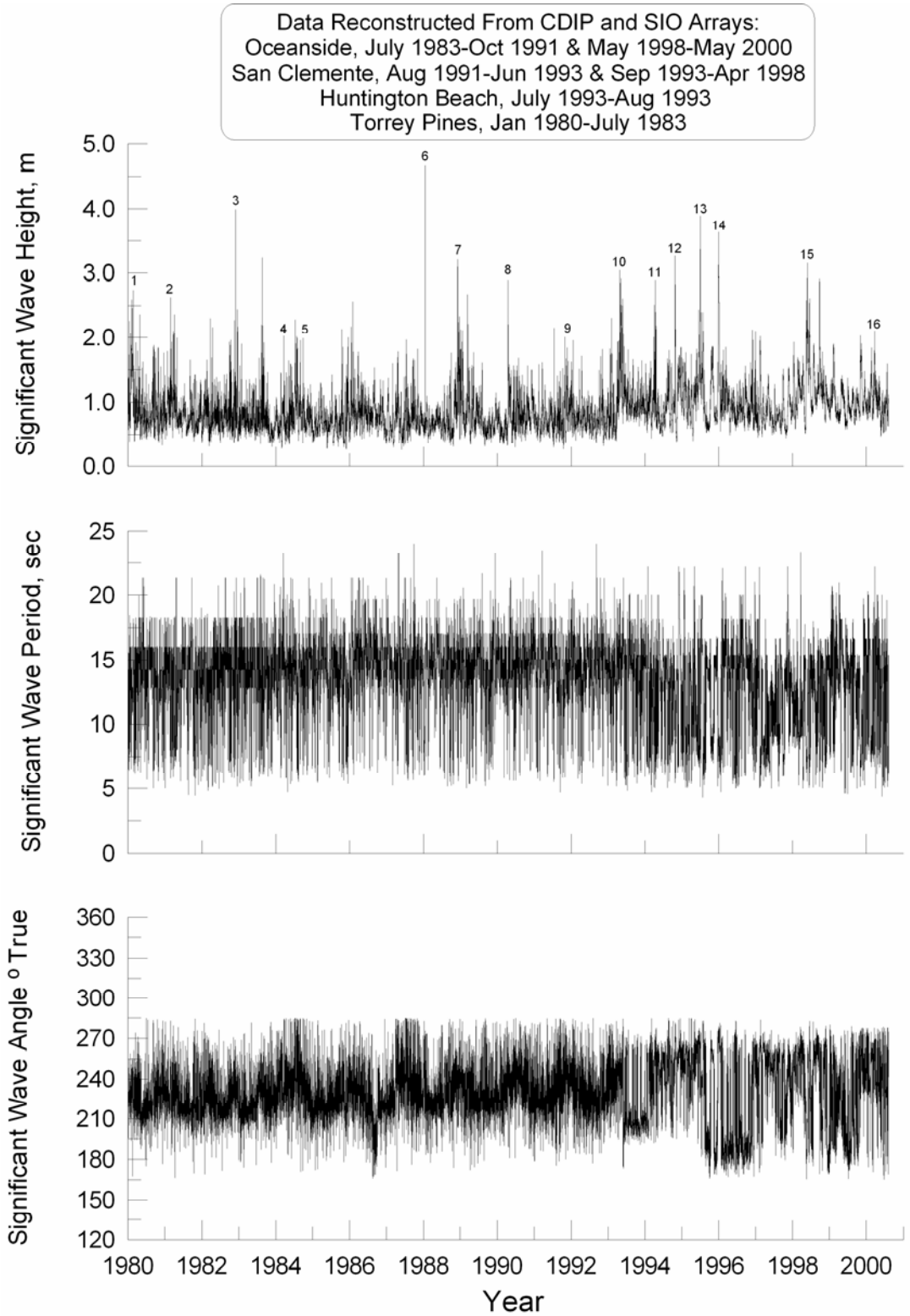

Figure 12: Deep water wave data for CEM forcing in Torrey Pines Sub-Cell derived from backrefraction of CDIP monitoring data

are propagating at the deep water boundary of Figure 10. Inspection of Figure 12 reveals that a number of large swells lined up with the wave windows open to Torrey Pines during the El Niño's of 1980-83, 1986-88, 1992-95, and 1997-98. The largest of these swell events was the 18 January 1988 storm, producing 4.5 m deep water swells off Torrey Pines (see event #6 in Figure 12).

For high resolution local refraction/diffraction calculations within the Torrey Pines Sub-Cell, we use the **oceanrds_tp.for** codes on a 441 x 236 raster formatted grid found in Appendix D. The input parameters output files which are required by **oceanrds_tp.for** are:

subbot50.grd…….*bathymetry input file
1.0……*(gis) if water values are negative gis= -1.0, if positive gis=1.0
1…… * wave exposure 1=west, 2=north, 3=east, 4=south (icoast)
0.0……* sea level adjustment MSL meters (sealev) (+ = deeper water)
50.0……..* inner grid dimensions in meters perpendicular to coast (sx)
50.0……..* inner grid dimensions in meters parallel to coast (sy)
236……* number of grid cells in from deep water perpendicular to coast raster (nx)
441……* number of grid cells along coast from top edge (ny)
15.0……...* wave period in seconds (persw)
285.0…….* wave direction degress clockwise from true north (asw)
2.0…….* wave height meters (hsw)

Figure 13 gives an example of the forward refraction calculation over the farfield grid of the Torrey Pines region for the largest swells occurring during the peak flow month of February 1998. These swells occurred 28 February 1998

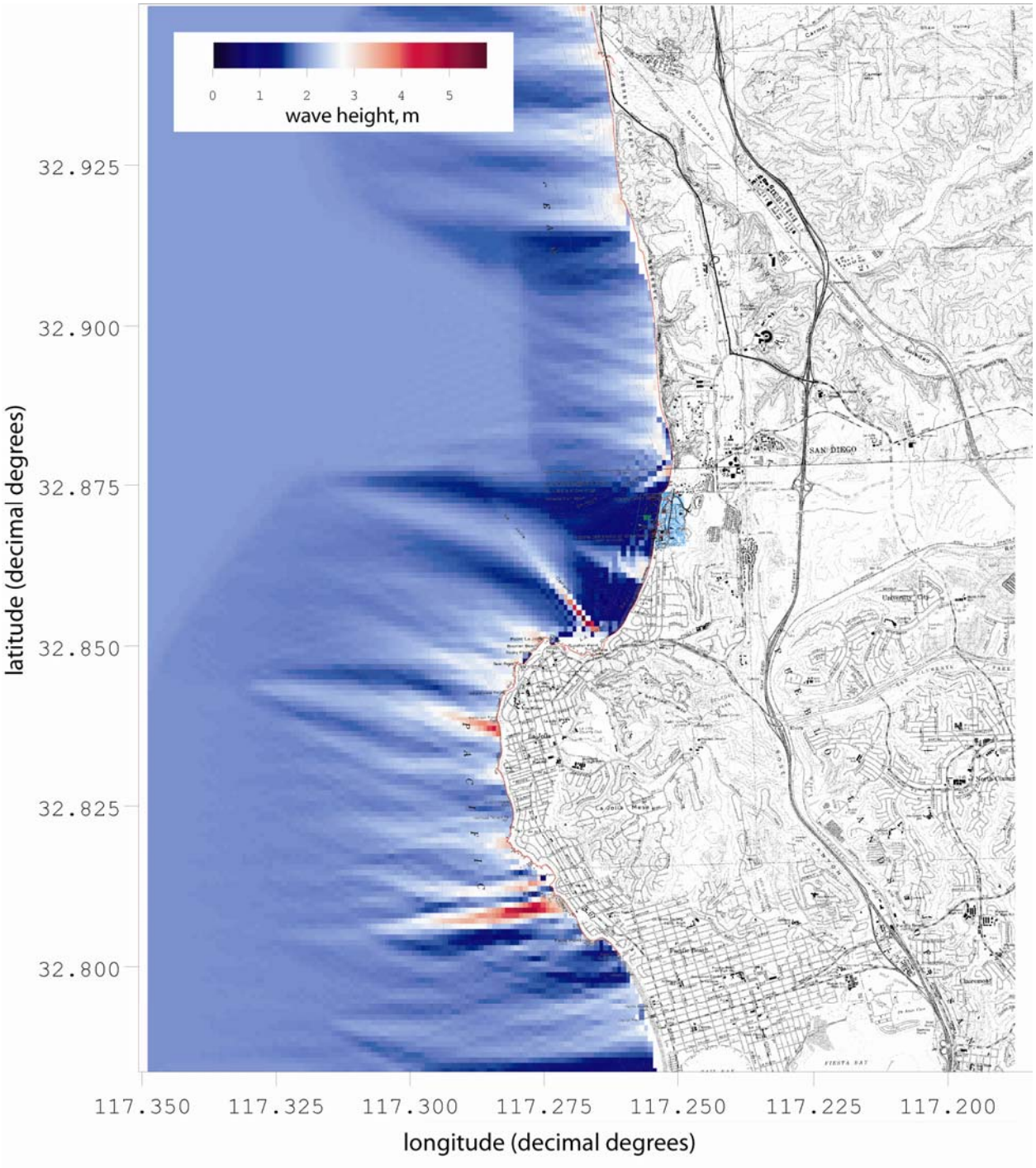

Figure 13: High resolution refraction/diffraction computation using *oceanrds_tp.for* on the Torrey Pines Sub-Cell during the 24 February 1998 storm with 2m deep water wave height from 285^0 with 15 sec period.

concurrent with the peak flow event in the Santa Margarita and San Luis Rey Rivers which occurred later in the month on 24 February 1998. We note very pronounced patterns of shadows and bright spots in the neighborhood of Point La Jolla and the Scripps and La Jolla Submarine Canyons. These alongshore variations in shoaling wave height result in strong alongshore variations in the strength of longshore currents and littoral drift termed divergence of drift and represented by the second term on the right hand side of (5).

To perform both the backward and forward shoaling computations, the refraction/diffraction algorithms require relatively fine-scale resolution of the bottom bathymetry, needing at least two grid points per wavelength of the highest frequency wave to be shoaled. The **oceanrds_socal.for** and **oceanrds_tp.for** codes run on a 3 x 3 and 2 x 2 arc-sec rectangular grids of bathymetry/elevation values. These codes require this grid data to be formatted as ascii real numbers. (The horizontal distance between cells is variable based on the latitude at the center of the grid and is entered as an input file parameter.) The data is obtained at the National Geophysical Data Center (NGDC) web site:
(http://www.ngdc.noaa.gov/mgg/gdas/gd_designagrid.html)
Referring to the web site macro in Figure 14, the procedure for down loading and structuring the grids is as follows:

1) enter 8-character grid ID (name of grid file during download/retrieval)
2) select “US Coastal Relief Model Grids” as Grid database
3) choose lat.lon bounds (FORTRAN code must be modified to match horizontal and vertical size of grid) ie. 1 deg x 1 deg results in a 1201x1201 grid cell grid
4) select “3-sec” cell size

***Figure* 14: Template for downloading bathymetry grids from NGDC for use in the *oceanrds_socal.for* and *oceanrds_tp.for* refraction/diffraction codes**

5) select “4-byte floating point, 0.1 meter vertical resolution” cell parameter
6) select “ascii raster” format; “no header”
7) select “all cells” coverage
8) hit “Design-a-Grid” button
9) download grid data file as zip-compressed file
10) retrieve file “save to disk”

Two detailed bathymetry grids were developed for the model: a 2,405 x 4,644 raster formatted grid called **graham_m.grd** to perform the back-refraction calculations from the CDIP arrays out to deep water using **oceanrds_socal.for** ; the other, a 441 x 236 raster formatted grid called **subbot50.grd** to forward refract those results with **oceanrds_tp.for** into the Torrey Pines computational cell in Figure 10. The forward refraction calculation with **oceanrds_tp.for** calculates the wave height and x and y components of the wave number at each point in the Torrey Pines computational cell. The x and y components of wave number are orthogonalized to compute the significant wave angle relative to the shoreline normal of each control cell within the Torrey Pines Sub-Cell. The calculation is carried shoreward until the wave height meets or exceeds 5/4 the local depth. This condition defines the point of wave breaking. The wave height, H_b wave angle α_b and grid cell location (x_b, y_b) at which this wave breaking condition is met are written into a **.bra** breaker file for use in subsequent potential longshore transport calculations.

The **.bra files** generated by refraction/diffraction calculations are used to compute the potential longshore transport rates at 6 hour intervals. The formulation for the longshore transport rate is taken from the work of Komar and Inman (1970) according to:

$$Q_{L2} = K\left(C_n S_{yx}\right)_b \qquad (9)$$

where Q_{L2} is the local potential longshore transport rate; C_n is the phase velocity of the waves; $S_{yx} = E\sin\alpha_b \cos\alpha_b$ is the radiation stress component; α_b is the breaker angle relative to the shoreline normal; $E = 1/8\rho g H_b^2$ is the wave energy density; ρ is the density of water; g is the acceleration of gravity; H_b

is the breaking wave height; and, K is the transport efficiency equal to:

$$K = 2.2\sqrt{c_{rb}} \tag{10}$$

$$c_{rb} = \frac{2g\tan^2\beta_0}{H_b\sigma^2} \tag{11}$$

Here c_{rb} is the reflection coefficient which is calculated from a gross estimate of the nearshore bottom slope, β_0 as determined from the bathymetry file using the break point coordinates and the position of the 0 MSL contour; and, σ is the radian frequency = $2\pi/T$, where T is the wave period. These equations relate longshore transport rate to the longshore flux of energy at the break point which is proportional to the square of the near breaking wave height and breaker angle. By this formulation, the computer code calculates a local longshore transport rate for each of 441 break point locations along the shoreline of the Torrey Pines Sub-Cell. A similar set of computations can be done at coarser resolution for the 2,405 solution points along the shoreline of the far field grid that **oceanrds_socal.for** runs on.

The longshore transport rates and divergence of drift that give the time variation of the first and second terms in (5) are computed by the **kavli_flux_socal.for** codes in Appendix-E. The **kavli_flux_socal.for** codes read the o-files of **oceanrds_socal.for** and **oceanrds_tp.for** and computes principal terms of the sediment budget equation (5)-(8), including the wave power EC_n, longshore current V_l, net littoral drift Q, divergence of drift dq/dy and beach

recession dX/dt for each control cell in the gridded computational domain. The input parameters output files which are required by **kavli_flux_socal.for** are:

295_13_3_3_5_-5.wh1……*wave height input file from refraction model
295_13_3_3_5_-5.an1……* wave angle input file from refraction model
graham_m.grd……*bathymetry input file
flux-j_295_13-5.dat……*ofile1
rnmn_d_295_13-5.dat……*ofile2
13.3……..*per1 wave period
15……*iback number of grid cells seaward of the coastline to sample refraction data
475……*isl_gap number of grid cells to jump over estuaries (less than island gap)
34.54519919……..*st_lat upper left corner latitude
2405……*n_rows number of 3 sec grid units, number of rows in graham grid
411……*ist_x column number starting point
1……ist_y row number starting point
77.5 ……..sx m grid cell dimension
92.6……...sy m grid cell dimension
295.0……deep_dir deep water wave direction
0.72……aks transport efficiency
1000.0……rho mks units density of water
2650.0……rhos mks units density of quartz
0.566……vcon net drift into cell from farfield sources (10^3 m^3)
0.3……dirmut directional convergence (degrees)

35…….ijump initial leap interval

100.0……divmax2 initial sweep limit (10^3 m^3)

1.0 ……str_1 computational starting row

14.8 …….sb_st Santa Barbara sub cell start row

1.591 ……str_2 Santa Barbara sub cell stretch factor

162.0 ……sb_nd Santa Barbara sub cell end row

1.0 …….str_3 Santa Monica re-set factor

190.0 ……sm_st Santa Monica cell start row

1.0 ……str_4 Santa Monica cell stretch factor

252.0 ……sm_nd Santa Monica cell end row

1.0 …….str_5 San Pedro re-set factor

269.0 ……...sp_st San Pedro cell start row

0.442 …….str_6 San Pedro cell stretch factor

308 ……sp_nd San Pedro cell end row

1.0 …….str_7 Oceanside re-set factor

335.0 …….. o_st Oceanside cell start row

1.308 …….str_8 Oceanside cell stretch factor

418.0 …… o_nd Oceanside cell end row

0.59066…….. str_9 Point LaJolla/ Pt Loma re-set factor

438.0 …… ss_st Silver Strand cell start row

1.0…… str_10 Silver Strand cell stretch factor

461.0 ……. ss_nd Silver Strandcell end row

0.75 ……. ak2 run up factor Hunt's formula

0.8 …… ak3 gamma breaker factor

0.3 ……akshor Peclet number

The factors listed between str_1 and ss_nd provide geometric transformations of local row numbers into shoreline distances based on the geometry and orientation of the local shoreline.

To demonstrate the computational capabilities of the **kavli_flux_socal.for** codes, we perform an erosion hot-spot analysis of the Southern California Bight based on the linear superposition of the refraction/diffraction patterns of the 5 largest storms in the winter of 1998 (Figure 15). This simulation neglects river sediment flux and considers only the erosion potential of the the first 2 terms on the right hand side of (5), namely the effects of divergence of drift and surf diffusion arising from along shore variation in the height. The computation is based on the coarse scale resolution of the outer grid graham_m.grd. Figure 16a shows how the cumulative wave power of the summed over the 5 biggest storms varies from place to place along the shoreline between Pt Conception and the Mexican border. These along shore gradients in wave height produce diffusive and advective fluxes of sand, where the advective fluxes are shown in Figure 16b. Applying these fluxes to the coupled set of shoreline bounded control cells in the graham_m.grd grid, the **kavli_flux_socal.for** solves (7) for the shoreline recession dX/dt in Figure 16c. Here the retreat rate represents an annual mean due to the cumulative flux of the 5 largest storms in 1998, with negative values representing erosion and positive values representing accretion. Inspection of Figure 16c reveals that the Southern California Bight had a predominately erosional potential during

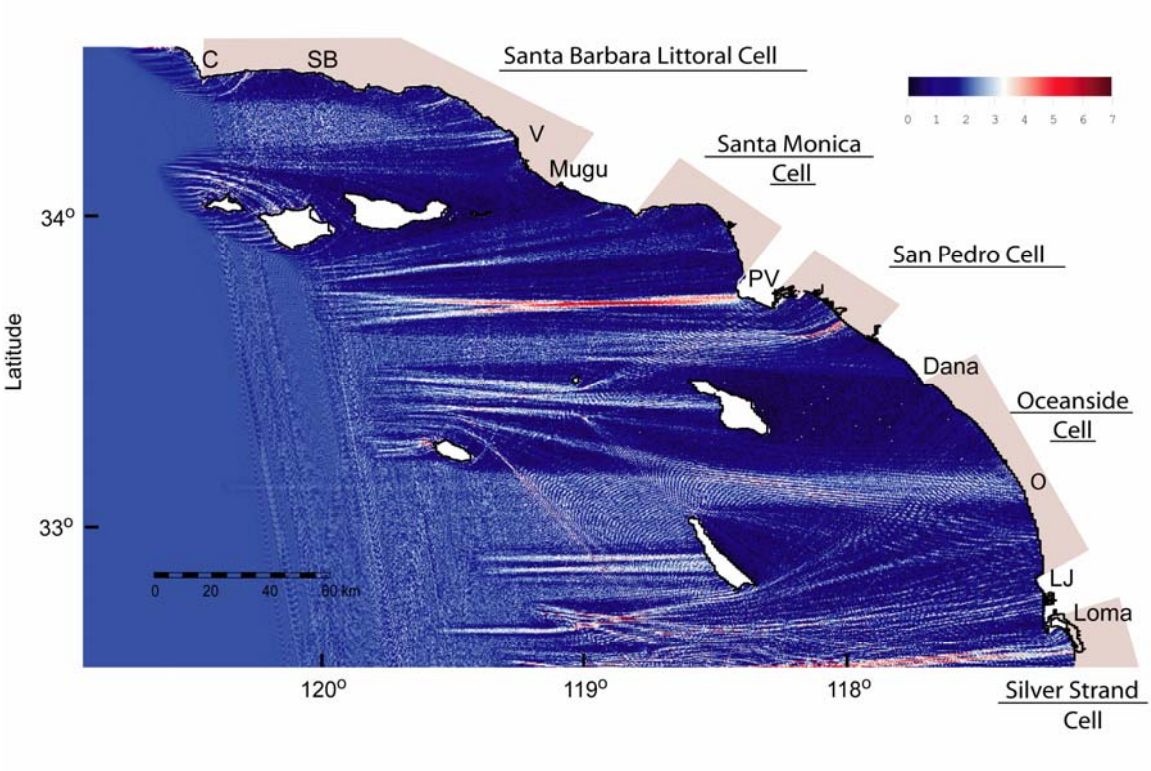

Figure 15: Refraction/Diffraction simulation for erosion hot-spot analysis based on the 5 largest storms of the 1998 El Nino winter

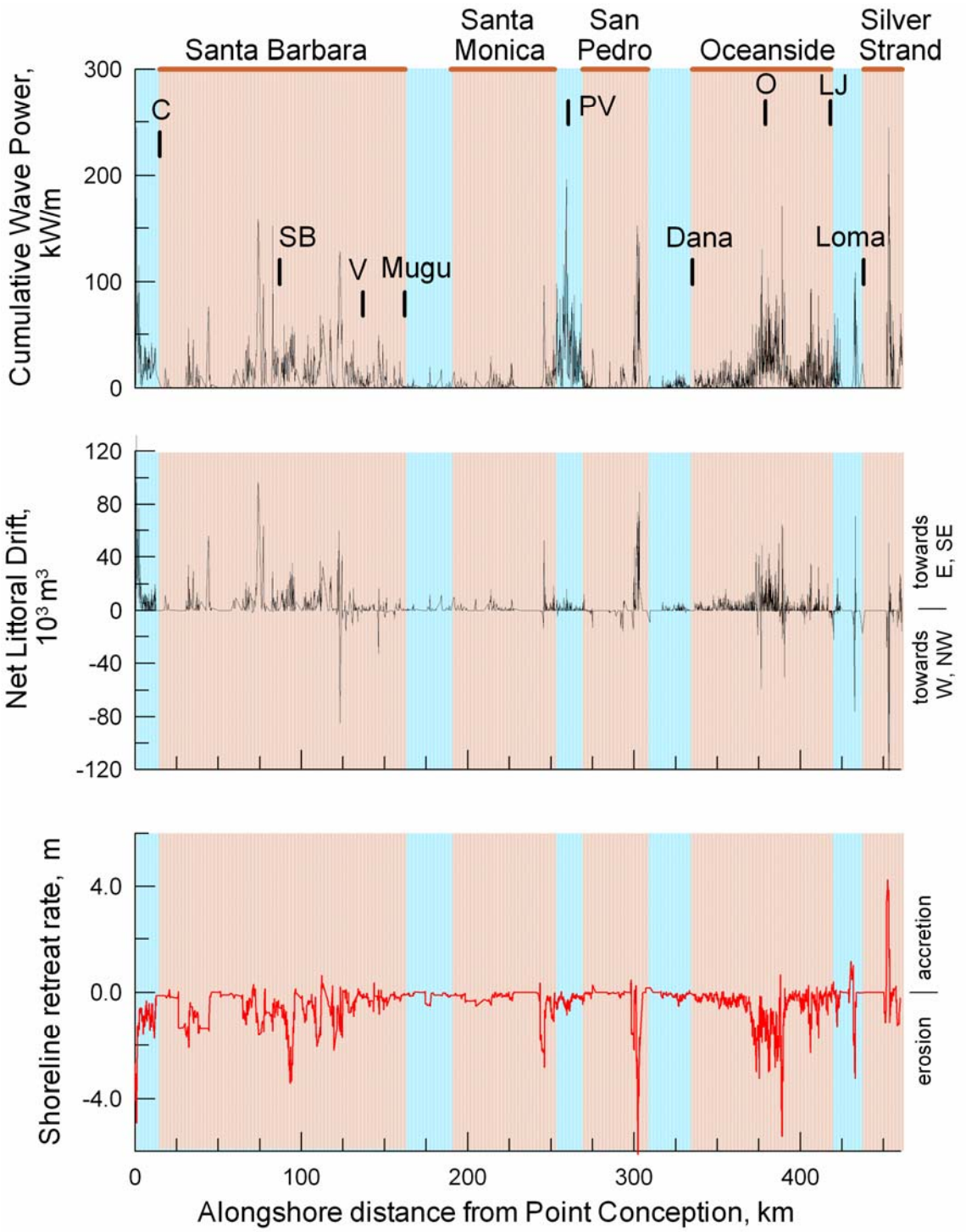

Figure 16: Erosion hot-spot analysis of Southern California Bight based on refraction/diffraction pattern from Figure 15. a) Annual cumulative wave energy flux, b) Annual net littoral drift, and c) Annual net change in the shoreline position(negative values represent erosion)

the 1998, with erosion hot-spots (regions of large negative values of dX/dt) occurring between Santa Barbara and Pt Mugu, near the southern ends of the Santa Monica and San Pedro Cells, and around the middle of the Oceanside Cell centered on Carlsbad, CA.

2.3 Wave Climate and Proxy Wave Records

The advective and diffusive fluxes of the erosion hot-spot analysis are controlled by the wave climate. Upon occasion, the typical seasonal weather cycles are abruptly and severely modified on a global scale. These intense global modifications are signaled by anomalies in the pressure fields between the tropical eastern Pacific Ocean and Australia/Malaysia known as the ***Southern Oscillation***. The intensity of the oscillation is often measured in terms of the ***Southern Oscillation Index (SOI)***, defined as the monthly mean sea level pressure anomaly in mb normalized by the standard deviation of the monthly means for the period 1951-1980 at Tahiti minus that at Darwin, Australia. The Southern Oscillation is in turn, modulated over multi-decadal periods by the ***Pacific Decadal Oscillation***, which results in alternating decades of strong and weak El Niño.

The long-term variability of the Pacific Decadal Oscillation (PDO) is shown in Figure 17 and the cumulative residual of the Southern Oscillation Index, between 1882 and 1996, is plotted in Figure 18. Southern Oscillation effects give rise to enhancements and protractions of the inter-annual seasonal cycles, and their two extremes are referred to as El Niño (SOI negative) and La Niña (SOI positive). Inspection of Figure 18 reveals a number of large positive oscillations in the SOI between 1944 and 1978 corresponding to La Niña dominated climate; and a series of very large negative oscillations occurring between 1978 and 1995 which

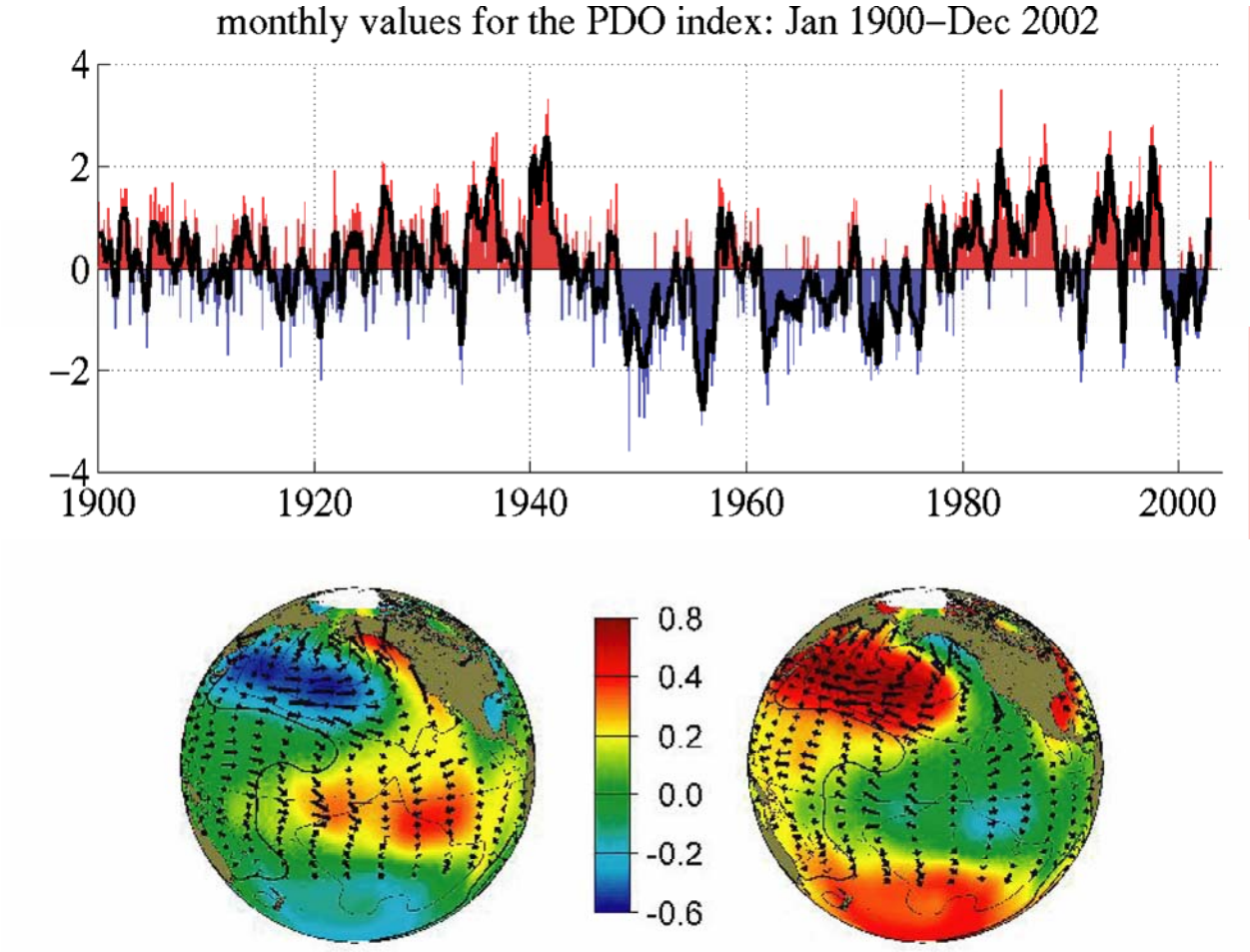

Figure 17. Typical wintertime Sea Surface Temperature (colors), Sea Level Pressure (contours) and surface wind stress (arrows) anomaly patterns during warm and cool phases of PDO.

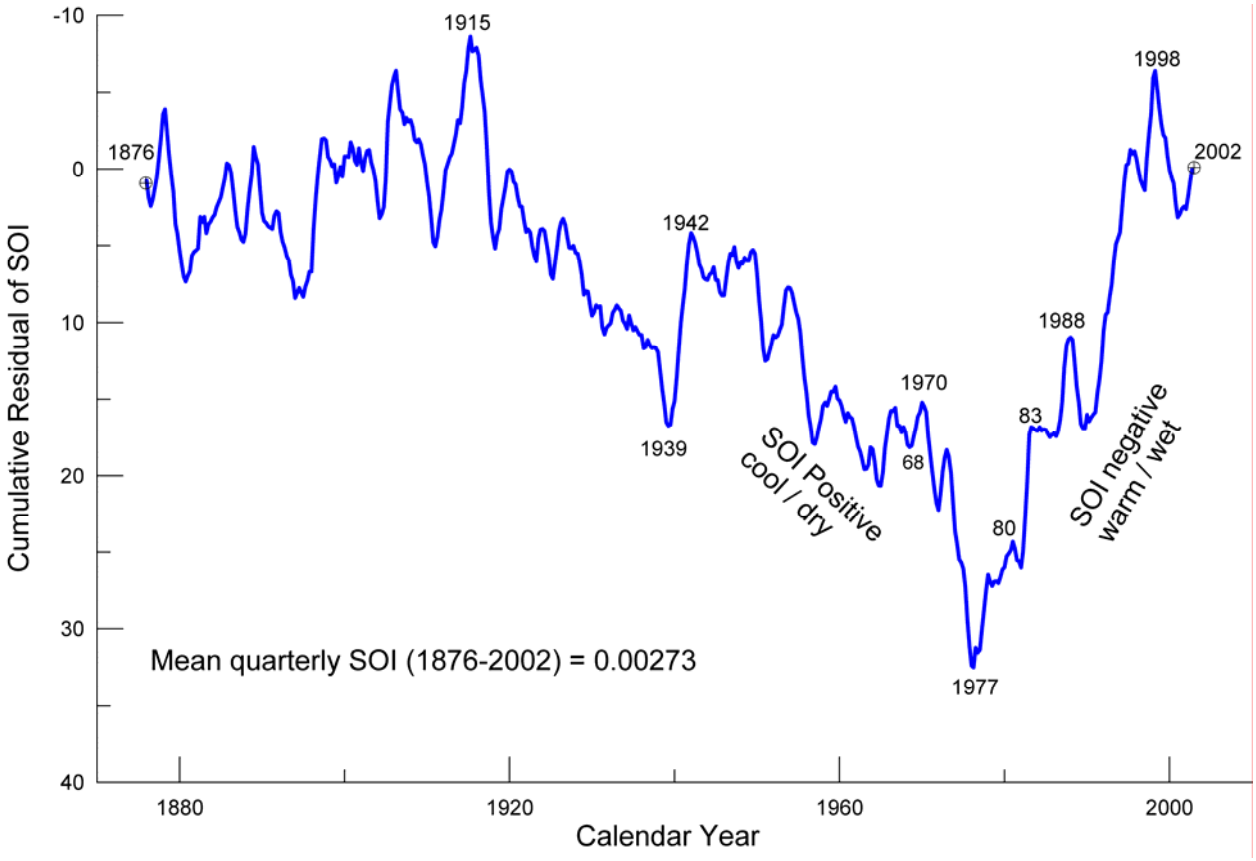

Figure 18. Cumulative residual of quarterly values of Southern Oscillation Index (SOI) [data from Australian Commonwealth Bureau of Meteorology].

correspond with El Niño dominated climate. Along the southern California coast, a period of mild-stable La Niña dominated pressure systems prevailed. The average SOI for this period was +0.1,with strong La Niña events in 1950, (SOI = +1.4); 1955/56, (+1.2); 1970/71, (+1.0); 1973/74, (+1.0); and 1975/76 (+1.4). Winters were moderate with low rainfall, and winds were predominantly from the west-northwest. The principal wave energy was from Aleutian lows having storm tracks which usually did reach southern California. Summers were mild and dry with the largest summer swells coming from very distant southern hemisphere storms.

The wave climate in southern California changed, beginning with the El Niño years of 1978/79 and extending at least until the present. The average SOI for this period was -0.5, with the 1978/79 El Niño averaging -1.2, the 1982/83 El

Niño averaging a record -1.7 and the 1993/94 El Niño recording a mean of -1.0. The prevailing northwesterly winter waves were replaced by high energy waves approaching from the west or southwest, and the previous southern hemisphere swell waves of summer have been replaced by shorter period tropical storm waves during late summer months from the more immediate waters off Central America. The net result appears to be a decrease in the southward component of the longshore transport of sand that had otherwise prevailed during the preceding thirty years.

Other strong El Niño events of the past have also been accompanied by extreme wave events, although none of these have been as sustained as the succession of El Niños from 1978 to 1995. The 1939/42 El Niño had an average SOI of -1.3 and was associated with a series of destructive wave events in the Southern California Bight, the most intense being the 24/25 September 1939 storm which seriously damaged the breakwater system at Long Beach, CA. The El Niño of 1904/05 had a mean SOI of -1.4 and was attended by a series of damaging west swells in March 1904 and again in March 1905 [Horrer, 1950; Marine Advisors, 1961].

We can quantify these wave climate trends by an analysis of 50 years of deep water wave hindcasts produced by Graham, (2003). This analysis is summarized in the cumulative residual analysis in Figure 19, revealing that waves were on average smaller and approached the Oceanside Cell from a more northerly directions during the cool-dry La Nina dominated period of the PDO between 1945 and 1977. Beginning with the onset of the warm-wet phase of PDO in 1978, waves approaching the Oceanside Cell from deep water increased in height and shifted to a more southerly direction, thereby decelerating the southward littoral drift.

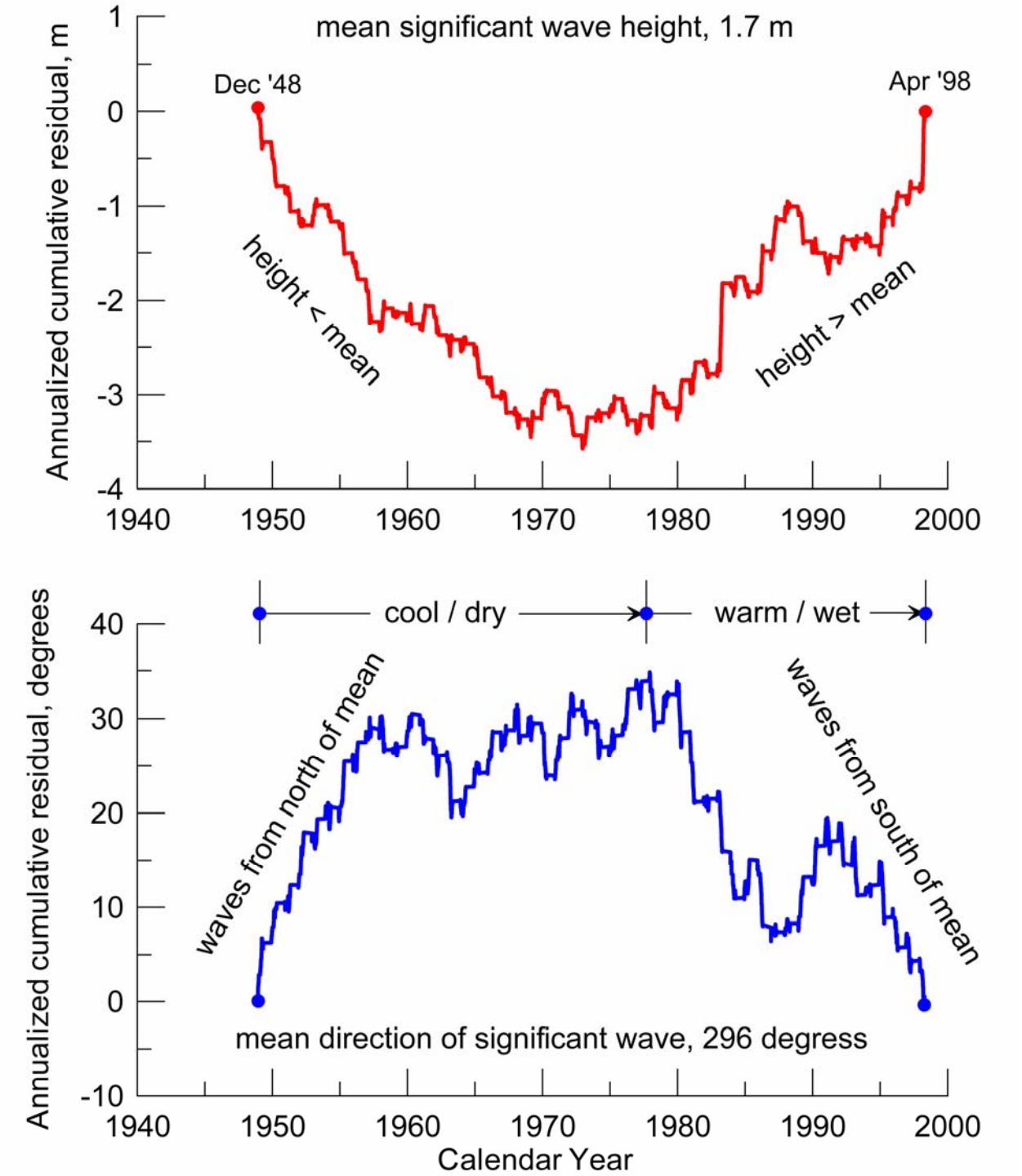

Figure 19. Cumulative residual time series of height and direction for 50 year record of North Pacific winter (5 month Dec-Apr) hindcast waves with 964 observations per year [data from Graham, 2002, station 33° N, 121.5° W].

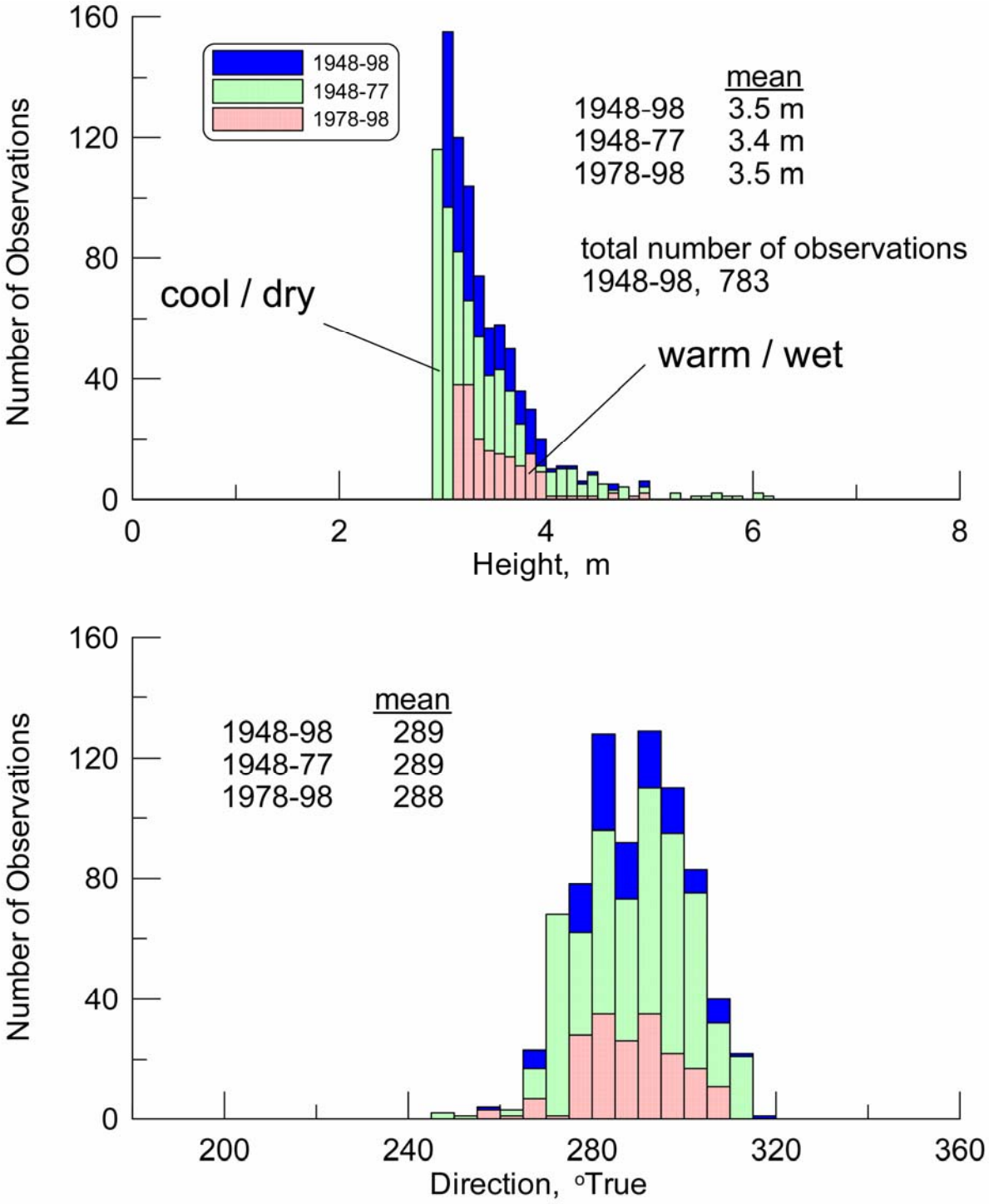

Figure 20. Comparison of height and direction of highest 5% of waves occurring during La Nina (SOI pos) conditions for 50 yr (1948 -98), 30 yr (1948-77) and 20 yr (1978-98) periods [data from Graham, 2003, at 33^{o} N, 121.5^{o} W].

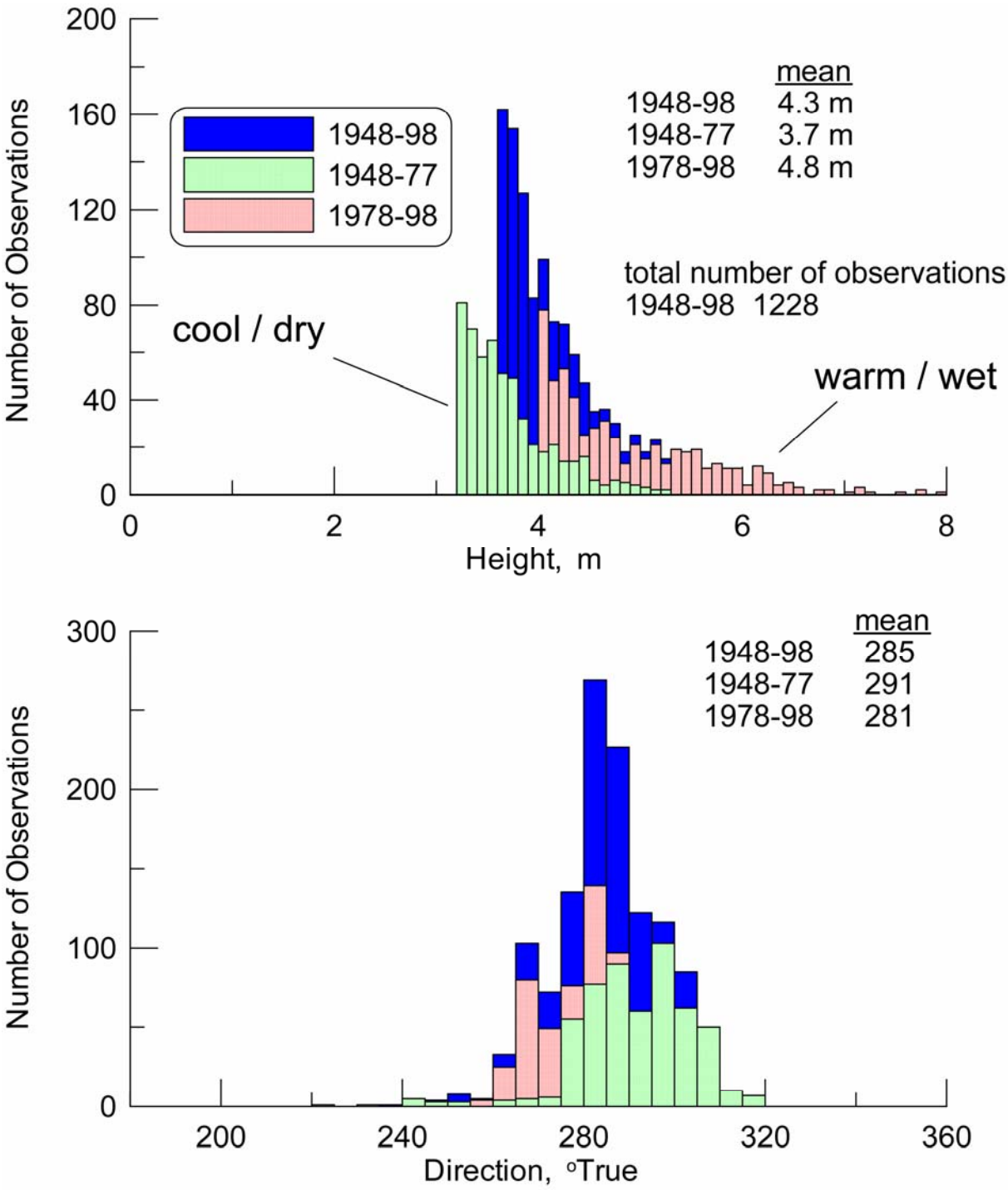

Figure 21. Comparison of height and direction of highest 5% of waves occurring during El Nino (SOI neg) conditions for 50 yr (1948 -98), 30 yr (1948-77) and 20 yr (1978-98) periods [data from Graham, 2003, at 33^{o} N, 121.5^{o} W].

In general, beach erosion is driven more by the highest waves than by the average waves. The histogram analysis in Figures 20 and 21 show that these same climate effects on wave height and direction also apply to the highest 5% of the waves occurring in any given climate period. This allows us to develop a characteristic proxy wave record for each climate state that can be looped in time for long term coastal evolution model simulations. To prepare these proxy wave records the **ptsal_histogram_percentile_soi.for** code (Appendix-F) was developed allowing the 50 year wave record of Graham (2003) to be sub-sampled according to user defined directional and energy characteristics. A similar code **cdip_histogram_percentile_soi.for** (Appendix-G) was developed to perform the same kind of sub-sampling on the 20 year CDIP wave record reconstructed in Figure 12. The input parameters output files which are required by **ptsal_histogram_percentile_soi.for** are:

alutian_wv1.txt…… *name of wave input file - ifile
sg_wv_48-98_soi.txt …… *name of soi input file - ifile2
wht_alu7898.txt …… *output file - ofile1
per_alu7898.txt …… *output file - ofile2
dir_alu7898.txt …… *output file - ofile3
wht95_alu7898.txt …… *output file - ofile4
dir95_alu7898.txt …… *output file - ofile5
soi_alu7898.txt…… *output file - ofile6
soi95_alu7898.txt …… *output file - ofile7
per95_alu7898.txt…… *output file - ofile8
80 nbins1…….. *number of bins in histogram - variable #1
0.1 binw1……... *width of each histogram bin - variable #1
0.1 …… st1 *starting point of first bin - variable #1

20 ……. nbins2 *number of bins in histogram - variable #2
1 …….. binw2 *width of each histogram bin - variable #2
1.0 ……. st2 *starting point of first bin - variable #2
36 …….. nbins3 *number of bins in histogram - variable #3
5.0 …….. binw3 *width of each histogram bin - variable #3
185.0 …….. st3 *starting point of first bin - variable #3
95.0 …….. cumthr *threshold of target wave
80 …….. nbins4 *number of bins in histogram - variable #4
0.1 …….. binw4 *width of each histogram bin - variable #4
0.1 …….. st4 *starting point of first bin - variable #4
36 …….. nbins5 *number of bins in histogram - variable #5
5.0…….. binw5 *width of each histogram bin - variable #5
185.0 …….. st5 *starting point of first bin - variable #5
20 …….. nbins6 *number of bins in histogram - variable #6
1 …….. binw6 *width of each histogram bin - variable #6
1.0 …….. st6 *starting point of first bin - variable #6 "
19471201 ……*jst 10000 less than actual start of 1st year integer
19480401 ……*jnd 10000 less than actual end of 1st year integer
1……*jsign soi index (positive = 1) or (negative = -1) (zero = 0)
19781201……*nst_date first 8 digit integer date record in histogram
19980401…… *nnd_date last 8 digit integer date record in histogram
1 …….. *n_soi if 0 evaluate based on SOI, if 1 use all data

The **ptsal_histogram_percentile_soi.for** code was used to sub sample the 50 yr wave record of Graham (2002) to determine the probability density functions (histograms) for the height, period direction and cumulative wave power of the winter time storm waves from the Aleutian Low source (Figure 22) We find that

these waves are commonly 3 to 4m high in the open sea with periods typically 14 to 16 sec. They approach the Southern California Bight from a mean direction of 300^0, so much of the 105 kW/m incident wave power is shadowed by the channel islands and southward facing orientation of the coast (ala, Figure 15). However, the Graham 2003 hindcasts only project the energy from waves generated 1 December to 1 April each year. To fill in the remainder of the year we perform similar source constructions by sub-sampling the CDIP data base. These are done using the **cdip_histogram_percentile_soi.for** codes (Appendix-G) . The input parameters output files which are required by **ptsal_histogram_percentile_soi.for** are:

dp_80-00.txt……. *name of wave input file - ifile
cdip_80-00_soi.txt……. *name of soi input file - ifile2
wht_1980-98.txt……. *output file - ofile1
per_1980-98.txt……. *output file - ofile2
dir_1980-98.txt……. *output file - ofile3
wht95_1980-98.txt ……. *output file - ofile4
dir95_1980-98.txt……. *output file - ofile5
soi_1980-98.txt ……. *output file - ofile6
soi95_1980-98.txt ……. *output file - ofile7
per95_1980-98.txt ……. *output file - ofile8
80 nbins1……. *number of bins in histogram - variable #1
0.1 binw1 ……. *width of each histogram bin - variable #1
0.1 st1 ……. *starting point of first bin - variable #1

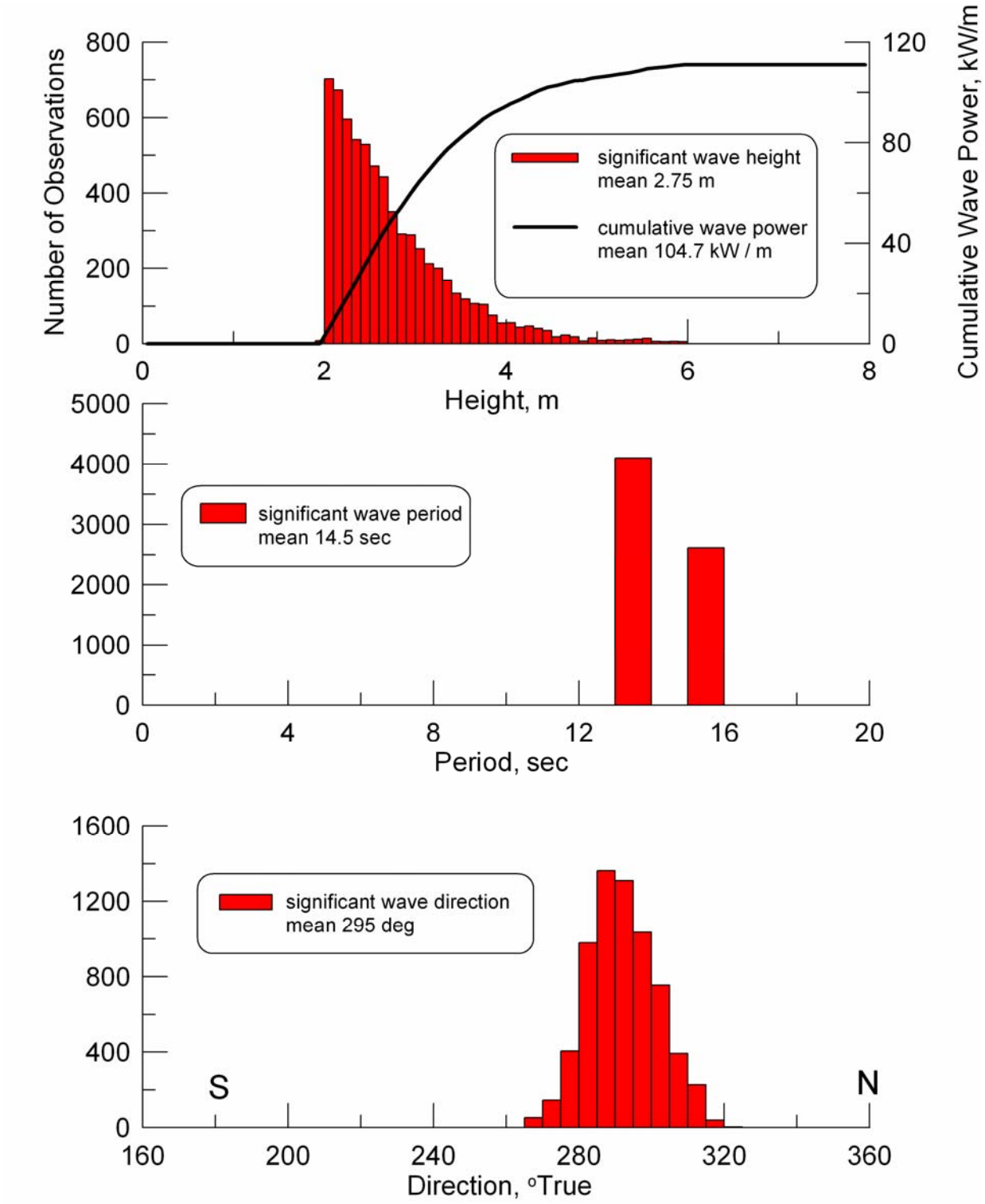

Figure 22. Histogram of Aleutian Low subset of 50 year (1948-1998) hindcast of significant wave height, power, period, and direction, 6710 observations. [data from Graham, 2003 at 33° N, 121.5° W]

20 ……. nbins2 *number of bins in histogram - variable #2
1 ……. binw2 *width of each histogram bin - variable #2
1.0……. st2 *starting point of first bin - variable #2
36 ……. nbins3 *number of bins in histogram - variable #3
5.0 ……. binw3 *width of each histogram bin - variable #2
185.0……. st3 *starting point of first bin - variable #3
95.0 ……. cumthr *threshold of target wave
80 ……. nbins4 *number of bins in histogram - variable #4
0.1……. binw4 *width of each histogram bin - variable #4
0.1……. st4 *starting point of first bin - variable #4
36……. nbins5 *number of bins in histogram - variable #5
5.0……. binw5 *width of each histogram bin - variable #5
185.0 ……. st5 *starting point of first bin - variable #5
20 ……. nbins6 *number of bins in histogram - variable #6
1……. binw6 *width of each histogram bin - variable #6
1.0 ……. st6 *starting point of first bin - variable #6
1979.0 ……. *ajst 1 year less than actual start of 1st year
1980.0 ……. *ajnd 1 year less than actual end of 1st year
-1 ……. *jsign soi index (positive = 1) or (negative = -1) (zero = 0)
1980.000 ……. *st_date first date record in histogram
1998.246 ……. *end_date last date record in histogram
1……. *n_soi if 0 evaluate based on SOI, if 1 use all data
1.4 …… *akn *correction factor for wht north waves inside to ouside bight
2.0 ……..*aks *correction factor for wht south waves inside to ouside bight
0.5 ……...*adn *correction factor for dir north waves inside to ouside bight
1.3 …… *ads *correction factor for dir south waves inside to ouside

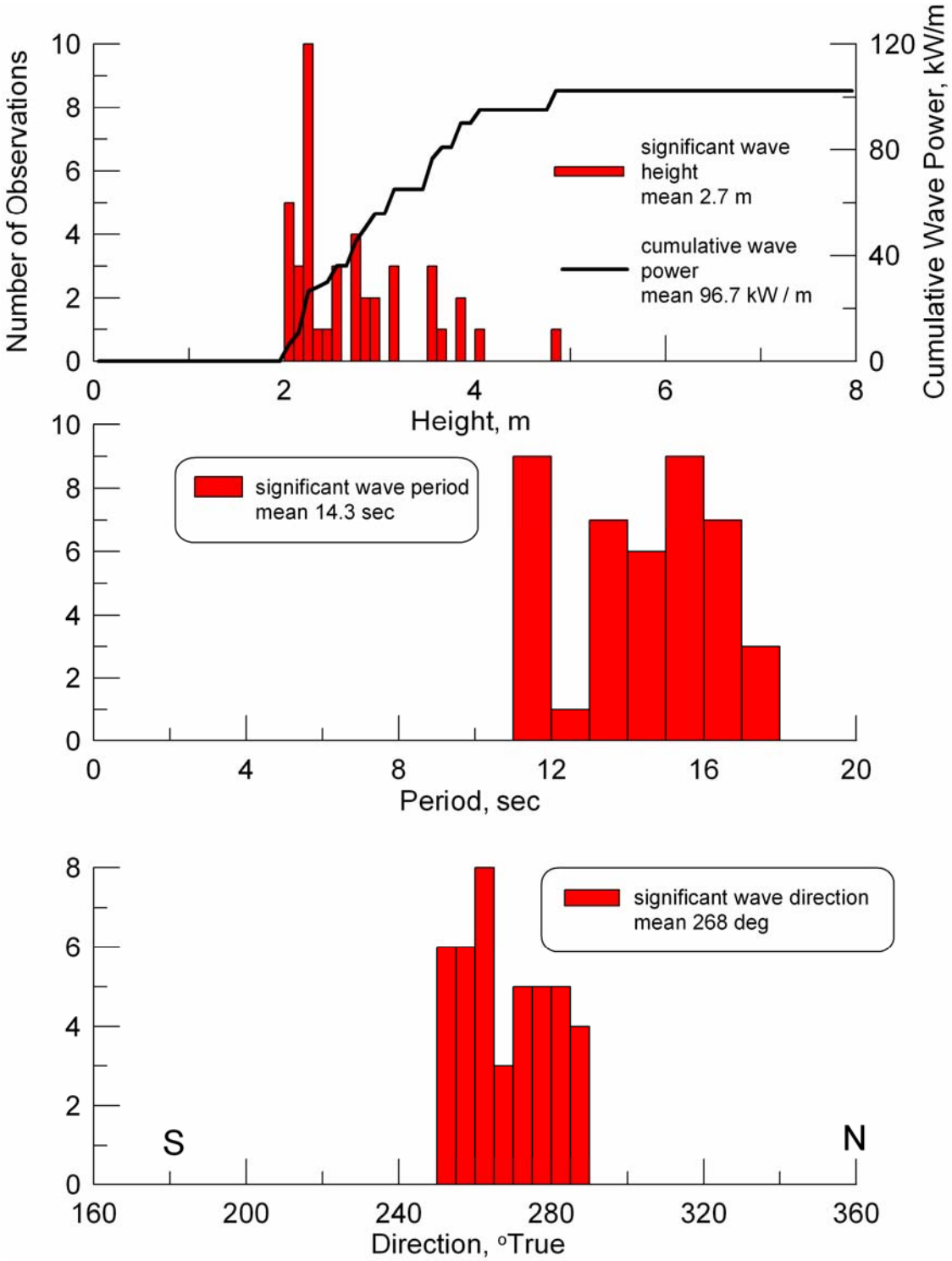

Figure 23. Histogram of Aleutian Low subset of 18 year (1980-1998) CDIP record of significant wave height, power, period, and direction, 42 observations. [after Inman & Jenkins, 2002 corrected to 33° N, 120° W]

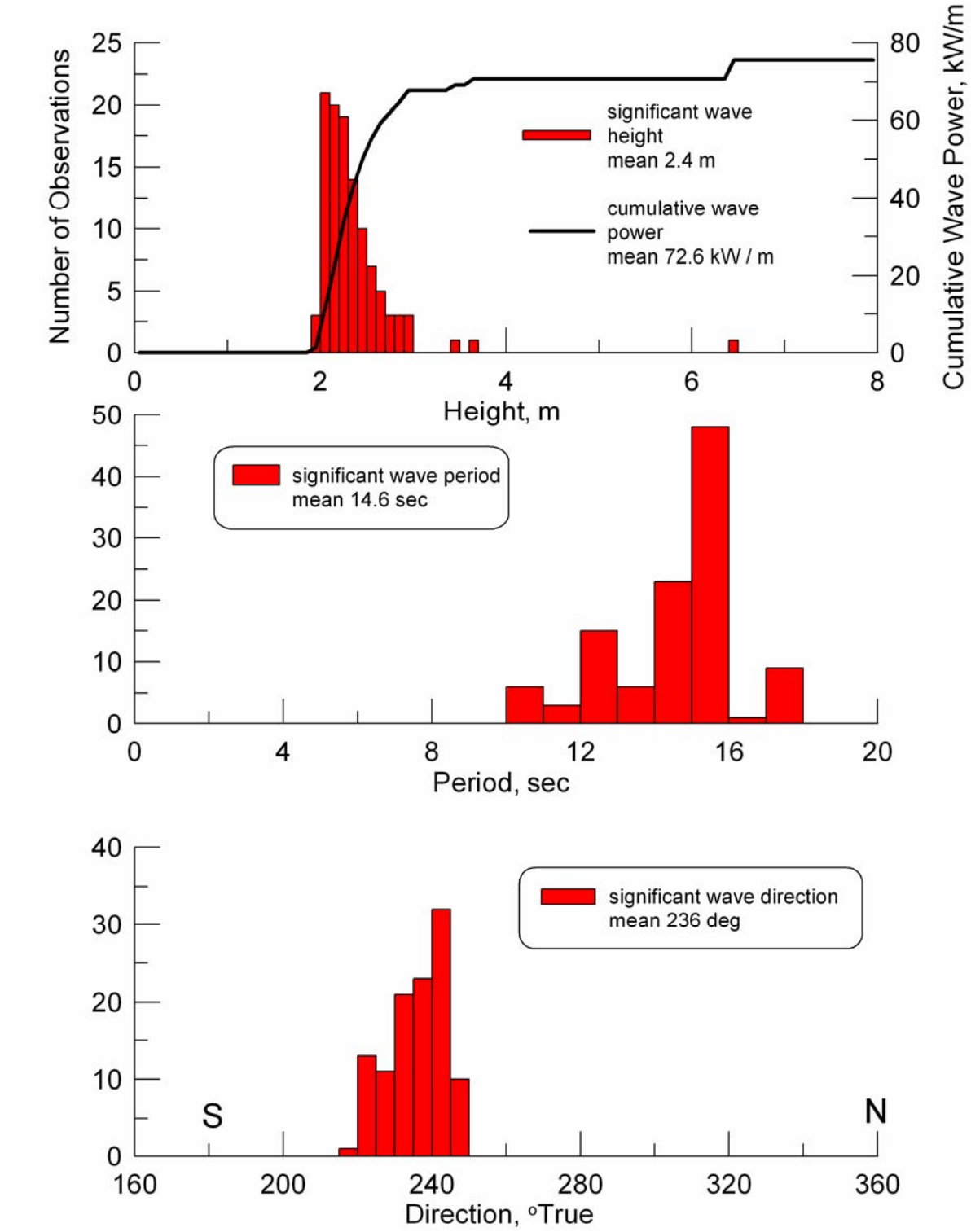

Figure 24. Histogram of Pineapple Express subset of 18 year (1980-1998) CDIP record of significant wave height, power, period, and direction, 111 observations. [after Inman & Jenkins, 2002 corrected to 33° N, 120° W]

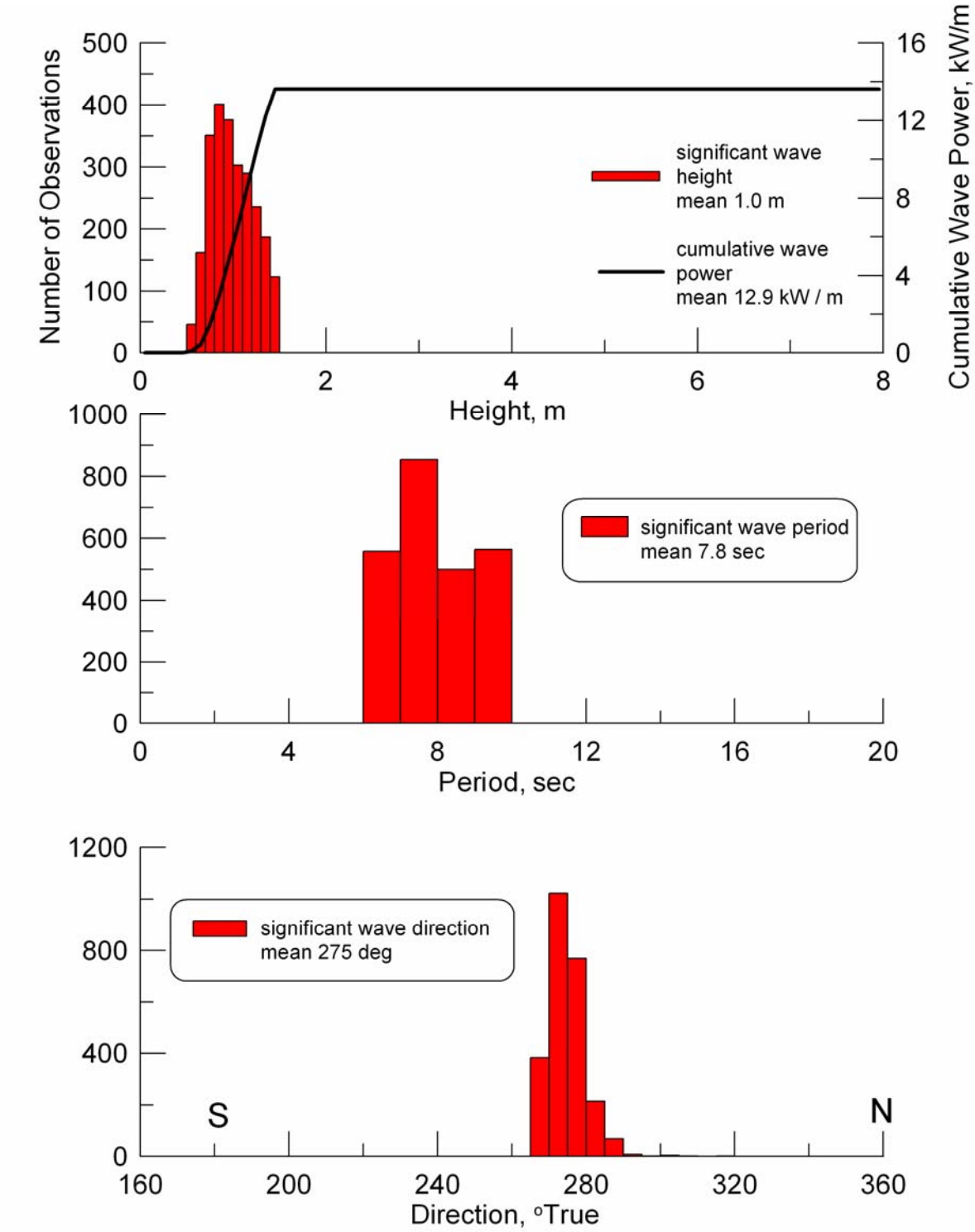

Figure 25. Histogram of North Pacific High subset of 18 year (1980-1998) CDIP record of significant wave height, power, period, and direction, 42 observations. [after Inman & Jenkins, 2002 corrected to 33° N, 120° W]

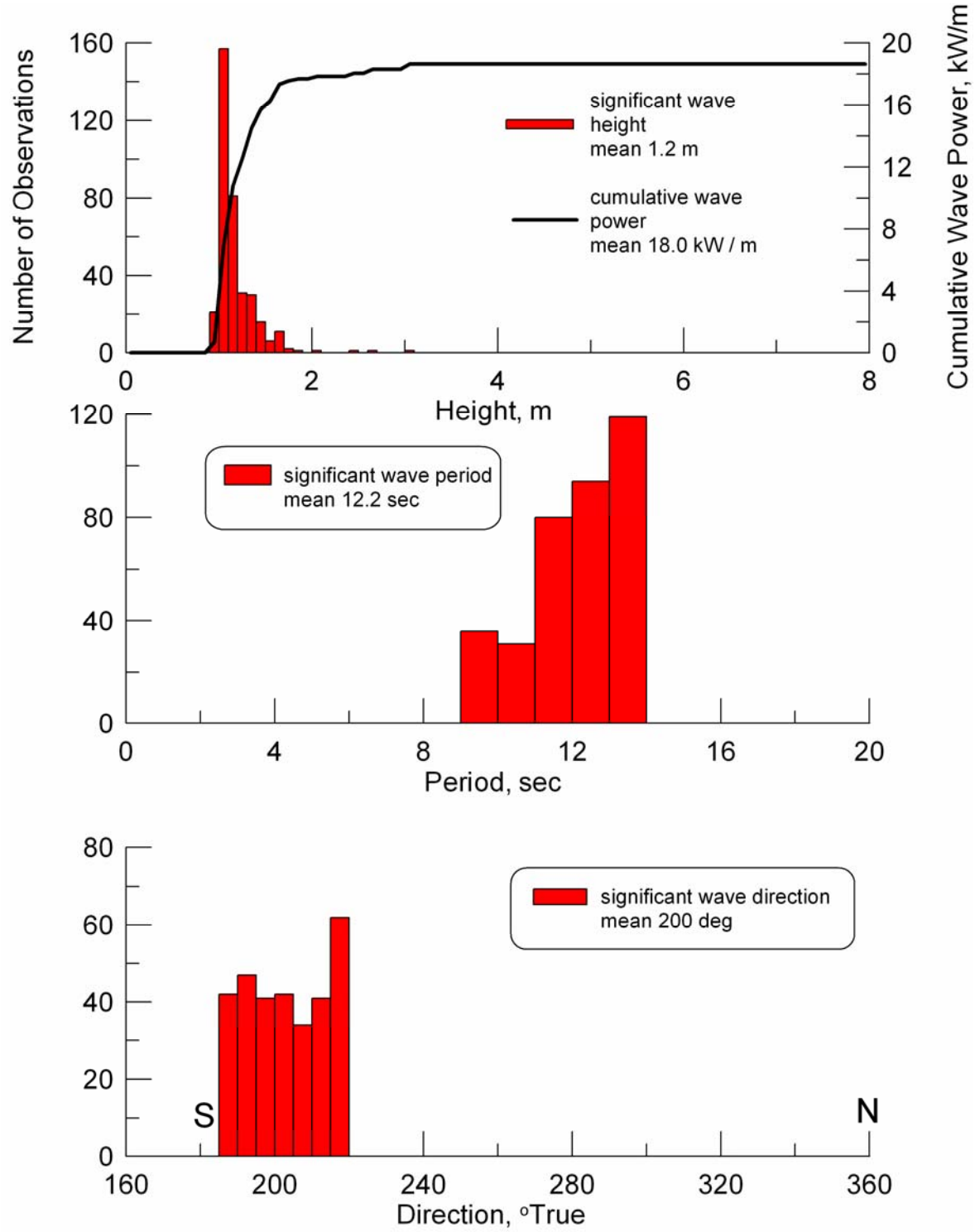

Figure 26. Histogram of Tropical Storm subset of 18 year (1980-1998) CDIP record of significant wave height, power, period, and direction, 360 observations. [after Inman & Jenkins, 2002 corrected to 33° N, 120° W]

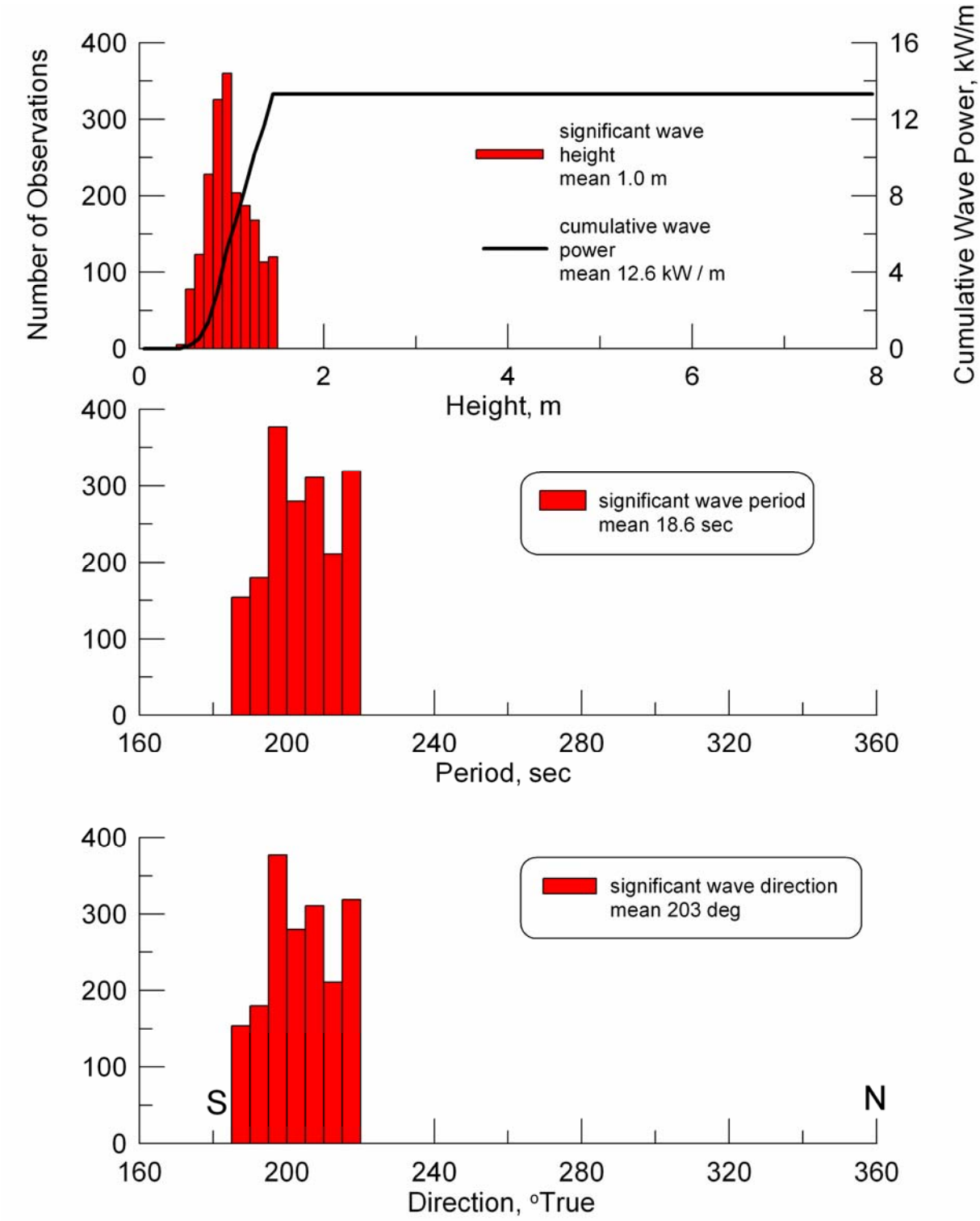

Figure 27. Histogram of Southern Hemisphere Swell subset of 18 year (1980-1998) CDIP record of significant wave height, power, period, and direction, 1912 observations. [after Inman & Jenkins, 2002 corrected to 33° N, 120° W]

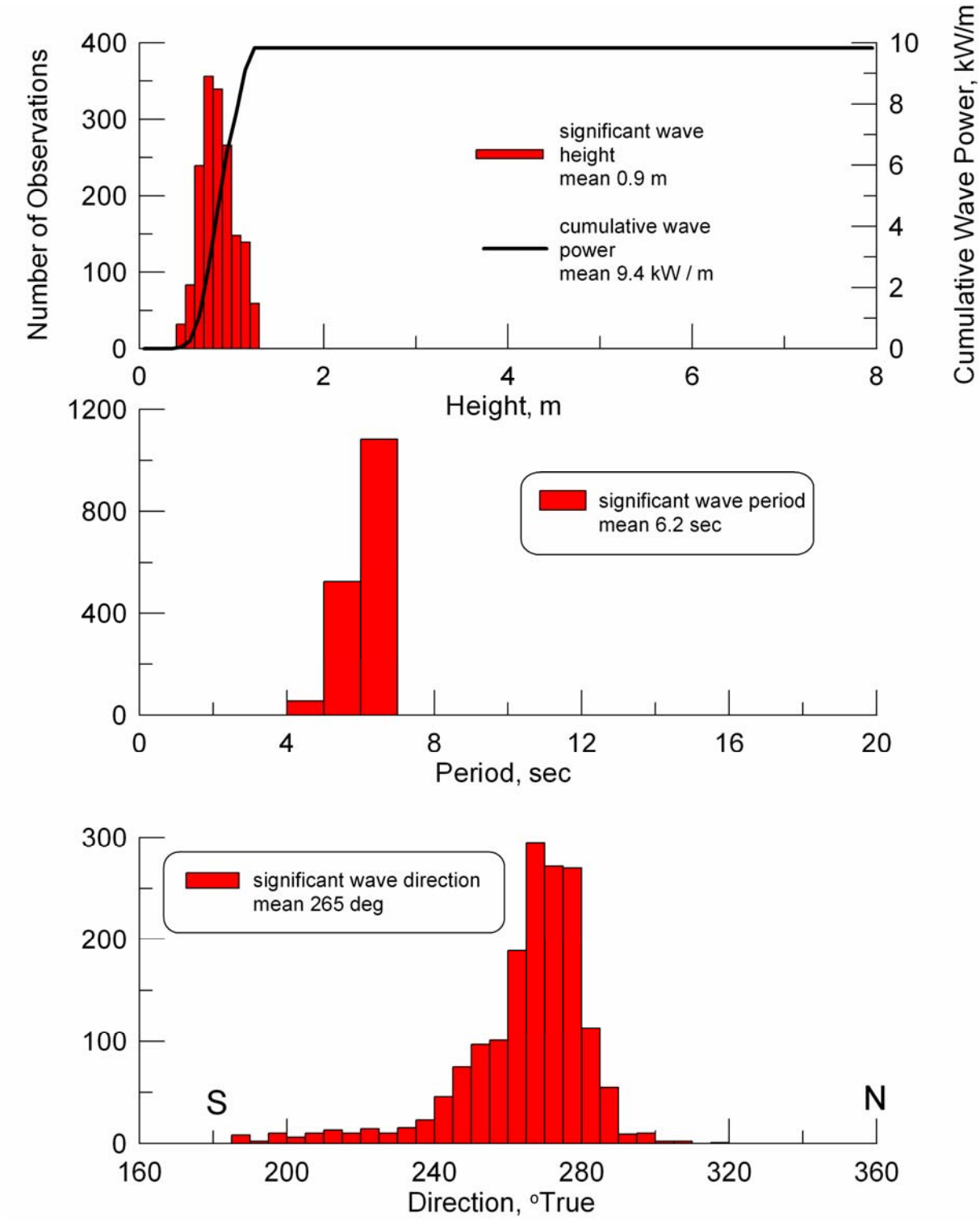

Figure 28. Histogram of Sea Breeze subset of 18 year (1980-1998) CDIP record of significant wave height, power, period, and direction, 1662 observations. [after Inman & Jenkins, 2002 corrected to 33° N, 120° W]

Applying the **cdip_histogram_percentile_soi.for** code to the 20 year CDIP wave record (Figure 15) produces the alternative probability density function for the Aleutian Low waves shown in Figure 23. Because these waves are derived from observations inside the Southern California Bight, the wave heights and cumulative wave power are reduced somewhat relative to Figure 22, and the directional spread is more westerly. The year-round observational window of the CDIP wave monitoring also picks up the presence of shorter period waves (typically10 sec). The **cdip_histogram_percentile_soi.for** code was also used to complete the portfolio of waves for the proxy wave record to include: waves due to frontal cyclones tracking toward the Bight from waters east of Hawaii (Pineapple Express, Figure 24), wind swells generated by the North Pacific High (Figure 25), waves generated from tropical cyclones west of Central America typically during summer (Figure 26), long waves generated by extra-tropical storms in the Southern Hemisphere (Figure 27), and local wind waves from diurnal pressure gradients over the Southern California Bight (Figure 28). These probability density functions in Figures 23-28 are used to determine the statistical mix of waves in synthesizing a 200- year long proxy wave record for simulating future coastal evolution.

2.4 Sealevel Effects on Refraction/Diffraction

Here we apply the sealevel algorithms from Figure 4, Section 1.1 to the **oceanrds_socal.for** code to determine how refraction of proxy waves are effected by sea level change. The sea level function in Figure 4 for any arbitrary age less than 18,000 years BP is calculated by the code **sea_level_waz.for** found in APPENDIX-H. No input file is need to run this code as it provides screen prompts for all input ages and sealevel outputs. The relevant input parameters in **oceanrds_socal.for** that accept the sealevels from **sea_level_waz** is **sealev**. A contrast between refraction/diffraction in The Southern California Bight during

present sea level versus sealevel during the Younger Dryas (-54 m) is shown in Figures 29 and 30. In Figure 30, the present shoreline from Figure 29 is shown as a solid black line. The shelf and banks which have been laid bare by lowered sealevel in Figure 30 appear as the white areas extending beyond the present shoreline contour. The result of this lowered sealevel is a considerable increase in the size of the channel islands, thereby increasing the degree of island sheltering in the refraction/diffraction pattern in the upper Bight. As a consequence, the average energy flux reaching the shoreline in the upper Bight is reduced from 127 W/m during present sealevel, to 99 W/m during sealevels of the Younger Dryas (occurring 12 ka). In the lower Bight, reduced sealevel reduces the depths over the shallow banks along the continental margin, allowing these banks to have a greater influence on refracted wave direction at great distance from the shoreline. The result of this is greater directional spreading of incoming wave energy in the lower Bight, with more intense beam forming, particularly in the Oceanside Cell. As a consequence, lowered sea level slightly increases the average energy flux reaching the shoreline in the upper Bight from 612 W/m during present sealevel, to 624 W/m during Younger Dryas sea level. These variations in energy flux precipitate changes in the equilibrium profile of the sediment cover.

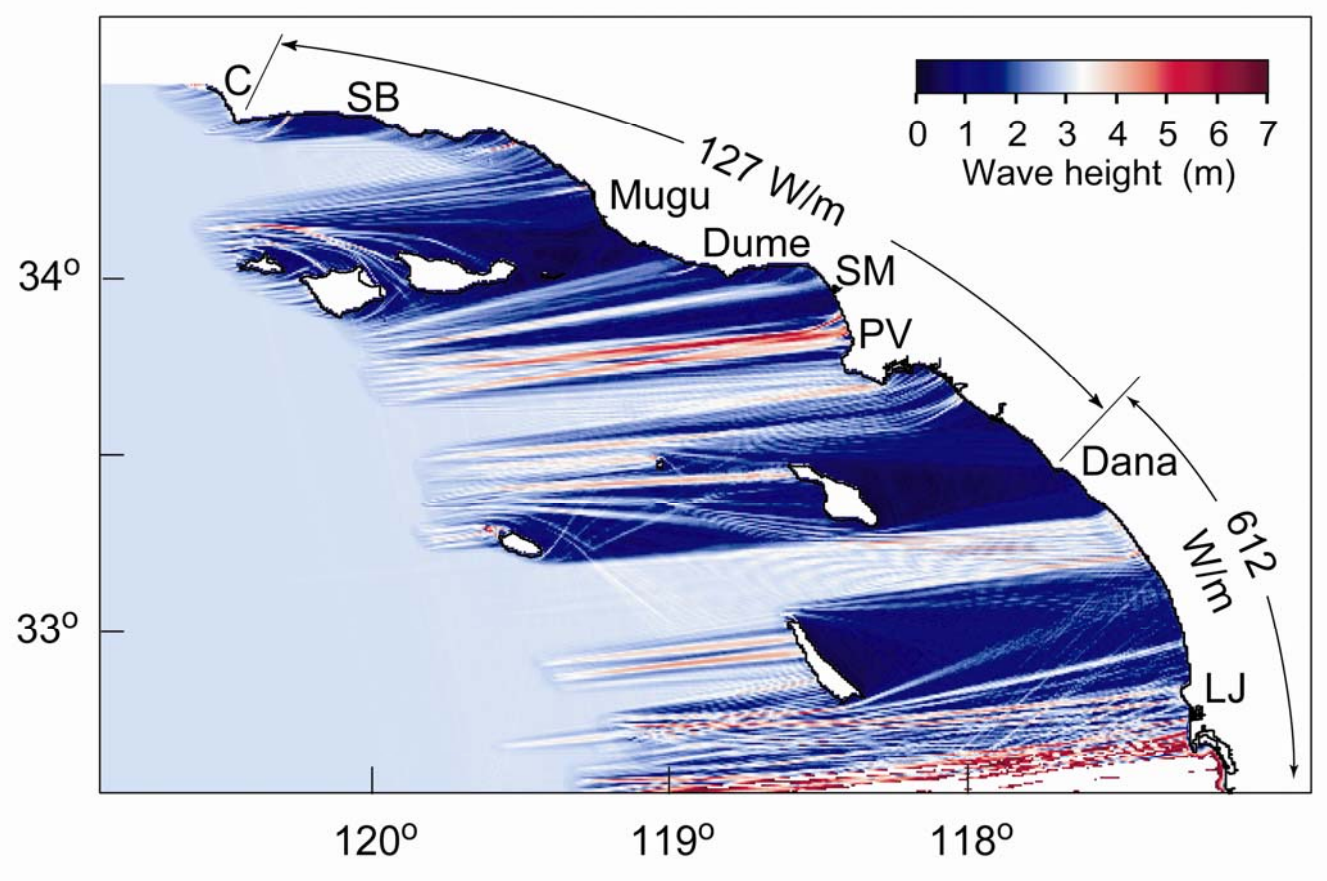

Figure 29: Refraction of proxy wave record for present sealevel (0 m MSL*)*

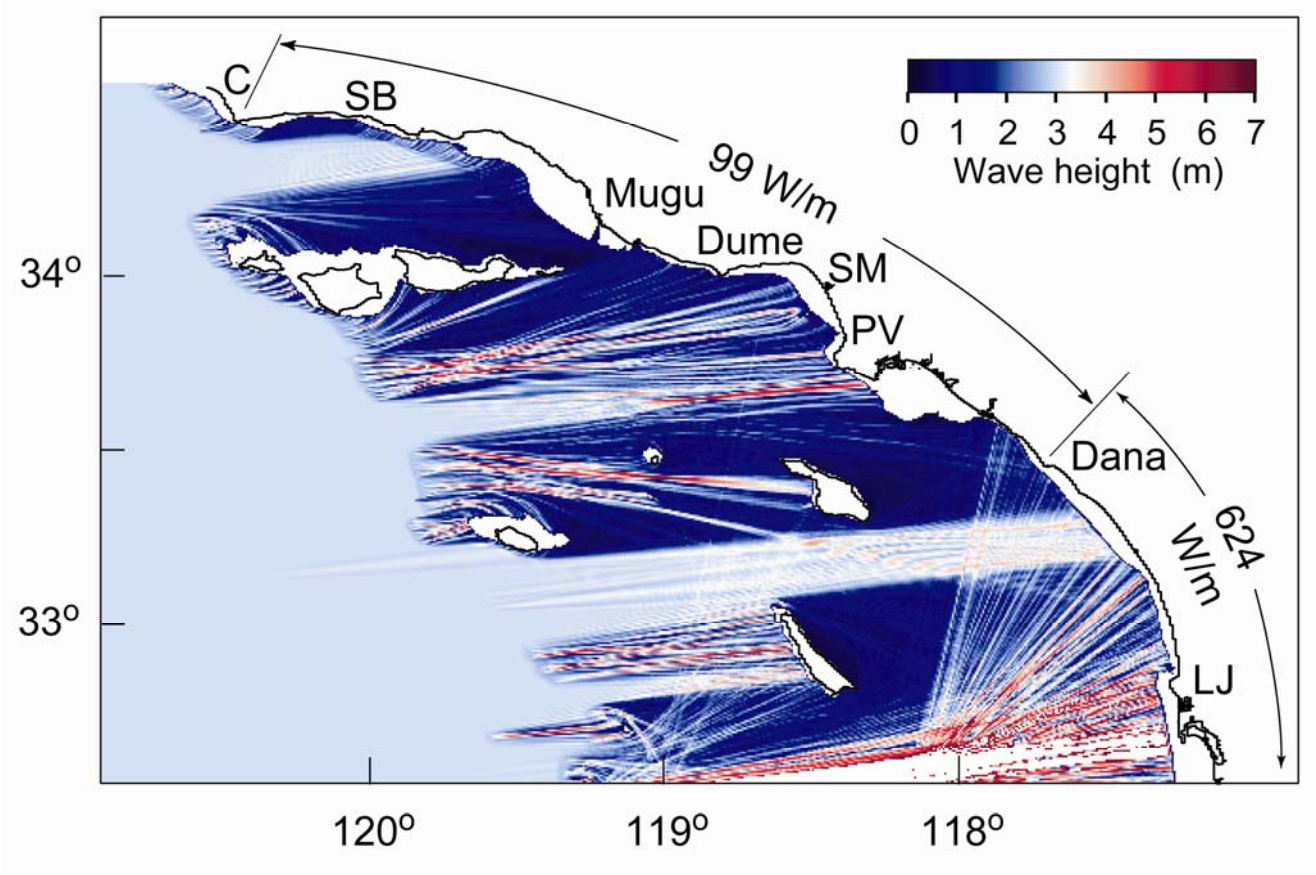

Figure 30: Refraction of proxy wave record during Younger Dryas sealevel (-54 m)

2.5 Equilibrium Profiles of the Sediment Cover

Having specified the terms of the sediment continuity equation for the LCM in Sections 2.1-2.4, we now proceed with solving for the shape of the equilibrium profile of the sediment cover (shown in Figure 3b). The seaward boundary of the shorezone is a vertical plane at the critical closure depth $\hat{h}_c$ (Figure 31a) corresponding to the maximum incident wave [e.g., *Kraus and Harikai*, 1983]. The landward boundary is a vertical plane at the berm crest (cross), a distance $\hat{X}_1$ from a bench mark. The cross-shore length of the system from the berm crest to

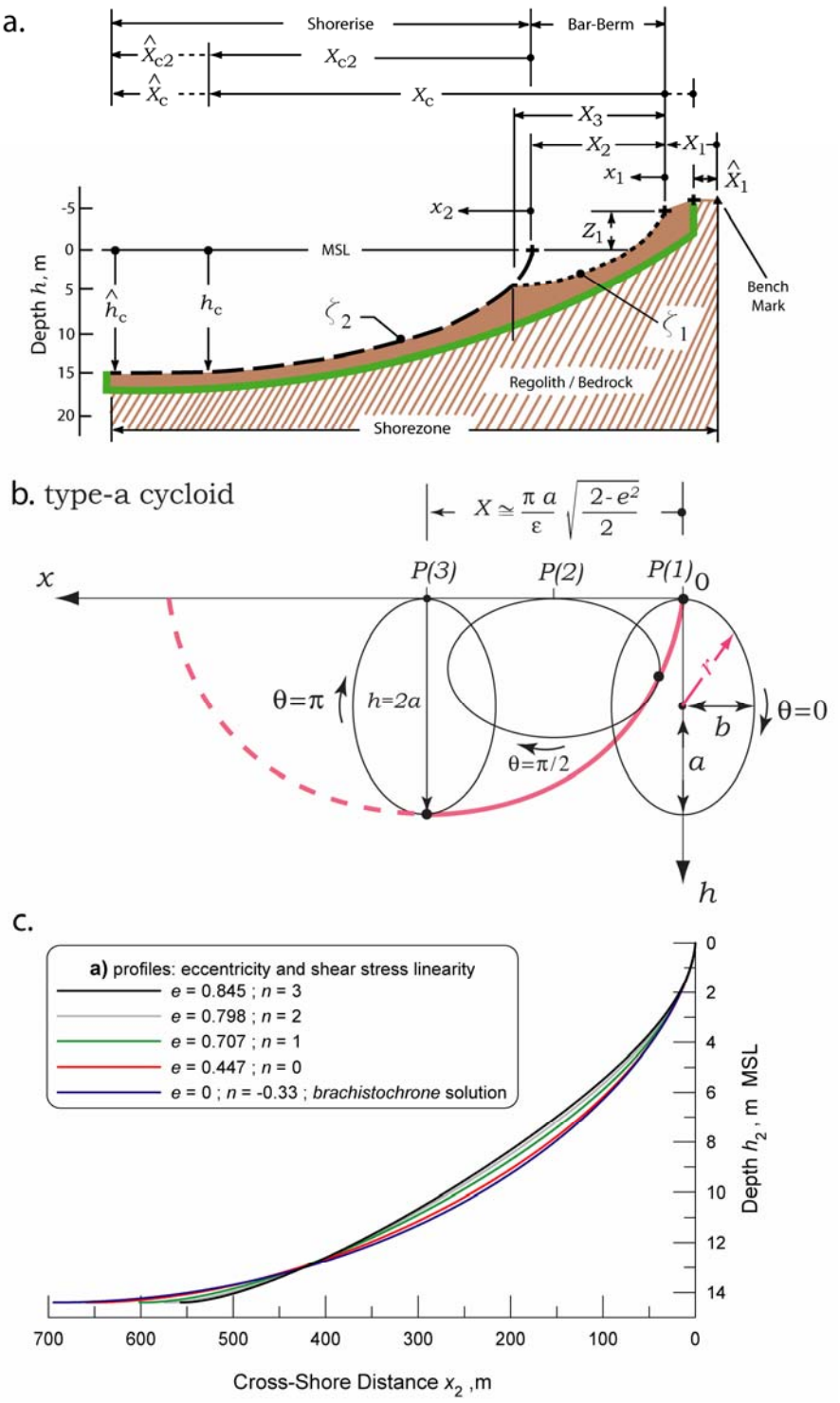

Figure 31. Equilibrium beach profile a) nomenclature, b)elliptic cycloid, c) Type-a cycloid solution.

closure depth is $\hat{X}_c$. The distance from the point of wave breaking to closure depth is $\hat{X}_{c2}$ such that $\hat{X}_c = \hat{X}_{c2} + \hat{X}_2$, where $\hat{X}_2$ is the distance from the berm crest to the origin of the shorerise profile near the wave breakpoint. We consider equilibrium over time scales that are long compared with a tidal cycle and profiles that remain in the wave dominated regime where the relative tidal range (tidal range/H) < 3 [*Short*, 1999]. Under these conditions, the curvilinear coordinate that defines the profile referenced to mean sea level (MSL) vertical datum is,

$$d\zeta = \sqrt{(dx)^2 + (dh)^2} = \sqrt{1 + x'^2}\ dh = \sqrt{1 + h'^2}\ dx$$
$$x' = \frac{dx}{dh} \quad ; \quad h' = \frac{dh}{dx} \tag{13}$$

where $d\zeta$ is calculated separately for inner (bar-berm, $d\zeta_1$) and outer (shorerise, $d\zeta_2$) portions of the conjoined profile.

Fluxes of energy into and out of the shorezone system are shown by arrows crossing the system boundaries in Figure 31a. Work W per unit of longshore distance y is performed on the system by the incident waves that provide energy to the system at a rate given by

$$\frac{\mathrm{d}W}{\mathrm{d}t} = \left[EC_g\right]_{x=X_c}$$

where $E = \rho g H^2/8$ is energy per unit longshore surface area, ρ and g are water density and acceleration of gravity, C_g is wave group velocity, and H is local rms wave height. The waves shoal and break inside the shorezone system, dissipating wave energy into an increment of heat dQ. This evolution of heat produces an incremental entropy change

$$\mathrm{d}S = \frac{\mathrm{d}Q}{T_\mathrm{a}}$$

where T_a is absolute temperature. Heat is removed from the shorezone system to the surroundings primarily by advection and turbulent diffusion in the nearshore circulation system [e.g., rip currents etc., *Inman et al.*, 1971] and secondarily through heat of vaporization in sea spray.

The second law of thermodynamics (often referred to as 'the entropy law') is a necessary condition for equilibrium and requires that a natural process that starts in one equilibrium state and ends in another will cause the entropy of the system plus its surroundings (universe) to increase,

$$\left.\frac{\partial S}{\partial t}\right)_{\mathrm{UNIVERSE}} = \left.\frac{\partial S}{\partial t}\right)_{\mathrm{SYSTEM}} + \left.\frac{\partial S}{\partial t}\right)_{\mathrm{SURROUNDING}} > 0 \qquad (14)$$

The decisive issue with respect to the thermodynamic state of the shorezone system is the fate of the heat evolved within it and whether the entropy increase associated with that heat evolution is retained by the system or exported to its surroundings. We adopt a heat transport/ entropy production formulation for the shorezone system that is an analogue of that used to describe dissipation in global climate state models [*Paltridge*, 1975, 1978; *Ozawa et al*., 2001, 2003]. The derivation for entropy production in a fluid system is found in *de Groot and Mazur* [1984] and *Landau and Lifshitz* [1980] and can be written,

$$\left.\frac{\partial S}{\partial t}\right)_{\mathrm{UNIVERSE}} = \int \frac{1}{T_\mathrm{a}}\left[\frac{\partial(\rho c_\mathrm{v} T_\mathrm{a})}{\partial t} + \nabla\cdot(\rho c_\mathrm{v} T_\mathrm{a} u) + p\nabla\cdot u\right] dV + \int \frac{q\cdot n_\mathrm{r}}{T_\mathrm{a}}\, dA \qquad (15)$$

where c_v is the specific heat at constant volume, u is the fluid velocity, p is the fluid pressure, q is the diabatic heat flux taken as positive when occurring outward across system boundaries and n_r is the unit normal vector on the system boundary. The volume integral in (15) is the rate of change of entropy of the fluid system and represents the first term on the right side of (14). The surface integral in (15) is taken over the system boundary (green line in Figure 31a) and represents the discharge rate of entropy into the surroundings due to heat flux across the system boundary. When a fluid system is in a steady state, *Chandrasekhar* [1961] has shown that the first law of thermodynamics reduces the volume integral in (15) to:

$$\left.\frac{\partial S}{\partial t}\right)_{\text{SYSTEM}} = -\int \frac{1}{T_a} \nabla \cdot q \, \mathrm{d}V + \int \frac{\Phi}{T_a} \, \mathrm{d}V \tag{16}$$

where Φ is the dissipation function representing the rate of viscous dissipation of kinetic energy per unit volume. The first term on the right side of (16) represents the entropy change due to transport of latent heat by advection and diffusion. If latent heat is transported out of the system (q positive), the system losses entropy. Because entropy is a state function of the system, it must remain constant if the system is to achieve equilibrium [*Landau and Lifshitz*, 1980]. Therefore, any equilibrium fluid system that exports latent heat to its surroundings must compensate for the associated entropy loss through the production of new entropy at an equivalent rate.

When heat fluxes across the system boundary, the entropy of the surroundings changes at a rate given by the surface integral in (15). This surface integral can be expressed in terms of a volume integral through the application of Gauss's theorem, giving the entropy change of the surroundings in terms of heat fluxes within the system volume

$$\left.\frac{\partial S}{\partial t}\right)_{\text{SURROUNDING}} = \int \frac{q \cdot n_{\text{r}}}{T_{\text{a}}}\, dA = \int \frac{1}{T_{\text{a}}} \nabla \cdot q dV + \int q \cdot \nabla\left(\frac{1}{T_{\text{a}}}\right) dV \qquad (17)$$

The first term on the right side of (17) is the entropy change occurring in the surroundings due to the latent heat that was imported from the system, while the second is due to heat conduction along temperature gradients formed within the system between regions of hot and cold. Entropy changes in the surroundings due to latent heat transport are equal and opposite in sign to those occurring in the system (16), and taken together, produce no net change in the total entropy of the universe. Instead, the entropy of the universe can only be changed by temperature gradients and viscous dissipation occurring within a fluid system, as found after inserting (16) and (17) in (14),

$$\left.\frac{\partial S}{\partial t}\right)_{\text{UNIVERSE}} = \int \frac{\Phi}{T_{\text{a}}}\, dV + \int q \cdot \nabla\left(\frac{1}{T_{\text{a}}}\right) dV > 0 \qquad (18)$$

When applying (18) we assume the shorezone system is isothermal and hence the second term on the right is vanishingly small. We support this assumption by noting that the body of empirical data from the field has never shown warmer water under breaking waves than found elsewhere in the shorezone, nor have episodes of high waves been correlated with episodes of elevated surfzone temperatures. If the shorezone is isothermal, then no entropy production is possible from the heat conduction mechanism and the second law by (18) reduces to,

$$\left.\frac{\partial S}{\partial t}\right)_{\text{UNIVERSE}} = \int \frac{\Phi}{T_a}\, dV > 0 \tag{19}$$

Under these circumstances the first law of thermodynamics (16) requires the rate of entropy production by viscous dissipation inside the system to be in balance with the rate at which entropy is discharged to the surroundings by latent heat transport,

$$\int \frac{\Phi}{T_a}\, dV = \int \frac{1}{T_a} \nabla \cdot q dV \tag{20}$$

This balance maintains constant entropy inside the system,

$$\left.\frac{\partial S}{\partial t}\right)_{\text{SYSTEM}} = 0 \tag{21}$$

The particular value at which the shorezone entropy remains constant is determined by the number of grains of sand contained within that system :

$$S = \frac{6 K_B N_o V_s}{\pi D^3} \left\{ \log\left[X_c (Z_1 + \hat{h}_c) \right] + \log J \right\}$$

where K_B is Boltzman's constant and the system boundary scale factor is

$$J = \oint \frac{d\zeta}{X_c}$$

If the entropy flux balance between system and surroundings in (20) were not upheld, then equilibrium states would not be possible in the shorezone because the system could not maintain constant state function as in (21). Without latent heat transport from the system, heat evolved from wave breaking would increase the local water temperature in time Δt by as much as:

$$\Delta T_a = \frac{g^{3/2} H_b^{1/2} \gamma^{3/2} \tan\beta_o \Delta t}{4\kappa_H c_\nu}$$

where H_b is breaker height, γ is a factor relating the depth of wave breaking h_b to breaker height $H_b = \gamma h_b$, $\tan\beta_o$ is mean beach slope, and $\kappa_H = 4{,}186$ J/kcal is the mechanical equivalent of heat. For a breaking wave of height $H_b = 1$ m with $\gamma \sim 4/5$ and a nominal beach slope of $\tan\beta_o = 0.025$, the temperature of the nearshore waters would increase continuously by about 3°C every 24 hours. This insensible result obtained by violating (20) re-enforces the isothermal shorezone assumption and suggests that equilibrium is a common and persistent state in the shorezone.

A system that achieves equilibrium in this manner through the dissipation of external work into the heat of a reservoir in the surroundings belongs to the general thermodynamic system known as *external mechanical irreversibility*, [*Zemansky and Van Ness*, 1966]. While (19) and (21) are conditions for equilibrium and (20) defines the type of equilibrium, these are not sufficient conditions to define a unique equilibrium state for the shorezone system. To obtain unique solutions, we adopt the criteria of maximum entropy production (MEP) that has been successfully applied to certain steady state equilibrium climate states by *Dewar* [2003], and *Ozawa et al.* [2003]. The MEP criteria is a particular form of the second law (15), that requires the entropy of the universe not only increases when the system proceeds from one equilibrium state to the next, but that the entropy increase is a stationary maximum. The validity of the MEP criteria is based on observational and numerical evidence showing that in general, non-linear systems

having many degrees of freedom for dynamic equilibrium tend to those states, among all possible states under the second law, that maximize entropy production.

When the MEP criteria is applied to (19) subject to (21), we take the state variable associated with the external work done by incident waves as the independent variable and then seek a stationary maximum for the viscous dissipation, which becomes the dependent state variable. Since the shorezone system volume and sediment volume have been fixed, the fluid/sediment interface (bottom profile) is the only remaining thermodynamic coordinate that is unrestrained and available to maximize dissipation. From *Batchelor* [1970], the average rate of dissipation of mechanical energy per unit volume in a 2-dimemsional, incompressible fluid system is $\Phi = 2\mu\langle\tilde{\omega}\cdot\tilde{\omega}\rangle = \langle\tilde{\tau}\cdot\tilde{\omega}\rangle$, where $\langle\ \rangle$ denotes time averaging; $\tilde{\omega}$ is the fluid vorticity generated by the action of viscosity μ and $\tilde{\tau}$ is the time varying wave induced shear stress, including bottom shear stresses, internal shear stresses and granular friction at the fluid sediment interface [*Bagnold*, 1956; *Inman and Bagnold*, 1963]. We assume that no vorticity or dissipation (due to bottom ventilation) occurs within that portion of the system occupied by the sediment mass. Let $dV' = \Delta y dA'$ represent a volume increment of the remaining portion of the system that contains the fluid vorticity, where dA' is an increment of area bounded by the closed contour ζ around the fluid portion of the system and Δy is a unit length of shoreline. Applying these assumptions and definitions to Stokes theorem, $\int\tilde{\omega}\cdot n_r dA' = \oint\tilde{u}\cdot d\zeta$, the average dissipation rate of the system becomes:

$$\int \Phi dV = \int \Phi dV' = \Delta y \int \langle\tilde{\tau}\cdot\tilde{\omega}\rangle\, dA' = \Delta y \oint \langle\tilde{\tau}\cdot\tilde{u}\rangle\, d\zeta \qquad (22)$$

When (22) is used to maximize entropy production only the segment of contour integration taken along the bottom profile produces a change in the state variables of heat and work, as all remaining segments are comprised of fixed system boundaries. In the shorezone system, the bottom profile defines the pathway along which heat and work are evolved and both state variables are path dependent in an irreversible process. Hence, the MEP formulation of the second law reduces to maximization of a simple line integral:

$$\left.\frac{\partial S}{\partial t}\right)_{UNIVERSE} = \frac{\Delta y}{T_a}\int \langle \tilde{\tau}\cdot\tilde{u}\rangle \, d\zeta > 0 \qquad \text{(maximum)} \tag{23}$$

Our equilibrium problem now becomes that of finding the profile curve $\zeta = \zeta(h,x,x')$ after (13) that makes the integral in (23) a stationary maximum. This can be accomplished with calculus of variations using a change of variables in the integrand of (23) in terms of a generalized functional $F(h,x,x')$ written

$$F(h,x,x') = \langle \tilde{\tau}\cdot\tilde{u}\rangle \frac{d\zeta}{dh} \tag{24}$$

with the functional in (24) the entropy integral in (23) is maximized by solving the Euler-Lagrange equation [*Boas*, 1966],

$$\frac{\mathrm{d}}{\mathrm{d}h}\frac{\partial F}{\partial x'} - \frac{\partial F}{\partial x} = 0 \tag{25}$$

General solutions to (25) are given in section 2.5.1 for the shorerise and bar-berm profiles, while particular solutions are found in section 2.5.2.

2.5.1 General Solutions

We will pose separate formulations for the viscous dissipation in the shorerise (shoaling zone) and bar-berm (surf zone) portions of the shorezone system (Figure 31a). When applied to (25), these separate formulations will yield general solutions for the shorerise profile ζ_2 and bar-berm profile ζ_1 that happen to belong to the same class of equation. The solutions for the shorerise and bar-berm are conjoined at the wave break point.

The simplest surrogate for the shorerise is one that is uniform in the alongshore direction in the region between closure depth and the wave breakpoint. The fluid dynamics in this region are approximated by the linear shoaling transformation of the shallow water Airy wave,

$$\begin{aligned} \tilde{u} &= u_{\mathrm{m}} \cos(\sigma t - kx) \\ u_{\mathrm{m}} &= \frac{H(x)}{2}\sqrt{\frac{g}{h(x)}} \\ H(x) &= \frac{H_{\infty}}{\sqrt{2\sigma}}\left(\frac{g}{h(x)}\right)^{1/4} \\ k &= \frac{\sigma}{\sqrt{gh(x)}} \end{aligned} \tag{26}$$

Here, $k = 2\pi$ /wavelength is local wave number, $\sigma = 2\pi/\text{period}$ is radian frequency, $u_{\mathrm{m}}(x)$ is velocity amplitude at the sea floor boundary layer, and $H_{\square}$ is incident wave height. Local wave height and depth, $H(x)$ and $h(x)$, are taken with respect to local curvilinear coordinate of the bottom profile ζ_2, as shown in Figure 1b. The

Airy approximation in (26) has been shown in *Mei* [1989] to be valid over sloping bottoms if the following mild slope condition is satisfied:

$$\frac{\tan\beta}{kh} << 1 \tag{27}$$

where $\tan\beta = dh/dx$ is the local bottom slope. Exactly how much smaller than unity (27) must be is not definite, but its largest value is at the breakpoint where $kh = \sigma(H_b/\gamma g)^{1/2}$. We assume there is some $N >> 1$ such that (27) is satisfied everywhere in the shorerise by requiring

$$dh \sim \varepsilon\, dx \sim O(L)$$

$$\varepsilon = \frac{\sigma}{N}\left(\frac{H_b}{\gamma g}\right)^{1/2} \cong \frac{\sigma^{4/5}}{2^{1/5}N}\left(\frac{H_\infty}{g\gamma}\right)^{2/5} \tag{28}$$

where L is a characteristic length scale, ε. is a stretching factor proportional to the Airy wave mild slope factor N.

A simple power law formulation is used to prescribe the bottom shear stress,

$$\tilde{\tau} = \tau_o \cos(\sigma t - kx + \varphi)$$

$$\tau_o = \rho c_f u_m^2 = \rho K_\tau u_m^n \tag{29}$$

where τ_o is the shear stress amplitude; φ is the phase angle between the bottom shear stress and the oscillatory potential flow velocity from Airy theory; c_f is the quadratic drag coefficient and n is the shear stress velocity exponent referred to as *shear stress linearity*. The particular value of n varies with the dependence of c_f on

parameters of dynamic similitude, e.g., oscillatory Reynolds number $(R_e = u_m^2 / \sigma\nu)$, grain Reynolds number $(R_{eg} = u_m D / \nu)$, Keulegan-Carpenter (inverse Strouhal) number $(S_t = u_m / \sigma\eta_s)$, where η_s is bottom roughness, [e.g., *G. I. Taylor*, 1946; *Keulegan and Carpenter*, 1958; *Sleath*, 1984]. If we generalize $c_f \sim (R_e^{\,j} R_{eg}^{\,l} S_t^{w})$, then $n = 2 + 2j + l + w$ and the shear stress amplitude can be written in terms of a proportionality factor K_τ that is independent of u_m and consists of a collection of other factors contained in R_e, R_{eg} and S_t that make (27) dimensionally correct.

From (26) and (27), the dissipation rate per unit length of profile varies with depth h as

$$\left\langle \tilde{\tau} \cdot \tilde{u} \right\rangle = \rho K_\tau \cos\varphi \; u_m^{n+1} = \frac{\varpi}{h^{3(n+1)/4}}$$

$$\varpi = \frac{\rho K_\tau \cos\varphi \; H_\infty^{n+1} g^{3(n+1)/4}}{8\sigma^{(n+1)/2}} \tag{30}$$

where the work factor ϖ is independent of h, x and x'. When we select from (13) an infinitesimal arc length of the shorerise profile having the form,

$$d\zeta_2 = \sqrt{1 + x'^2}\, dh$$

then the integral in (23) for which we seek a stationary maximum becomes:

$$\int \left\langle \tilde{\tau} \cdot \tilde{u} \right\rangle d\zeta_2 = \varpi \int h^{-3(n+1)/4} \sqrt{1 + x'^2}\; dh \tag{31}$$

In terms of non-dimensional variables denoted by an underscore, $\underline{x} = x/L\,; \underline{h} = h/L,$ the following functional F is collected from the order-1 terms in (30) for use in the Euler-Lagrange equation in (25)

$$F(\underline{h}, \underline{x}, \underline{x}') = \underline{h}^{-3(n+1)/4}\sqrt{1+(\varepsilon \underline{x}')^2} \tag{32}$$

Because $\partial F/\partial \underline{x} = 0,$ the first integration of (25) using (32) gives,

$$\varepsilon \underline{x} = \int \sqrt{\frac{\underline{\Omega}\,\underline{h}^{\alpha}}{1-\underline{\Omega}\,\underline{h}^{\alpha}}}\, d\underline{h} \tag{33}$$

where $\alpha = 3(n+1)/2$ and $\underline{\Omega}$ is the first integration constant. We can rationalize the integrand of (21) using two separate Euler substitutions after *Gradshteyn and Ryzhik*, [1980, §2.261, §2.264]. These provide a general solution with two roots that has the following dimensional form,

$$x = \frac{\Omega^{(\alpha-1)/\alpha}}{\varepsilon\sqrt{R}}\left[-\sqrt{\frac{h^{\alpha}}{\Omega}-h^{2\alpha}} + \frac{1}{2\Omega}\arccos\left(1-2\Omega h^{\alpha}\right)\right] \tag{34}$$

where $\Omega = \underline{\Omega}/L^{\alpha}$ and the second integration constant of (25) is -π/4Ω. The first root is given by,

$$R = R_{\mathrm{a}} = \left(\frac{\pi}{2I_{\mathrm{e}}^{(2)}}\right)^2\left[4\Omega h^{\alpha} - 4\Omega^2 h^{2\alpha} + \frac{2}{1+\alpha}\left(1-4\Omega h^{\alpha}+4\Omega^2 h^{2\alpha}\right)\right] \tag{34a}$$

and the second root by,

$$R = R_{\mathrm{b}} = \left(\frac{\pi}{2I_{\mathrm{e}}^{(1)}}\right)^2 \left[1 - 4\Omega h^{\alpha} + 4\Omega^2 h^{2\alpha} + \frac{2}{1+\alpha}\left(4\Omega h^{\alpha} - 4\Omega^2 h^{2\alpha}\right)\right] \tag{34b}$$

Here $I_{\mathrm{e}}^{(1)}, I_{\mathrm{e}}^{(2)}$ are elliptic integrals of the first and second kind, respectively.

The general solution given by (34) belongs to a class of equations known as elliptic cycloids [*Boas*, 1966]. We can show that by making a transformation into polar coordinates (r,θ) with a substitution of variables:

$$\theta = \arccos\left(1 - 2\Omega h^{\alpha}\right) \tag{35}$$

from which we get

$$\frac{h^{\alpha}}{\Omega} - h^{2\alpha} = \frac{1}{4\Omega^2}\sin^2\theta \tag{36}$$

With (35) and (36), equation (34) reduces to two types of elliptic cycloids having the general polar coordinate form:

$$x = x_2 = \frac{2r\, I_{\mathrm{e}}^{(k_{1,2})}}{\pi\,\varepsilon}\left(\theta - \sin\theta\right) \tag{37}$$

where *r* is the radius vector measured from the center of an ellipse whose semi-major and semi-minor axes are *a*, *b* and $I_{\mathrm{e}}^{(k)}$ is the elliptic integral of the first or second kind ($k_{1,2}$) depending on which of the two cycloid types we resolve from (34a) and (34b). We limit our discussions to the solutions for the type-a cycloids that result from the first root in (34a) because these were shown to be in good agreement with field data. The polar equivalent of the type-a cycloid from (37) has a radius vector whose magnitude is

$$r = r_a = \left[\frac{a^2 b^2}{a^2 \sin^2\theta + b^2 \cos^2\theta} \right]^{1/2} = \frac{a\sqrt{1-e^2}}{\sqrt{\sin^2\theta + (1-e^2)\cos^2\theta}} \tag{38}$$

where e is the eccentricity of the ellipse given by $e = \sqrt{1-(b^2/a^2)}$. The polar form of the type-a cycloid in (34a) is based on the elliptic integral of the second kind that has an analytic approximation, $I_e^{(2)} = (\pi/2)\sqrt{(2-e^2)/2}$, see *Hodgman* [1947]. The integration constant Ω in (37) is determined from the dimensions of the ellipse axes by noting when $\theta = \arccos(1 - 2\Omega h^\alpha) = \pi$, then $\Omega h^\alpha = 1$. This gives:

$$\Omega = (2a)^{-\alpha} \qquad \text{(type-a cycloid)} \tag{39}$$

It is apparent that the root R in (34a) is equivalent to $rI_e^{(k)}/b$ in (37) when

$$1 - e^2 = \frac{2}{(1+\alpha)}$$

Hence, the eccentricity of the elliptic cycloid is governed by the shear stress linearity, n

$$e = \left[\frac{\alpha - 1}{\alpha + 1} \right]^{1/2} = \left[1 - \frac{4}{(3n+5)} \right]^{1/2} \tag{40}$$

The inverse of (16) subject to (19) gives the companion polar equation for the elliptic cycloid,

$$h = \frac{\pi\varepsilon\, x_2}{2I_e^{(k_{1,2})}} \left(\frac{1-\cos\theta}{\theta - \sin\theta} \right) = r(1-\cos\theta) \tag{41}$$

A geometric representation of the type-a elliptic cycloid used in the general solution for the shorerise profile is shown in Figure 31b as traced by an ellipse having eccentricity $e = 0.75$ and $\varepsilon = 1$. The equilibrium beach profile is given by the trajectory of a point on the semi-major axes of an ellipse that rolls seaward in the cross-shore direction under the plane of $h = h_2 = 0$. This trajectory defines the elliptic cycloid and the segment traced by the first half of a rotation cycle ($0 < \theta < \pi$) of the rolling ellipse is the equilibrium beach profile. The depth of water at the seaward end of the profile ($\theta = \pi$) is $h = 2a$ in the case of the type-a cycloid. The length of the profile X is equal to the semi-circumference of the ellipse,

$$X = \frac{2aI_e^{(2)}}{\varepsilon} \cong \frac{\pi\, a}{\varepsilon}\sqrt{\frac{2-e^2}{2}} \qquad \text{at} \quad \theta = \pi \quad \text{(type-a cycloid)} \qquad (42)$$

2.5.2. Particular Solutions

In this section we apply boundary and matching conditions to the general solutions developed in the previous section to obtain particular solutions for the shorerise and bar-berm profiles that conjoin at the breakpoint, X_3 (Figure 31a). The general solutions developed in the previous section admit to an arbitrary number of equilibrium profiles depending on the type of elliptic cycloid and its eccentricity. Here we use field measurements to resolve the eccentricity and select the best-fit cycloid that conforms to natural beaches. A Taylor series expansion of (37) about $x = 0$ gives a simple analytic approximation to the general elliptic cycloid solution that is equivalent to the equilibrium profile formulations developed earlier by *Dean* [1977, 1991] and *Inman et al.* [1993]. The leading order terms of this Taylor series expansion are,

$$h = Ax^m + 0\left(\varepsilon^{1/1+\alpha}\right) \qquad (43)$$

where terms $0\left(\varepsilon^{1/1+\alpha}\right)$ are neglected and

$$m = \frac{2}{(2+\alpha)} = \frac{2(1-e^2)}{(3-e^2)}$$

For the type-a cycloid, the profile factor A in (43) becomes:

$$A = \left[\frac{3\pi\varepsilon\ (2a)^{\alpha/2}}{4I_e^{(2)}}\right]^{2/2+\alpha} \tag{44}$$

Both the profile factor A, and the curvature exponent m of the classical parametric representation in (43, 34) are functions of the eccentricity of the elliptic cycloid. However, only the profile factor A varies with cycloid size. We use these dependencies in combination with the extensive data base on (A, m) derived from best-fits to beach profile measurements [*Inman et al.*, 1993] to establish a criteria for the selections for a and e, that give particular solutions.

Beginning with the shorerise profile, the origin of the cycloid in Figure 24a is positioned at mean sea level where $\theta = 0$ and $h = h_2 = 0$ at $x = x_2 = 0$. It is apparent that the elliptic cycloid must converge on closure depth h_c within one-half revolution of the cycloid wheel, $h = h_2 \to h_c \text{ as } \theta \to \pi$. Hence, the size of the shorerise ellipse axes are given by:

$$a = a_2 = h_c / 2 \tag{45}$$

This means that the closure depth formulation is decisive in achieving a particular solution to the shorerise equilibrium profile. However, the quantification of *closure depth* appears to be somewhat vague in the literature.

The general notion of closure depth h_c is the maximum depth at which seasonal changes in beach profiles are measurable by field surveys, most commonly using fathometers [*Inman and Bagnold*, 1963]. Closure depth for seasonal profiles repeated over a period of a year or more is usually taken as the depth of closure of the envelope of profile changes, e.g., where the depth change vs depth decreased to a common background error [e.g., *Kraus and Harikai*, 1983; *Inman et al.*, 1993]. When observations are limited to comparison of two or three surveys, the closure depth becomes the depth at which the survey lines converge with depth, a point of some uncertainty [e.g., *Shepard and Inman*, 1951; *Nordstrom and Inman*, 1973; *Birkemeier*, 1985]. *Hallermeier* [1978, 1981] derived a relation for closure depth, by assuming a relationship for the energetics of sediment suspensions based on a critical value of the Froude number, giving:

$$h_c \cong 2.28H_{ss} - 6.85\left(H_{ss}^2 / gT^2\right)$$

where H_{ss} is the nearshore storm wave height that is exceeded only 12 hours each year and T is the associated wave period.

Birkemeier [1985] suggested different values of the constants and found that the simple relation $h_c = 1.57\, H_{ss}$ provided a reasonable fit to his profile measurements at Duck, North Carolina. *Cowell et al*. [1999] reviews the Hallermeier relation for closure depth h_c and limiting transport depth h_i and extends the previous data worldwide to include Australia. Their calculations indicate that h_c ranges from 5 m (Point Mugu California) to 12 m (SE Australia), while h_i ranges

from 13 m (Netherlands) to 53 m (La Jolla, California). They conclude that discrepancies in data and calculation procedures make it "pointless to quibble over accuracy of prediction" in h_c and h_i. In the context of planning for beach nourishment, *Dean* [2002] observes that "although closure depth…..is more of a concept than a reality, it does provide an essential basis for calculating equilibrated…beach widths."

While it may be reasonable to apply the Hallermeier relation or its simpler form after *Birkemeier* [1985] to the shorerise boundary condition, comparisons with the *Inman et al.* [1993] beach profile data set show that these relations tend to underestimate closure depth. We propose an alternative closure depth relation. This relation is based on two premises: 1) closure depth is the seaward limit of non-zero net transport in the cross-shore direction; and, 2) closure depth is a vortex ripple regime in which no net granular exchange occurs from ripple to ripple. *Inman* [1957] gives observations of stationary vortex ripples in the field and *Dingler and Inman* [1976] establish a parametric relationship between dimensions of stationary vortex ripples and the Shield's parameter $\tilde{\Theta}$ in the range $3 < \tilde{\Theta} < 40.$ Using the inverse of that parametric relation to solve for the depth gives:

$$h_c = \frac{K_e H_\infty}{\sinh k h_c}\left(\frac{D_o}{D_2}\right)^{\psi} \tag{46}$$

where K_e and ψ are non-dimensional empirical parameters, D_2 is the shorerise median grain size; and D_o is a reference grain size. With $K_e \sim 2.0, \psi \sim 0.33$ and $D_o \sim 100\mu\text{m}$, the empirical closure depths reported in *Inman et al.* [1993] are reproduced by (46). From (46) we find closure depth increases with increasing wave height and decreasing grain size, as shown in Figure 32. Because of the wave

number dependence, closure depth also increases with increasing wave period. Using (46), the distance to closure depth X_{c2} can be obtained from (42),

$$X_{c2} = \frac{h_c I_e^{(2)}}{\varepsilon} \cong \frac{\pi\, h_c}{2\varepsilon}\sqrt{\frac{2-e^2}{2}}$$

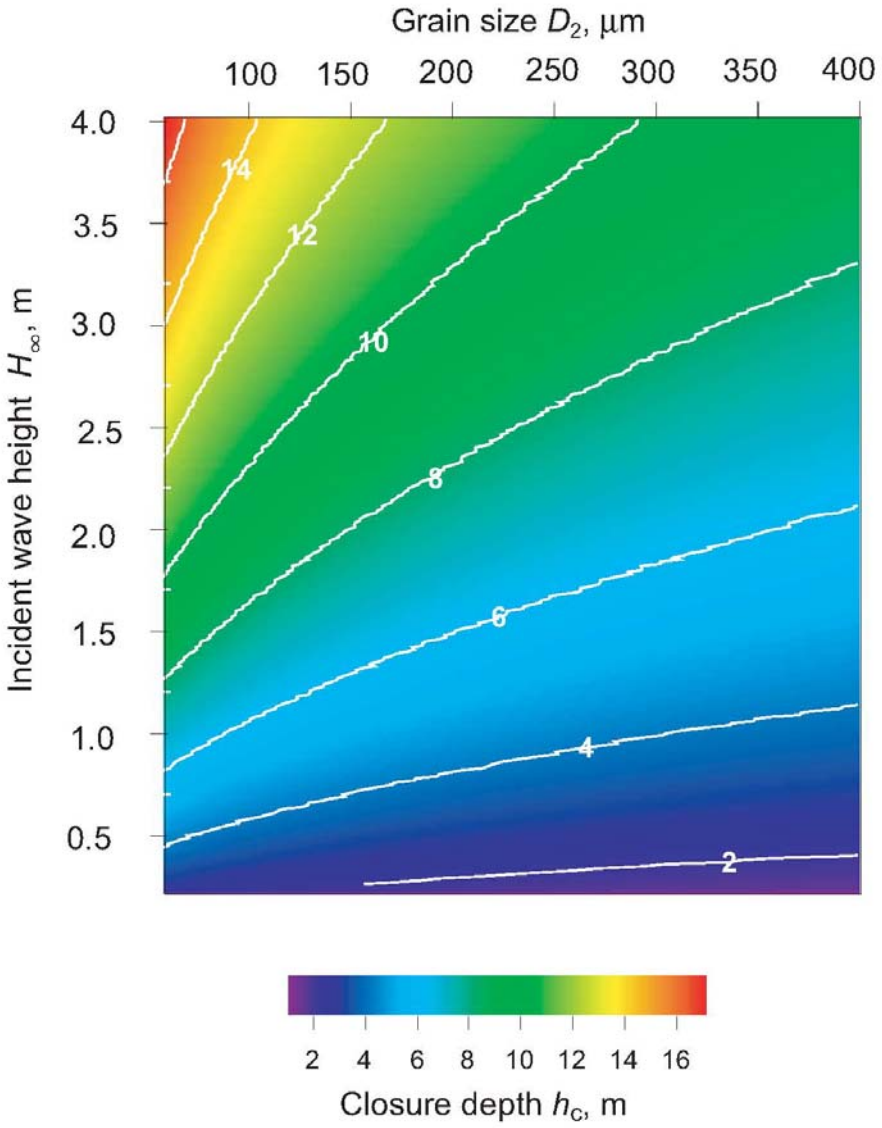

Figure 32. Closure depth h_C dependence on grain size D_2 and incident wave height H_∞ for waves of 15 sec period. (ψ = 0.33, K_e = 2.0, and D_0 = 100 µm)

where X_{c2} is measured from the origin of the shorerise located a distance X_2 from the berm and a distance $X_3 - X_2$ inside the breakpoint (Figure 31a). This will be determined subsequently from the matching condition. It is apparent from (46) and (42) that the shorerise profile dimensions grow with increasing wave height and period, and with decreasing grain size. From (43) and (40) the relation between shorerise profile exponent m_2 and shear stress linearity n is:

$$m_2 = \frac{4}{7+3n} \qquad \text{or,} \qquad n = \frac{4}{3m_2} - \frac{7}{3} \tag{47}$$

To select a preferred set of cycloid solutions for the shorerise, we examine the relation between (47) and the best-fit profiles to measured shorerises. *Inman et al.* [1993] gives tabulations of the shorerise profile exponent m_2 derived from best fits to 51 measured profiles from nine beaches comprising the basic data set. Of these 51 measured profiles, 20 were reported to represent summer equilibrium profiles, 20 represented winter equilibrium, while 11 were said to be non-equilibrium "translational" profiles. Only two of the 11 non-equilibrium profiles reported for the basic data set in Table 1 of *Inman et al.* [1993] produced best fits with $m_2 > 0.571$ (outside the theoretical limit for shorerise equilibrium); while all 40 of the equilibrium profiles resulted in best fit $m_2 < 0.571$ (Figure 33). The mean shorerise profile exponent for the entire ensemble of 51 profiles (equilibrium and non-equilibrium alike) was $\overline{m}_2 = 0.362$, which corresponds to a shear stress linearity of n = 1.35 and a cycloid eccentricity of e = 0.747. The mean m_2 of the 40

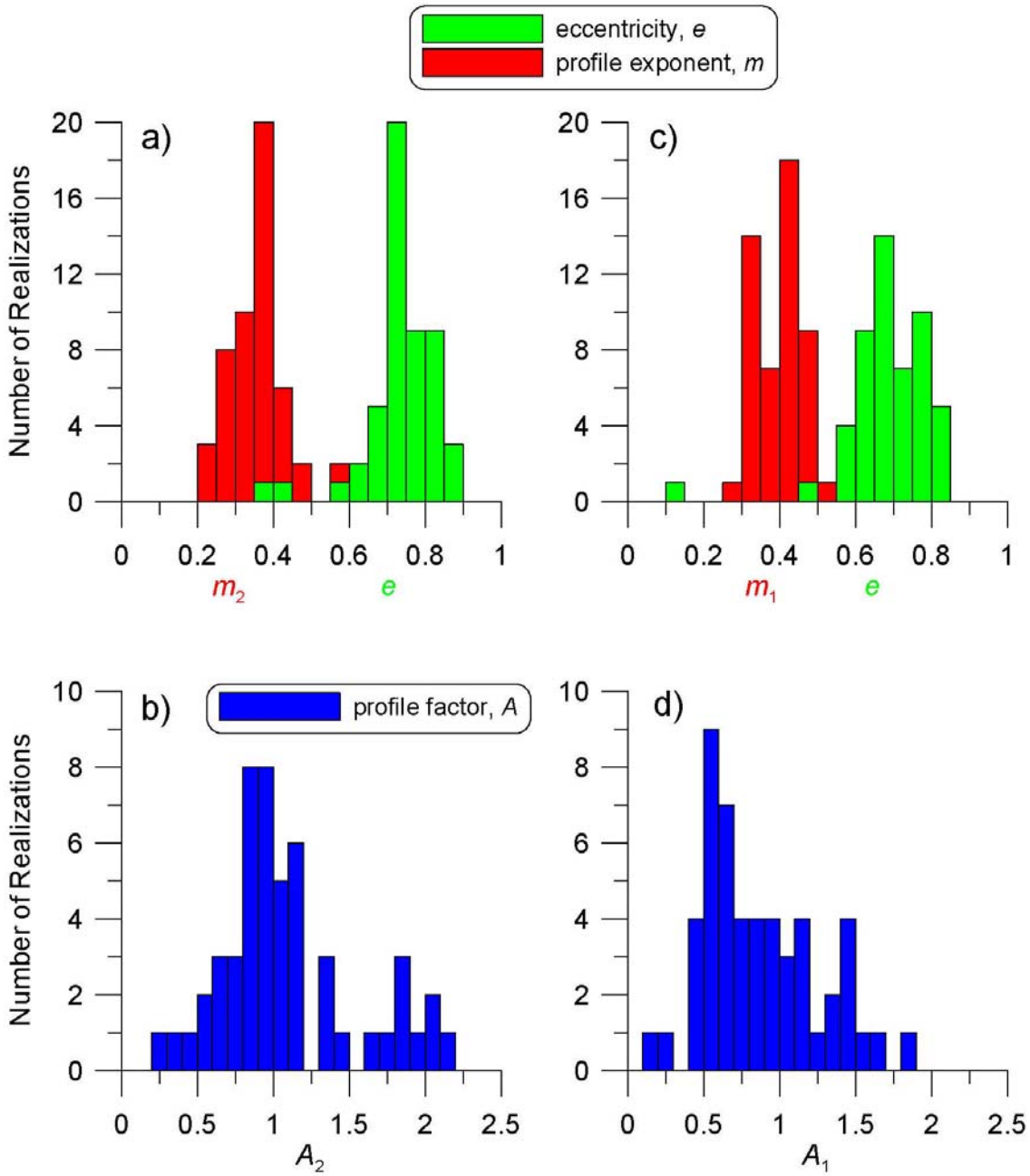

Figure 33. Histograms of profile exponent *m* (red) and profile factor *A* (blue) from best fit to beach surveys [after Inman, et al., 1993], corresponding eccentricity of elliptic cycloid (green).

equilibrium profiles is $\overline{m}_2 = 0.365$, giving n = 1.32 and e = 0.744. Based on these averages, (47) suggests that the bottom shear stress amplitude over the shorerise typically varies as $\tau_o \sim u_m^{4/3}$ in (29), coincident with the formulation of *Kajiura* [1968] for bottom friction due to oscillatory flow over rough beds when $S_t = u_m / \sigma \eta_s < 30.$ This scale regime is consistent with the vortex ripple regime reported by *Dingler and Inman* [1976] when the roughness height η_s is taken to be equivalent to the ripple height. The range of variation in the shorerise exponent for the remaining 49 profiles was $0.21 \le m_2 \le 0.5$ (Figure 33). At the upper limit of this range, as $m_2 \to 0.5$, the bottom shear stress varies weakly as $\tau_o \sim u_m^{1/3}$ and the shorerise cycloid has an eccentricity of e = 0.577. As $m_2 \to 0.4$, the bottom shear stress becomes linear (n = 1), and the resulting cycloid solution for the shorerise has an eccentricity of e = 0.707. Linear bottom shear stress $\tau_o \sim u_m$ would be expected with a laminar Stokes oscillatory boundary layer common to small amplitude oscillations over a perfectly smooth, impermeable bed, for which $c_f \sim R_e^{-1/2}$; [*Stokes*, 1851; *Lamb*, 1932; *Batchelor*, 1970; *Sleath*, 1984].

Intermediate in the upper portion of the range of variability, where $\overline{m}_2 \le m_2 \le 0.4,$ the periodic bottom shear stress can be characterized by a shear stress relation for smooth granular beds after *G. I. Taylor* [1946] that uses a drag coefficient formulation, $c_f \sim R_{eg}^{-1/5} S_t^{-3/5}$, and gives a shear stress linearity of n = 6/5, corresponding to $m_2 = 0.377$ with a cycloid eccentricity e = 0.731. In the lower potion of the range of variability below the mean, say $m_2 \to 0.25$, the shear stress becomes cubic $\tau_o \sim u_m^3$, giving a cycloid eccentricity of e = 0.845. At the lower limit $m_2 \to 0.21,$ the non-linearity of the shear stress increases to n = 4 and the cycloid eccentricity becomes e = 0.875. Generally, over the lower portion of the range of variability, $0.21 \le m_2 \le \overline{m}_2$, the shear stress takes on a relatively high degrees

of non-linearity, typical of form drag over non-stationary rippled beds at high Reynolds numbers $R_e \geq 10^4$, [*Sleath*, 1982, 1984], or ventilated oscillatory boundary layers over porous beds, [*Conley and Inman*, 1994].

From the above consideration of the empirical evidence, we conclude that the shorerise equilibrium profile is a set of elliptic cycloids whose eccentricity is limited to the range $0.447 \leq e \leq 0.875$, (Figure 31c) depending on bed roughness and dynamic scale regime, with semi-major and semi-minor axes specified by (45) and (46). The most common outcome has an eccentricity $\bar{e} = 0.744$, that can be represented by an analytic approximation given by (43) with $m = \overline{m}_2 = 0.365$ and $A = \overline{A}_2$ calculated from (44) using $\alpha = 3.479$.

Proceeding with the family of particular solutions for the bar-berm, we note that the Euler-Lagrange equation in (25) is an inhomogeneous linear differential equation, and as such, we may add a constant to any of our solutions and the resultant will also be a solution. This we must do in the bar-berm because the origin in Figure 31a is elevated above mean sea level at $h_1 = Z_1$. Accordingly, the bar-berm cycloids have the following vertically offset polar form:

$$h = h_1 = \frac{\pi\varepsilon\, x_1}{2I_e^{(k)}}\left(\frac{1-\cos\theta}{\theta-\sin\theta}\right) + Z_1 = r\left(1-\cos\theta\right) + Z_1 \qquad (48)$$

where *r* is given by (20). We prescribe the vertical offset by the maximum runup elevation from Hunt's Formula [*Hunt*, 1959; *Guza and Thornton*, 1985; *Raubenheimer and Guza*, 1996],

$$Z_1 = -\Gamma H_b$$

where Γ is the runup factor taken herein as $\Gamma = 0.76.$ The bar-berm cycloid must converge on the breaker depth $h_b = H_b / \gamma$ within one-half revolution of the cycloid wheel,

$$h = h_1 \to h_b \quad \text{as} \quad \theta \to \pi$$

Because of the vertical offset to the bar-berm profile origin, the ellipse axes must span the distance between Z_1 and h_b as $\theta \to \pi.$ Consequently, the breakpoint boundary condition in (40) leads to the following sizing of the bar-berm ellipse axes,

$$a = a_1 = \frac{H_\infty}{2\Lambda}\left(\frac{1}{\gamma} + \Gamma\right) \tag{49}$$

where Λ is the shoaling factor from linear theory. The field work of *Raubenheimer et al.* [1996] shows that γ has an observed range of variability $0.2 < \gamma < 1.6.$ Enforcing the breakpoint boundary condition in gives the distance to the break point X_3 from (42),

$$X_3 = \frac{(h_b - Z_1) I_e^{(2)}}{\varepsilon} \cong \frac{\pi\ H_\infty}{2\Lambda\varepsilon}\left(\frac{1}{\gamma} + \Gamma\right)\sqrt{\frac{2 - e^2}{2}} \tag{50}$$

The data in *Inman et al.* [1993] indicates that the envelope of particular solutions for the bar-berm are limited to a set of type-a and type-b cycloids of the form in (48). Within this envelope of solutions, the most commonly occurring is the linear bore (e = 0.707) that can be approximated by (43) with $m = \overline{m}_1 = 0.400$ and $A = \overline{A}_1$ calculated from (44) using $\alpha = 3.0.$ The mean value of m_1 for the 51 best fits to the bar-berm profiles reported in the data set of *Inman et al.* [1993] is

$\overline{m}_1 = 0.411$, of which only one (a translational profile) gave $m_1 \to 0.66,$ the equivalent of the brachistochrone solution. The mean m_1 of the 40 equilibrium profiles was $\overline{m}_1 = 0.400,$ which corresponds to a cycloid with eccentricity $e = 0.707$, coincident with a linear bore (Figure 33). The range of variability for the 40 equilibrium profiles was $0.29 \le m_1 \le 0.55,$ corresponding to cycloids with $0.491 \le e \le 0.813.$ The cycloid derived from the maximum wave dissipation formulation ($e = 0.845$) corresponds roughly to the lower limit $(m_1 \to 0.29)$ of this statistical spread. This limit can also be obtained from the depth-limited bore solution corresponding to a cycloid with eccentricity of $e = 0.813$, exactly. The magnitude and dynamic range of the A_1 solutions in (44) are consistent with the best-fit results to beach surveys from *Inman et al.* [1993] that show a mean of $\overline{A}_1 = 0.868$ with a standard deviation of 0.386. The bar-berm profile factor A_1 increases with increasing wave height and decreasing $\gamma.$ Unlike the shorerise, the ellipse axes a and b in (49) are independent of frequency in the bar-berm. Consequently A_1 decreases with increasing wave period due to the frequency dependence of the ε factor in (28). Therefore the mean bar-berm slopes become flatter with longer period waves.

The bar-berm A_1 solutions show very similar compound variation with wave height as the shorerise A_2 solution. A relation arises between γ and beach grain size through the matching condition discussed below. The basis for this relation is a finding in *Raubenheimer et al.* [1996] who show that γ increases with increasing bottom slope at the break point, $\tan \beta_{X_2}$,

$$\gamma = K_o + K_1 \frac{\tan \beta_{X_2}}{kh}$$

where K_o, K_1 are empirical constants taken as $K_o = 0.2$ and $K_1 = 6.0$. The bottom slope at the break point, $\tan\beta_{X_2}$, is given by the slope of the shorerise profile at $x_2 = X_3 - X_2$.

To complete the particular solutions, we must match the bar-berm and shorerise profiles at the break point (Figure 31a). The point of conjoinment is the seaward end of the bar-berm profile at the break point, a distance X_3 from the origin. Here, the shorerise and bar-berm solutions must both equal the breaker depth,

$$h_2 = h_1 = h_b = \frac{H_b}{\gamma} = \frac{H_\infty}{\Lambda\gamma}$$

at $x_2 = X_3 - X_2$ and $x_1 = X_3$, respectively. To obtain this match, the origin of the shorerise profile must be located a distance $X_3 - X_2$ landward of $x_1 = X_3$. In terms of the polar form of the shorerise cycloid, this distance is,

$$\begin{aligned} X_3 - X_2 &= \frac{2r_2 I_e^{(k)}}{\pi\varepsilon}(\theta_b - \sin\theta_b) \\ \theta_b &= \arccos\left[1 - 2\left(\frac{H_\infty}{\Lambda\gamma h_c}\right)^\alpha\right] \end{aligned} \tag{51}$$

where r_2 is given by (38) and evaluated at $\theta = \theta_b$, and α is related to shorerise cycloid eccentricity by (40). Taking the above, the shorerise bottom slope at the breakpoint can be solved,

$$\tan\beta_{X_2} = \frac{\sin\theta_b + e^2(\cos\theta_b - 1)\sin\theta_b\cos\theta_b}{1 - \cos\theta_b + e^2(\sin\theta_b - \theta_b)\sin\theta_b\cos\theta_b} \tag{52}$$

Because θ_b is grain size dependent through the closure depth relation in (46), γ in (51) also becomes grain size dependent. This in turn makes the bar-berm profile sensitive to grain size variability. In terms of the analytic approximation, the matching condition is satisfied by,

$$X_2 = X_3 - \left[\frac{A_1 X_3^{m_1} - \Gamma H_\infty / \Lambda}{A_2} \right]^{1/m_2} \tag{53}$$

giving the bottom slope at the break point as,

$$\tan \beta_{X_2} = m_2 A_2 (X_3 - X_2)^{m_2 - 1} \tag{54}$$

where X_3 is given by (50). For further details see Jenkins and Inman (in press).

2.6 Codes for the Equilibrium Profile Algorithms

The Littoral Cell Model (LCM) codes that perform the type-a cycloid and closure depth computations of the equilibrium sediment cover profile are **cycloid_ellipse_2.for** in Appendix-I and **cycloid_ellipse_3.for** in Appendix-J. The **cycloid_ellipse_2.for** code does all computations for the type-a cycloid solutions, while **cycloid_ellipse_3.for** computes type-b cycloids. We will confine our attention here to the type-a cycloid solutions as these were found to give the best predictive skill in calibration trials described in Section 2.5.4. The input parameters output files which are required by **cycloid_ellipse_2.for** are :

sp2loid_per15.txt…… *ofile

sp2loid_nrange-per50.txt…… *ofile0

plymwht1_0med_sr_a50.txt…… *ofile1 1 meter wave

plymwht2_0med_sr_p80.txt…… *ofile2 2 meter wave

plymwht3_0med_sr_a50.txt …… *ofile3 3 meter wave

plymwht4_0med_sr_a50.txt…… *ofile4 4 meter wave

plymcrit_0med_sr_a50.txt…… *ofile5 slope=crit each curve

plymendp_0med_sr_a50.txt …… *ofile6 endpoint of each curve

aaa_whtsmlmed_sr_a50.txt …… *ofile7 0.5 meter wave

aaa_wht150med_sr_a50.txt ……*ofile8 1.5 meter wave

aaa_wht050med_sr_a50.txt …… *ofile9 0.5 meter wave

aaa_wht1_0med_sr_a50.txt …… *ofile11 1 meter wave

aaa_wht150med_sr_a50.txt…… *ofile10 1.5 meter wave

aaa_wht2_0med_sr_a50.txt…… *ofile12 2 meter wave

aaa_wht3_0med_sr_a50.txt …… *ofile13 3 meter wave

aaa_wht4_0med_sr_a50.txt…… *ofile14 4 meter wave

15.0 …… *per wave period

9.8 …… *g MKS acceleration of gravity

0.0 …… *ak sea level anomaly

0.015 …… *beta shorerise slope at closure depth

0.34 …… *akm profile curvature

2.0 …… *akd Dougs coefficient, ke

5.5445 …… *vdepce empirical max breaker depth

0.345 …… *bs free parameter profile factor wave height exp

380 …… *irange survey reference number

1800 …… *nrange degrees x 0.1

0.85 …… *snum ellipse eccentricity

0.22 ……*akx verticle to horizontal stretch, N (smaller makes profile longer)
8.0 …… *hce empirical max closure depth
0.0067965 …… *crit empirical critical slpoe at closure depth
100.0 ……*refdia reference grain diameter
0.333 …… *a exponent on grain diameter ratio
100.0 …… *dia2 shorerise grain diameter
80 …… *iht1 1 m wave height for critical mass envelope
180 …… *iht2 2 m wave height for critical mass envelope
280 …… *iht3 3 m wave height for critical mass envelope
380 …… *iht4 4 m wave height for critical mass envelope
30 …… *iht05 0.5 m wave height for critical mass envelope
130 …… *iht15 1.5 m wave
2.58 …… *akbr breaker coefficient(set at vdepce+zone/Hb when ibrbm=1)
1 …… *ibrbm 0=shorerise, 1=barberm (run on 0 to get hc)
5.0 …… *zone survey elevation (set at zero when ibrbm = 0)
7.5 …… *xshift survey distance bench mark

In addition to the basic macro-scopic inputs (wave height, period, grain size) the input file to **cycloid_ellipse_2.for** includes a number of empirical inputs from field surveys to allow the solutions to be readily aligned with survey bench mark datum during the calibration process described in Section 2.7. The **cycloid_ellipse_2.for** program also generates a family of cycloids based on a distribution of wave heights to facilitate critical mass calculations in Section 2.8.

2.7 Calibrating the LCM Equilibrium Profile Algorithms

Here we detail the calibration of the **cycloid_ellipse_2.for** by making point-wise comparisons between particular shorerise and bar-berm solutions from thermodynamic theory and the profiles measured by the U. S. Army Corps of Engineers at their beach survey range PN1180, near Oceanside, CA during a six year period between March 1981 and September 1987 [*USACE*, 1985; 1991]. This range and setting are described in *Inman et al.* [1993]. Wave climate was measured in 6 hr intervals by the pressure sensor array located off Oceanside, CA [*CDIP*, 1980-1988]. These directional wave data were back refracted into deep water from their measurement location and forward refracted to 10 m depth in the neighborhood of the PN1180 beach range to correct for local shelf and island sheltering effects [*O'Reilly and Guza*, 1991, 1993]. Under the hypothesis that equilibrium is determined by the persistent large waves, the refracted wave time series were filtered for the highest 5% waves using the **cdip_histogram_percentile_soi.for** code and then time-averaged over each survey period to provided the forcing history of the H_∞, T, and Λ needed to calculate temporal variability of the boundary conditions on each profile. Grain size data from *Inman* [1953], *Inman and Rusnak* [1956] and *Inman and Masters* [1991] were used in these calculations. All remaining free parameters were set according to: $\Gamma = 0.76, N = 10, K_e = 2.0, \psi = 0.33, K_0 = 0.2, K_1 = 6.0$.

The horizontal location of the bar-berm origin relative to the survey benchmark X_1 (Figure 31a) was treated as an empirical input to **cycloid_ellipse_2.for,** taken directly from the data base of each survey. Although X_1 could have been calculated with divergence of drift techniques applied to the local sediment budget [e.g.

Inman and Dolan, 1989], it was decided not to obscure the accuracy of the thermodynamic solutions with potential errors in the calculation of X_1.

The solutions were calculated as exact cycloids by the following series of iterative steps: a) shorerise profiles were calculated from **cycloid_ellipse_2.for,** using an initial assumption of a cycloid eccentricity of $e = 0.745$, per the Kajiura [1968] shear stress formulation; b) bar-berm profiles were calculated from **cycloid_ellipse_2.for,** using initial assumptions that $\gamma = 0.8$ and $e = 0.707$, per the linear bore dissipation formulation; c) the initial profiles from steps-a & -b are matched by the X_3 - X_2 shift of the shorerise profile calculated from (51); d) the bottom slope at the breakpoint is calculated from (52) and used to correct the initial assumption of the gamma factor by means of (51); e) the bar-berm profile is re-calculated per step-b using the corrected gamma factor; f) step-a through step-e is repeated making iterative adjustments to the eccentricity to minimize the mean squared error between the cycloid solutions and the measured profile.

Figure 34 gives a point-by-point comparison between the type-a cycloid solutions and the six measured beach profiles surveyed at PN1180. Shorerise cycloids are shown as dashed blue lines; bar-berm profiles are shown as dashed red lines; and the measured profiles are solid gray lines. The legend of each grid cell gives the average significant wave height and period of the highest 5% waves that occurred between successive survey periods. The type-a cycloids and Figure 31c gave a predictive skill factor of **R** = 0.83 to 0.95, where **R** is adapted from *Gallagher et al.* [1998] and applied to the mean-square error in depth. The type-b cycloids produced a skill factor generally less than 0.5. The eccentricity of the

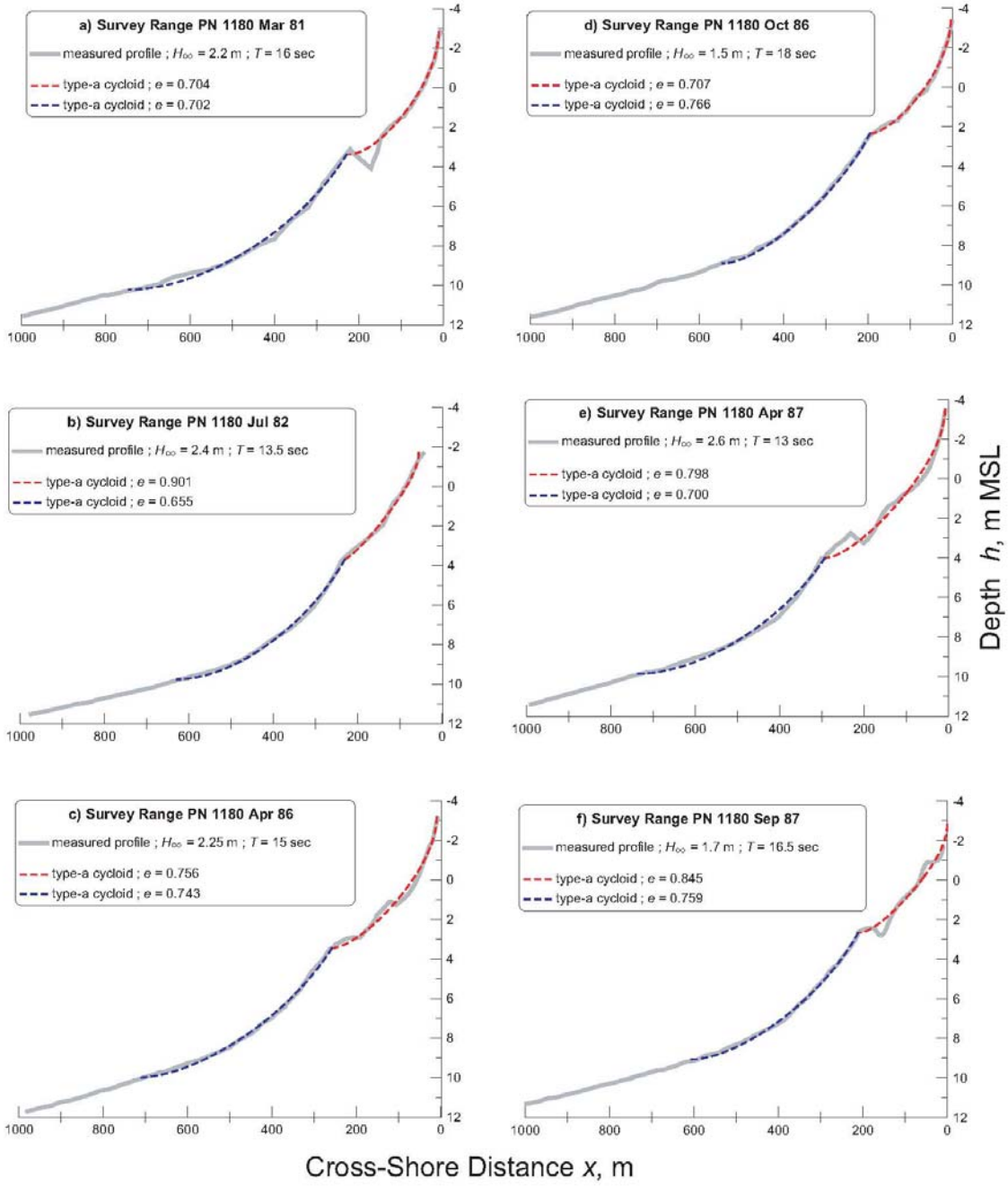

Figure 34. Comparison of beach profile survey data (gray) from Oceanside, CA, versus the elliptic cycloid equilibrium solutions for the shorerise (blue dashed) and bar-berm (red dashed). Calculated profiles based on CDIP wave monitoring data and median grain size D_2 = 100 μm with N = 10, and γ = 0.8.

type-a shorerise cycloids varied over a relatively narrow range $0.655 \le e \le 0.766$ with a mean of $\bar{e} = 0.721$, generally consistent with the shear stress formulations for smooth to moderately rough beds after Kajiura [1968] and *G. I. Taylor* [1946] , and in overal agreement with the larger ensemble statistics that were inferred from the analytic approximation in Figure 33a. The type-a bar-berm cycloids displayed a somewhat wider range of variability in eccentricity, $0.704 \le e \le 0.901$ with a mean of $\bar{e} = 0.785$. The range spanned all theoretical possibilities between the depth limited bore formulation and the average wave dissipation formulation, while the mean was still within the main peak of the large ensemble distribution found in Figure 33c. Therefore, the point-by-point accuracy of the type-a cycloid solution is not only good, but was achieved with ellipse parameters that are compatible with both process-based and empirically-based computations of those parameters.

The type-b cycloid solutions performed poorly on a point-by-point bases at PN1180 because of the broad bench or trough and bar that these profiles exhibit for eccentricities $e \ge 0.65$. This feature is not generally found on narrow shelf beaches such as those along the southern California coast. However, on wide shelf beaches such as the U.S. Gulf Coast, this feature may give the type-b cycloid a predictive skill advantage.

2.8 The Critical Mass of Equilibrium Sediment Cover

When an a series of type-a cycloid solutions for a broad range of wave heights are overlaid on an ensemble of many beach profile measurements, a well defined envelope of variability becomes apparent as illustrated in Figure 35. This figure combines 12 measured profiles over a 37 year period from two adjacent beaches near Oceanside that have geomorphic equivalence. Such comparisons with the cycloid solutions suggest that the volume of sand associated with long term beach

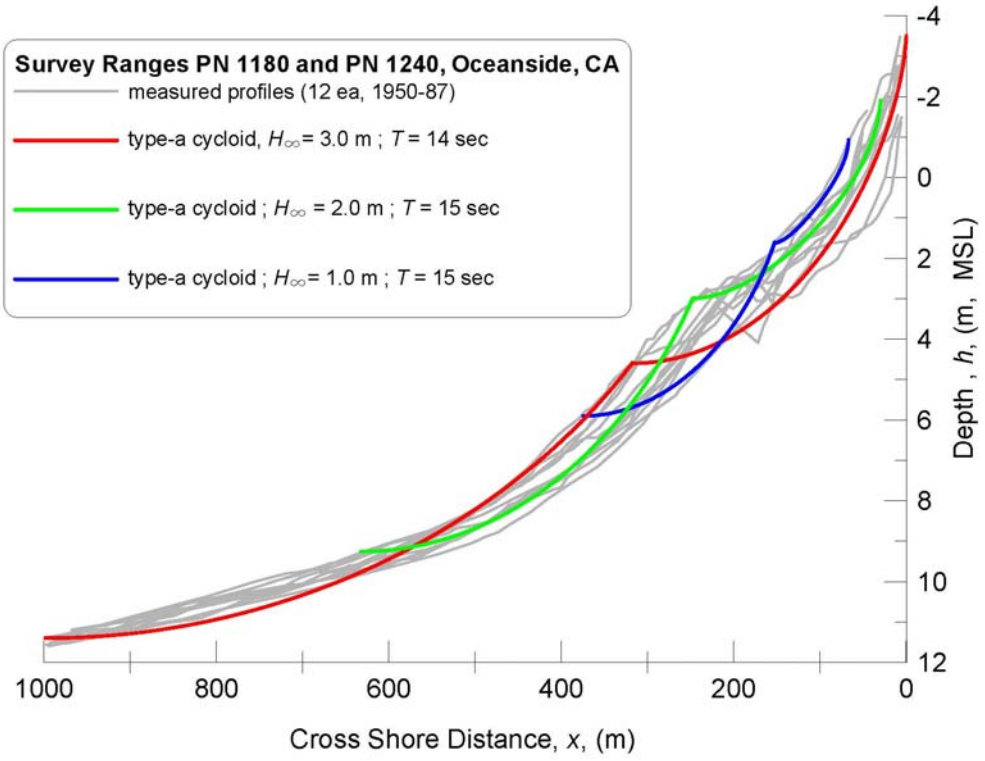

Figure 35. Envelope of variability of measured beach profiles (1950-87) at Oceanside, CA (grey) compared to the ensemble of elliptic cycloid solutions (colored) for selected incident wave heights and periods with D_2 = 100 μm, N = 10, γ = 0.8, and Λ = 0.814.

profile variations are directly calculable by integration of the cycloid solution between the limits of wave climate variation for a particular site. In this particular example, the wave height integrated cycloid solutions indicate that 1,180 m^3 of sand are involved with long term beach variability per each meter of shoreline. At lowest order, this volume represents the absolute minimum sand volume that the beach must retain in the long term in order for it to maintain a sustainable equilibrium. We refer to this minimum sand volume as the ***critical mass of sand***.

The critical mass of sand on a beach is that required to maintain equilibrium beach shapes over a specified time, usually ranging from seasons to decades. The critical mass for a seasonal beach is determined from the volume of the envelope of sand necessary to maintain continuous beach forms during the many changes in shape from one equilibrium state to another over a period of seasons (Jenkins and

Inman, 2003). There is no thermodynamic principle the can exclude changes in profile shape between equilibrium states involve transitional shapes that are non-equilibrium in form. However, as a first order approximation, we assume the critical mass envelope consists of a set of incremented equilibrium profiles, and the associated set of transitional profiles occurring between successive equilibrium states. Each profile in this set corresponds to a particular rms breaker height H_b that varies between some seasonal minimum H_{bo} and the critical wave height $\hat{H}_b$, the highest wave condition for which the existing sand supply can accommodate equilibrium and transitional profile adjustments. The equilibrium profiles are incremented by infinitesimal changes in wave height, $H_{bo} \le H_b + dH_b \le \hat{H}_b$, giving a continuous envelope of beach profile change. The volume of this envelope can be calculated from the thermodynamic solutions for the bar-berm profile, ζ_1, and the shorerise profile ζ_2 to solve for the volume of critical mass V_c per meter of shoreline (m^3/m):

$$V_c = \int_{H_\infty}^{\hat{H}_b} \int_{X_1}^{X_3} \frac{\partial \zeta_1}{\partial H_b} dx dH_b + \int_{H_\infty}^{\hat{H}_b} \int_{X_3}^{X_c} \frac{\partial \zeta_2}{\partial H_b} dx dH_b \qquad (55)$$

Analytic solutions to V_c are difficult because the thermodynamic solutions for the curvilinear coordinates (ζ_1, ζ_2) using elliptic cycloids are transcendental. Therefore solutions for the V_c envelope are obtained by numerical integration of (55) based on long term wave climate as shown in Figures 20-28. We use the number crunching capabilities **cycloid_ellipse_2.for** for this purpose. Figure 36 gives the critical mass solution resulting from numerical integrations of (55) using

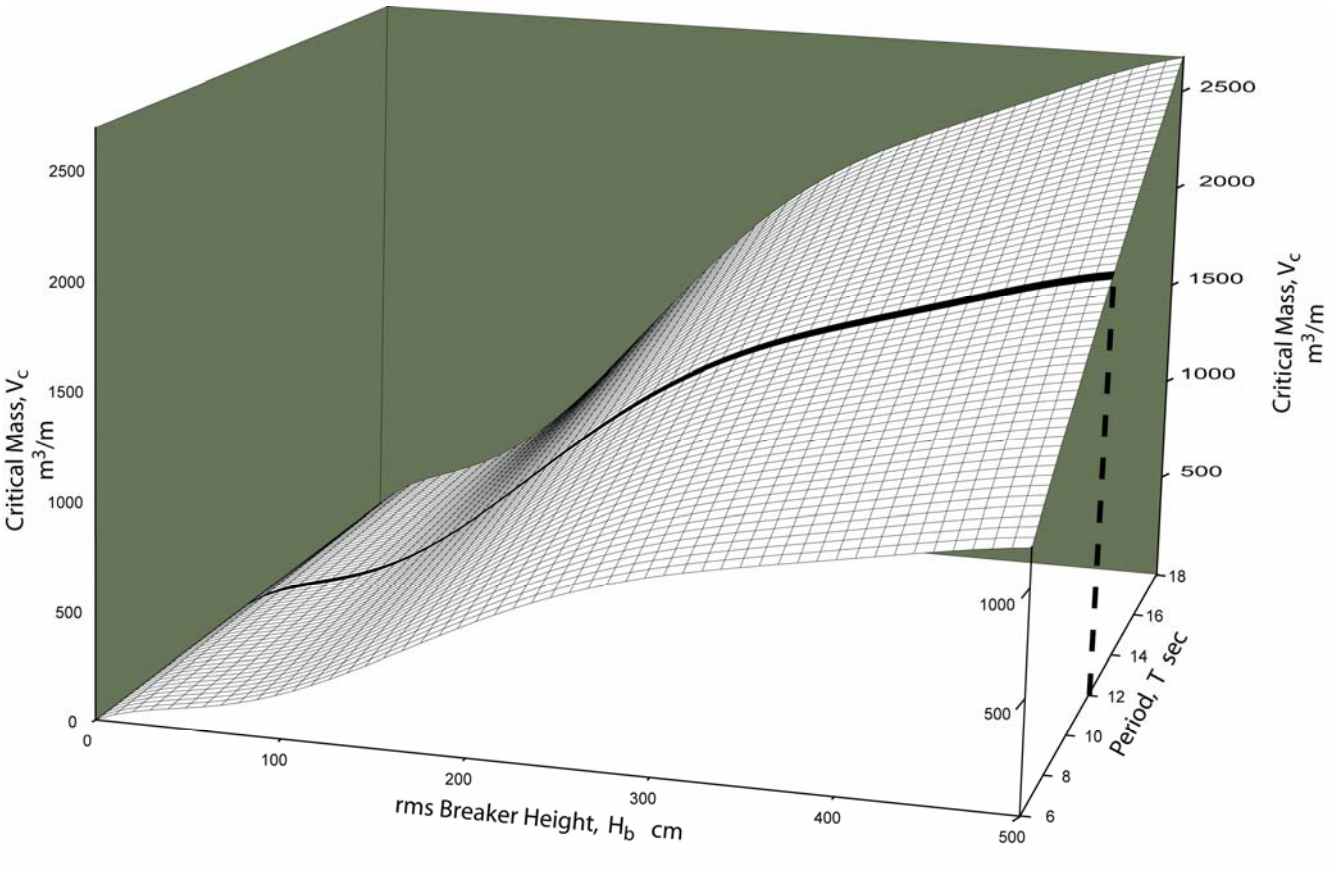

Figure 36: Three dimensional rendering of the total solution space of the critical mass. Black line corresponds to the solution in Figure 37 for D_1 = 225 microns and D_2 = 125 microns

the **cycloid_ellipse_2.for** codes. Because equilibrium and transitional profiles are grain size dependent through the closure depth condition, the volume of critical mass has a certain degree of sensitivity to grain size. Sensitivity analyses of (55) based on numerical integration show that finer grain sizes, particularly in the shorerise, tend to result in larger volumes of critical mass. This is shown in in Figure 37 with the wave period fixed. Longer curvilinear length ζ_1, ζ_2 and deeper closure depths h_c arise from finer grained sediment, thus resulting in physically

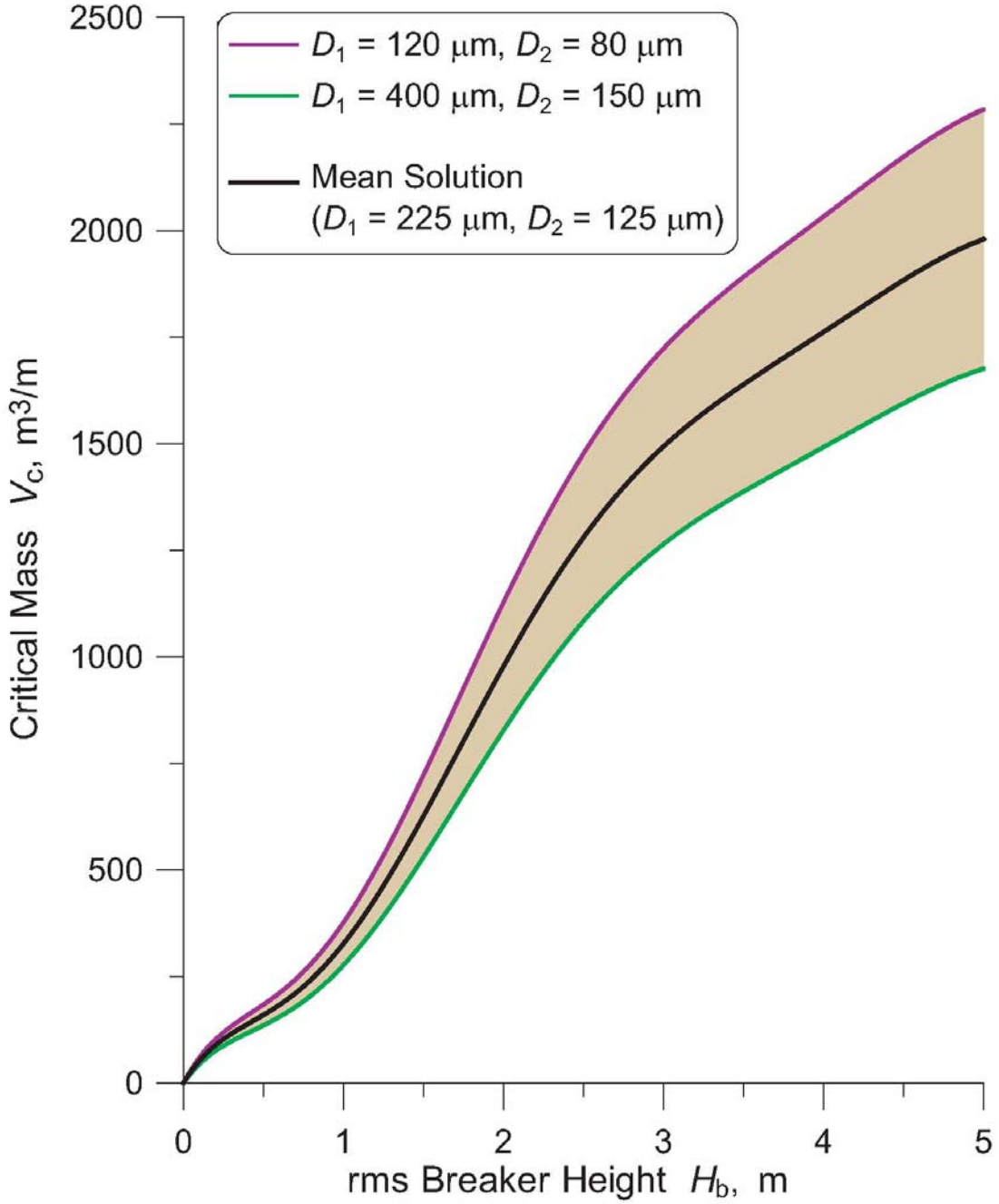

Figure 37: Critical mass elliptic cycloid solution with rms breaker height for 12 s waves breaking on variable sand size, D_1 in the bar-berm and D_2 in the shorerise. Curves are for continuous waves with rms breaker height Hb and Shields parameter of 30 at closure depth given by the relation in Figure 36.

larger critical mass envelops. However, the sensitivity of the volume of critical mass to grain size is second order relative to the dependence on wave height and period. A polynomial fit to the wave height dependence averaged over all grain sizes gives the following analytic approximation:

$$V_c \cong 500 H_b^{0.9} \tag{56}$$

where H_b is in meters, giving V_c in m^3 per meter of beach length.

2.9 Effect of Sealevel Rise on Equilibrium Sediment Cover.

We are now in a position to link several of the LCM codes to determine the combined effects of sea level on refraction/diffraction, the equilibrium profile of the sediment cover and the critical mass. This is accomplished by setting the parameter **sealev** in the **cdip_histogram_percentile_soi.for** codes and the parameter **ak** in the **cycloid_ellipse_2.for** codes for the particular sealevel anomaly obtained from the sea level function produced by **sea_level_waz.** Figure 38 reveals the net effect of a 50 cm rise in mean sealevel relative to present. We find that the equilibrium profile of a sediment cover of constant volume is shifted landward by 27 m, while the bar berm origin is rasied by an increment equivalent to the sealevel anomaly. The net effect of these two profile adjustments to sea level rise is to increase the critical mass of sand required to sustain the beach equilibrium forms. Numerical experiments with the **cycloid_ellipse_2.for** codes indicate that an increase in sea level of $\Delta\eta$ will alter the lowest order critical mass approximation

to become:
$$V_c \cong 500\left\{H_b\left[1+\left(\frac{\gamma\,\Delta\eta}{\Lambda H_b}\right)^{\alpha}\right]\right\}^{0.9} \tag{57}$$

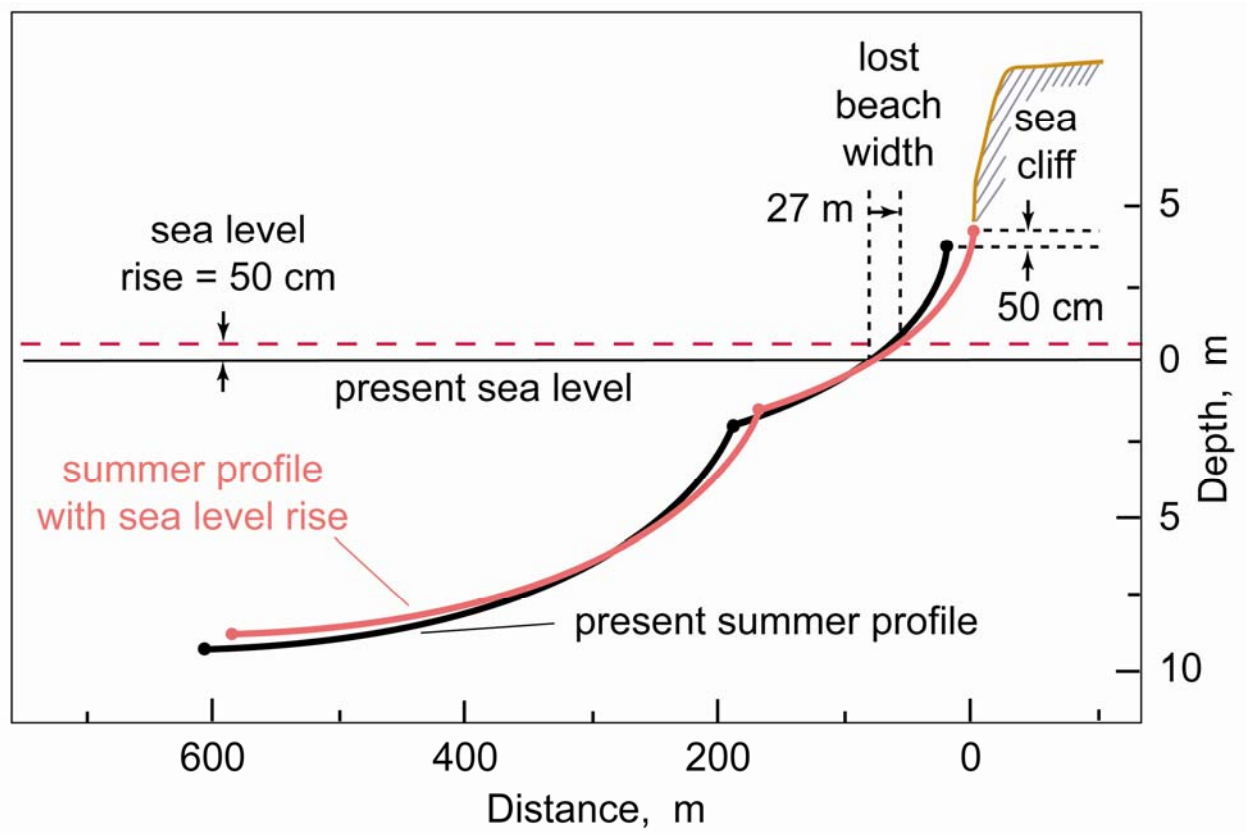

Figure 38: Effect of sealevel rise on the equilibrium profile of a sediment cover of constant volume.

3. Bedrock Cutting Model (BCM) Algorithms and Code Documentation

When the sediment mass becomes sufficiently depleted by a cumulative negative divergence of drift as in Figure 16, the critical mass envelope will intersect the underlying bedrock as shown schematically in Figure 39. In this case, further depletion of sediment mass by continued negative divergence of drift can not be compensated by equilibrium profile adjustments. Instead the sediment cover profile will assume a non-equilibrium form referred to as a ***disequilibrium profile*** (Inman, et. al., 1993). The disequilibrium profile will bare a certain portion of the

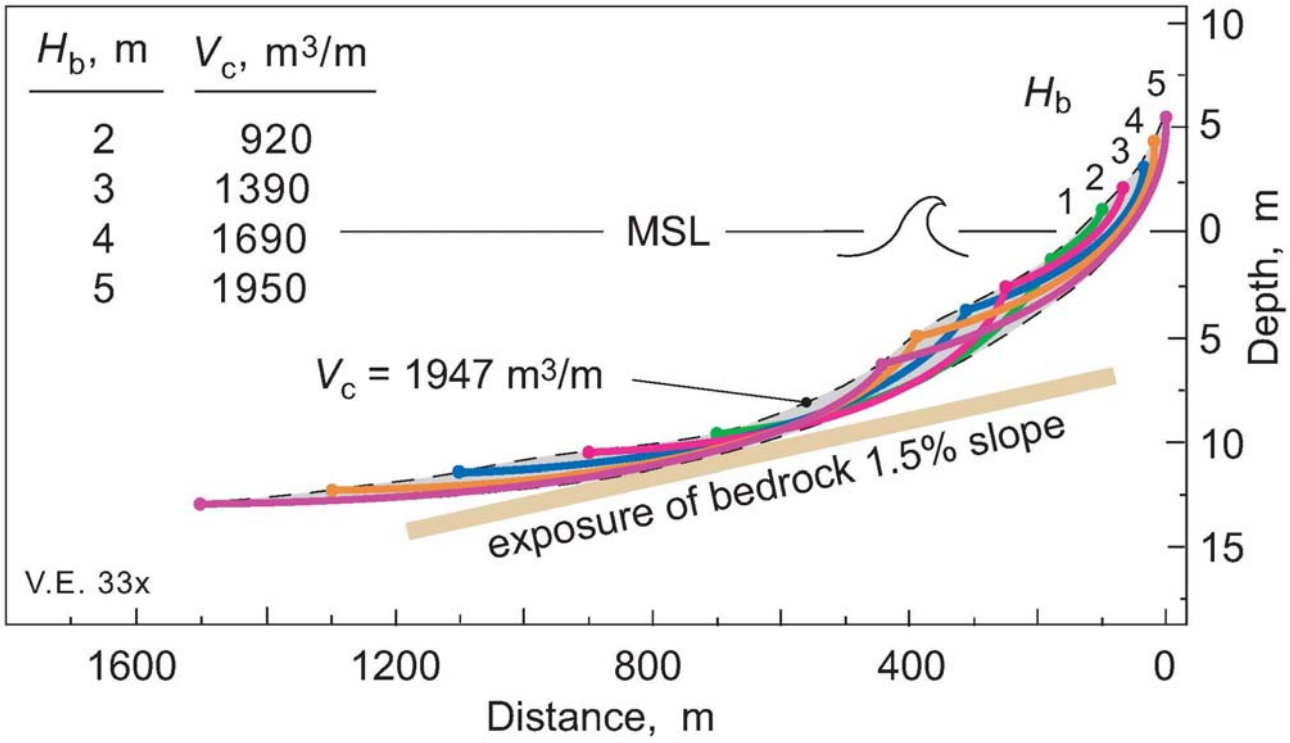

Figure 39: Equilibrium beach profiles for 12 s waves and rms breaker height H_b. V_c is the critical volume of sand required for equilibrium.

bedrock surface to the direct action of wave induced bottom friction. This bottom friction will cause the basal conglomerate consisting of gravels and cobbles to scrub back in forth in oscillatory motion, abrading the bedrock surface in the process. This action produces a wave cut platform in the bedrock surface. If abrasion of the denuded bedrock continues over a long period of time, the platform will continue to cut landward, eventually intersecting the toe of the sea cliff (Figure 40). This results in notching or under-cutting of the toe of the sea cliff, leading to collapse of the seaward face of the sea cliff, and recession of the sea cliff formation. In this section we detail three separate codes that make up the BCM and simulate these bedrock cutting processes: 1) the **cn_scour_osc.for** code (Appendix-K) that computes the disequilibrium profile and bottom friction over the bedrock surface; 2) the **bedrock_cutting-3.for** codes (Appendix-L) that computes the the abrasion of the exposed bedrock surface and development of the wave-cut platform in the bedrock formation; and 3) the **cliffing_model_4_leg.for** codes (Appendix-M) that compute the erosion of the cliff face and the sea cliff recession. We begin by describing the 3-dimensional data bases needed to run these codes in simulations of the Torrey Pines Sub-Cell (Figure 10).

3.1 Bathymetry and Sub-Bottom of the Torrey Pines Sub-Cell

The interpolations of both the sub-bottom and bathymetry grids for the Torrey Pines Subcell were done using the ESRI ArcInfo program TOPOGRID. The grid cell spacing was set at 20m for each interpolation. Both interpolations used the 0 MSL contour extracted from the SANDAG 10m Digital Elevation Map (DEM) for the land boundary. The sea boundary in each case was defined by the -100 m contour extracted from USGS/NOS 3-arc second database. The Bathymetry

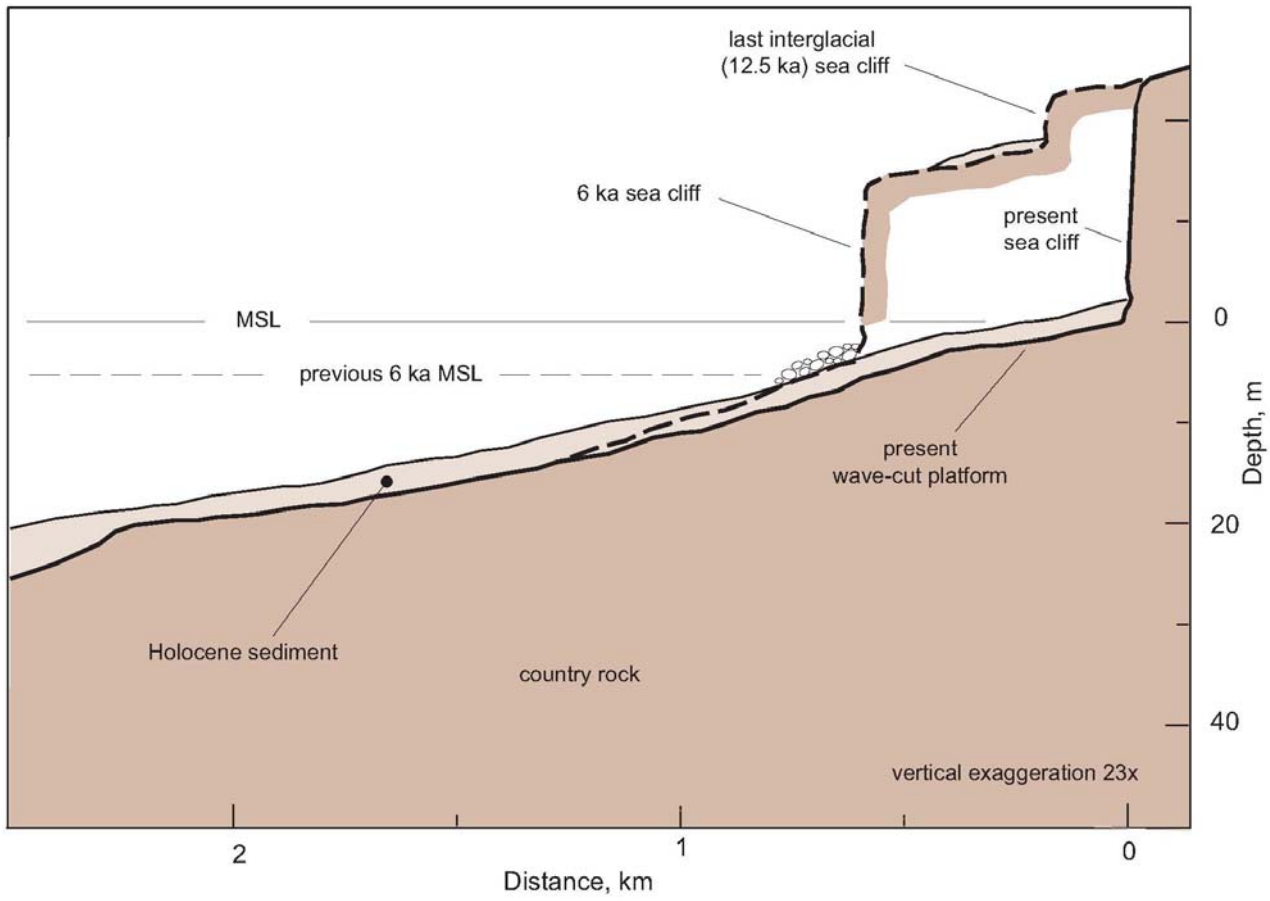

Figure 40: Generalized section showing the present wave cut terrace (with sand), the previous locations of the 6 ka terrace (with cobbles), and the perched remnants of the last interglacial terrace (125 ka) with sand beaches. Regional uplift for the Oceanside littoral cell is ~ 15 cm/ka.

raster (Figure 41) includes contours at 10 m spacing extracted directly from the USGS/NOS DEM.

In addition to the land boundary contour and -100 m sea boundary contours, the Subbottom raster (Figure 42) incorporated point data from Jet Probe data (CCSTWS 88-5) at 4 ranges, north to south, SD600, DM560, TP530, TP470, subbottom profiles from USGS multibeam survey ranges 229x, 230xd, 230x, 162x, 232x, 233x, 902x, 165x, 235x, 237xa, and 237xd (USGS 2000) , and high resolution subbottom surveys in the region between Los Penasquitos lagoon and

the SIO submarine canyon (Driscoll, 2000). After the initial Subbottom interpolation, excessive irregularities were present in the interpolated raster that could not be justified by the underlying data. A second interpolation was performed using the same initial data plus subbottom contours extracted from the first interpolation. This 2nd interpolation eliminated much of the spurious irregularities which producing no deviations from the actual data points. Under ideal conditions with ample subbotom data the 2nd interpolation would not have been necessary. For example if we had data points spaced everywhere in the Torrey Pines Sub-cell at a spacing comparable to the Driscoll (2002) data the 2nd interpolation would not have been necessary. However, under the circumstances of limited subbottom survey data, we feel this was a satisfactory result for the gridded sub-bottom shown in Figure 42.

The gridded bathymetry in Figure 41 and sub-bottom (bedrock surface) in Figure 42 provide the shape files on which the BCM was run. The difference between these two surfaces (Figure 41 minus Figure 42) provides the basline sediment cover (isopach) on which the BCM and CEM were run for long range forecast simulations described in Section 4.

3.2 Scour Algorithms for the Bedrock and Sediment Cover

Once the critical mass envelope impinges on the bedrock surface (Figure 39), the thermodynamic solutions from Section 2.5 can no longer be applied. At this point, subsequent time step computations are through-put below the blue line in the Figure-1 architecture, engaging a set of mechanics based scour algorithms to calculate the disequilibrium sediment cover and bottom friction acting over the exposed bedrock surface. These scour algorithms are based on vortex lattice theory applied to oscillatory wave-induced motion.

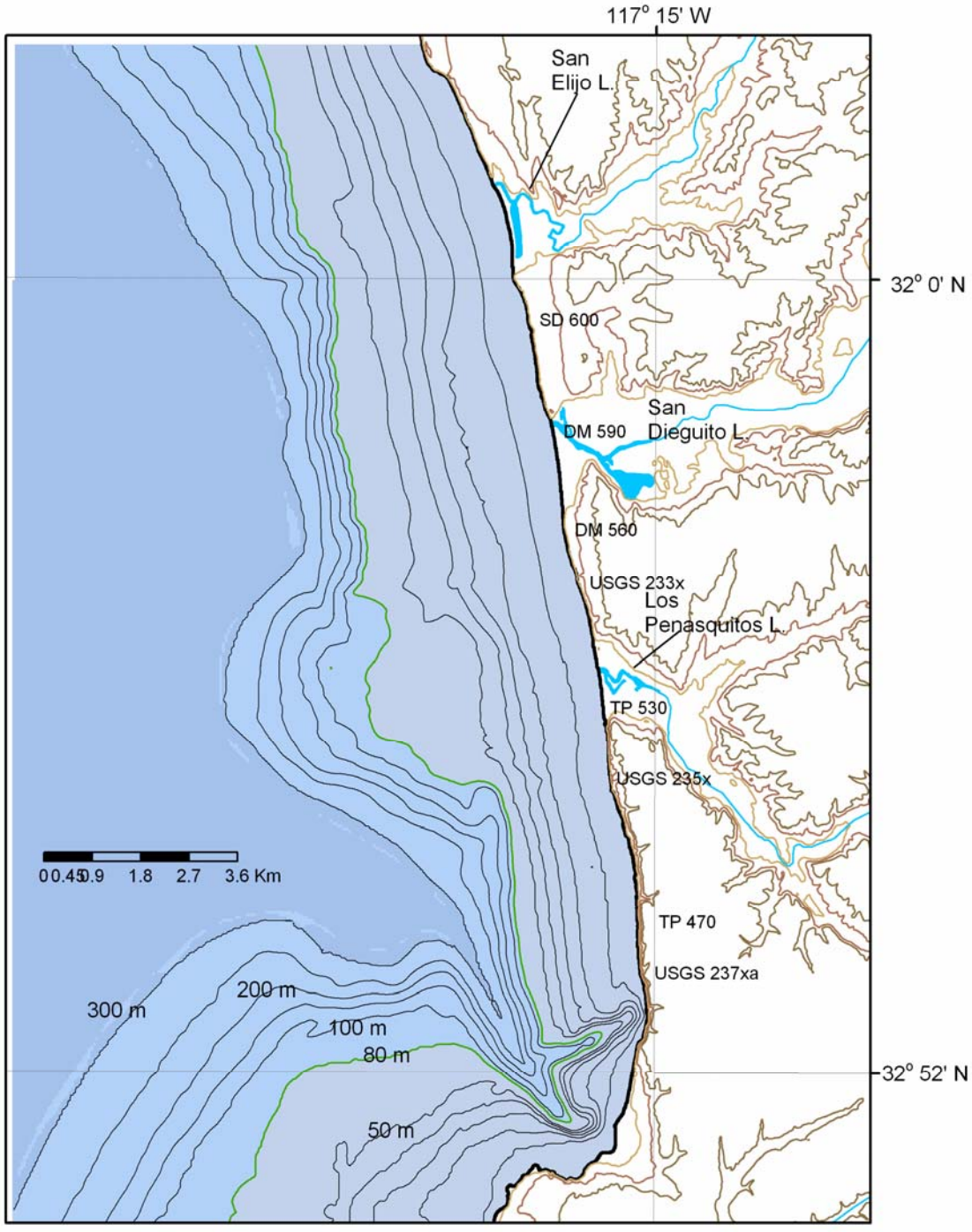

Figure* 41: Torrey Pines Subcell bathymetry (time zero sediment surface). Depth contours shown in meters mean sea level from the GIS grid file *bottom20.txt

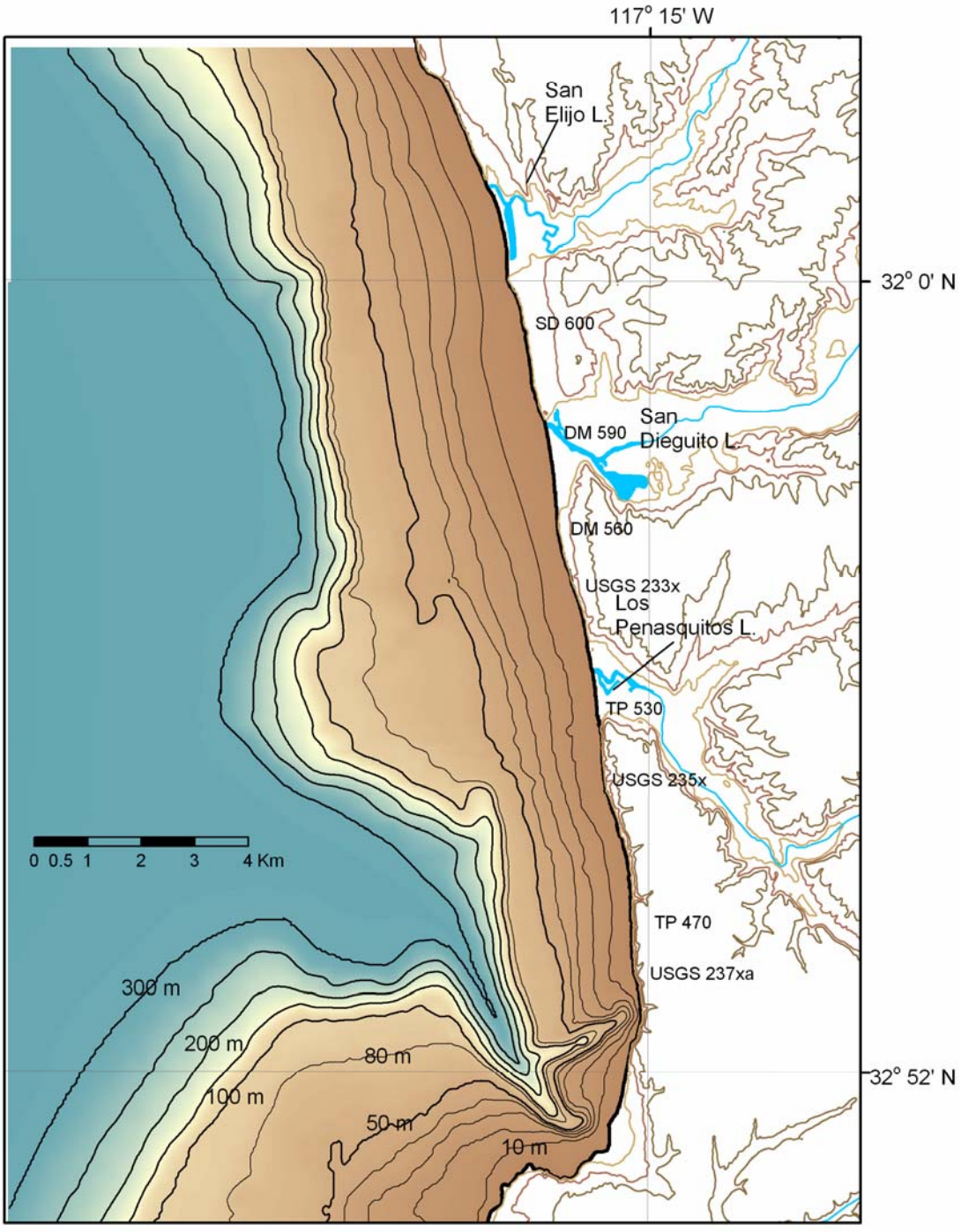

Figure 42: Torrey Pines Subcell sub-bottom (time zero bedrock surface). Contours shown in meters mean sea level from the GIS grid file *subbot20.txt*

For the any given i^{th} grid cell in the grid of the Torrey Pine Sub-cell, there exists a horseshoe vortex (Figure 43) consisting of a bound vortex Γ_o that contains all of the vorticity generated on the surface of a grid cell, and a pair of trailing vortex filaments, $+\Gamma_i$ and $-\Gamma_i$, that discharge vorticity from the grid cell into the flow, causing a vortical wake. The trailing vortex filaments scrub the seabed and induce scour and suspension of bottom sediment as shown schematically in Figure 44. The circulation of the vortex Γ_o bound to the grid cell is calculated from the boundary layer velocity shear [Batchelor, 1970]:

$$\Gamma_o = \int_0^{\delta} \int_{x_n}^{x_{n+1}} \left\{ \Re\left(\frac{\partial \tilde{u}}{\partial z} \right)^2 \right\}^{1/2} dx dz \tag{58}$$

where $\Re$ is the real part operator and the shear of the near-bottom flow, $\partial u / \partial z$, is prescribed from the wave/current boundary layer profile from Jenkins and Inman (1985),

$$\begin{aligned} \tilde{u} &= u^{(1)} e^{i\sigma t}(1 - e^{-\alpha}) \\ &+ u^{(2)} \left[-\alpha e^{-\alpha^*} + \left(1 - \frac{3}{2}i\right) e^{-\alpha^*} - \frac{i}{2} e^{-\alpha} + \left(\frac{i}{2} - \frac{1}{4}\right) e^{-2r/\delta} - \frac{3}{4} + \frac{3}{2}i \right] \end{aligned} \tag{59}$$

where $u^{(1)}$ is the local oscillatory velocity amplitude at the top of the boundary layer $u^{(1)} = \nabla\phi$, and $u^{(2)}$ is the steady streaming at the top of the boundary layer $u^{(2)} = 3\nabla\left(u^{(1)}\right)^2 / 8\sigma$. The radian frequency of the wave oscillation is σ and the

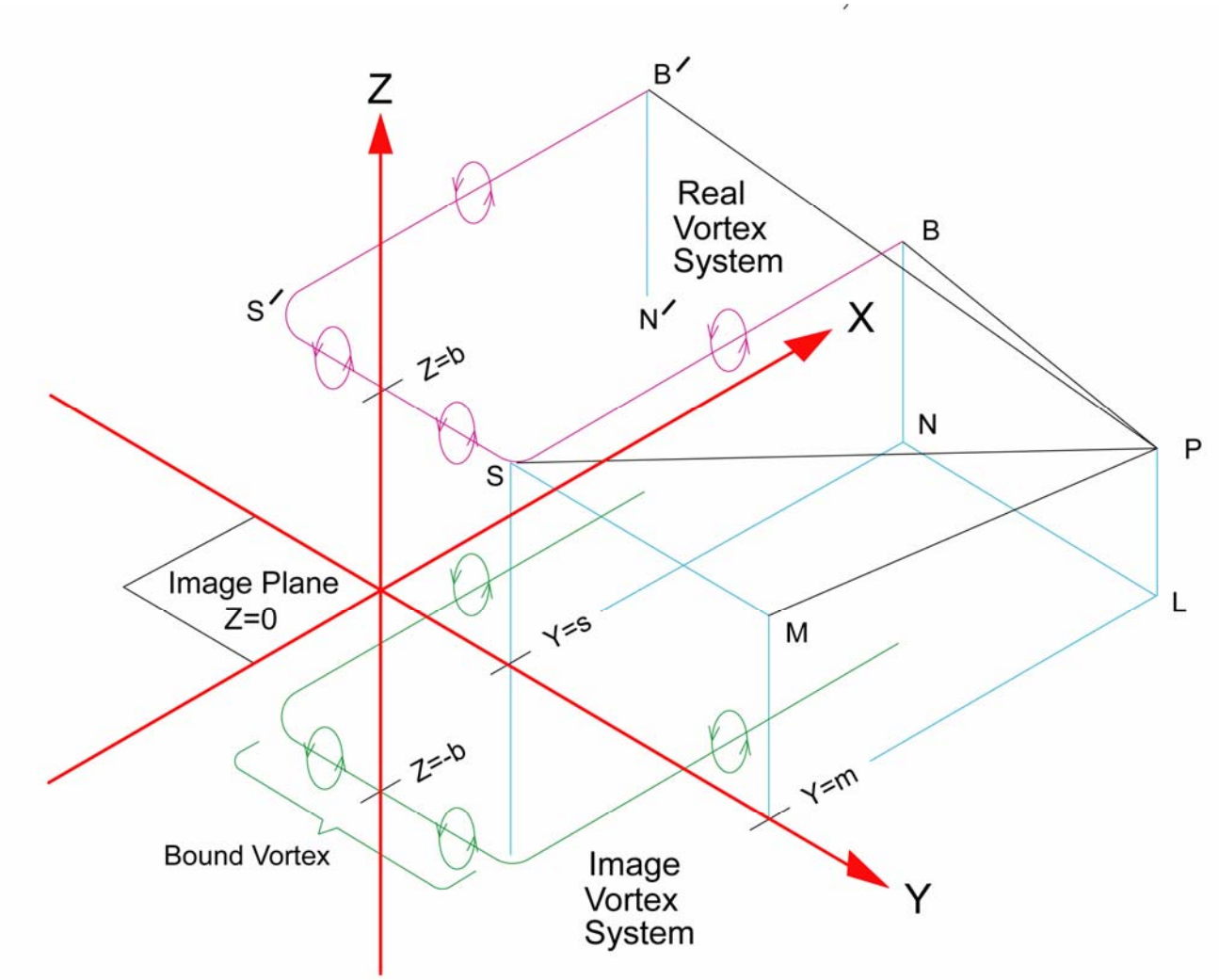

Figure 43: Image method for vortex lattice method. Vortex induced velocity at any point "P" near the bed due to the horsedhoe vortex of an arbitrary grid cell in the sub-cell grid. The real vortex over the sea bed is diagrammed purple while the image vortex is green.

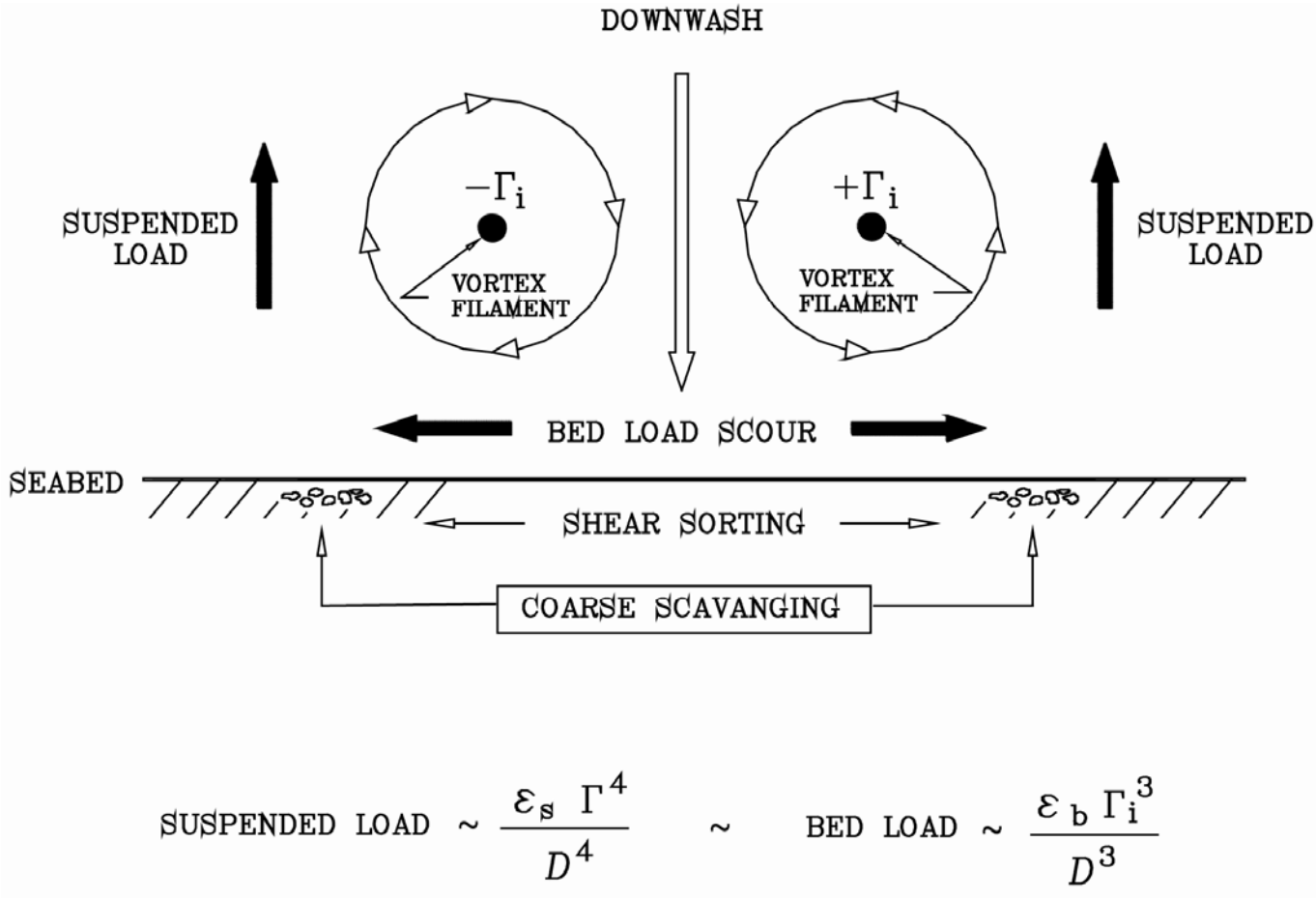

Figure 44: Schematic in the along shore plane of a pair of vortex filaments trailing in the cross-shore direction (in and out of page).

boundary layer profile is given by $\alpha = (1+i)r/\delta$ in terms of the local surface normal coordinate *r*. Complex conjugates are denoted by a star (*).

The boundary layer thickness used to evaluate (58) and (59) is derived from the work of Jonsson and Carlsen (1976) by finding local solutions for each grid cell to the transcendental equation:

$$\frac{30\delta}{Z_i}\log\left(\frac{30\delta}{Z_i}\right) = 1.2\left(\frac{d_0}{2Z_i}\right) \tag{60}$$

where Z_i is the elevation of the i[th] grid cell above the seabed. The factor d_0 / Z_i in (60) accounts for lowest order inertial effects associated with the wave orbital velocity amplitude u_m as represented by the inverse Strouhal number $\mathbf{St} = u_m / \sigma L$ for a characteristic length scale $L \sim Z_i$.

The trailing vortices consist of right/left pairs whose circulation have equal but opposite rotation, $+\Gamma_i$ *vs* $-\Gamma_i$ as shown in plan view in Figure 43 and in cross section in Figure 44. To prevent these vortices from inducing normal flow through the bottom plane, there is a set of image vortices beneath the bottom plane (ground effect). The mathematical representation of the trailing vortex filaments from a grid cell is derived from lifting line theory in ground effect according to Van Dyke, (1964 and 1975). Taking *x* as the cross shore coordinate along the axis of wave propagation, *y* as the along shore component (parallel to the wave crests), and *z* measured vertically upward from the undisturbed seabed plane, the horseshoe vortex for the i[th] grid cell in the sub-cell is represented by,

$$\Gamma_i = -\frac{\Gamma_o}{4\pi}\left\{\tan^{-1}\left[\frac{(z-Z_i-b')(y+S)}{x\sqrt{x^2+(y+S)^2+(z-Z_i-b')^2}}\right]-\tan^{-1}\left[\frac{(z+Z_i+b')(y+S)}{x\sqrt{x^2+(y+S)^2+(z+Z_i+b')^2}}\right]\right\}$$

$$-\frac{\Gamma_o}{4\pi}\left\{\tan^{-1}\left[\frac{(z+Z_i+b')(y-S)}{x\sqrt{x^2+(y-S)^2+(z+Z_i+b')^2}}\right]\right\}-\frac{\Gamma_o}{4\pi}\left\{\tan^{-1}\left[\frac{(z-Z_i-b')(y-S)}{x\sqrt{x^2+(y-S)^2+(z-Z_i-b')^2}}\right]\right\}$$

$$-\frac{\Gamma_n}{4\pi}\left\{\tan^{-1}\left[\frac{(z+Z_i+b')}{(y-S)}\right]-\tan^{-1}\left[\frac{(z-Z_i-b')}{y-S)}\right]\right\} \tag{61}$$

$$-\frac{\Gamma_n}{4\pi}\left\{\tan^{-1}\left[\frac{x(z+Z_i+b')}{(y-S)\sqrt{x^2+(y-S)^2+(z+Z_i+b')^2}}\right]-\tan^{-1}\left[\frac{x(z-Z_i-b')}{(y-S)\sqrt{x^2+(y-S)^2+(z-Z_i-b')^2}}\right]\right\}$$

$$-\frac{\Gamma_n}{4\pi}\left\{\tan^{-1}\left[\frac{(z-Z_i-b')}{(y+S)}\right]-\tan^{-1}\left[\frac{(z+Z_i+b')}{(y+S)}\right]\right\}$$

$$-\frac{\Gamma_n}{4\pi}\left\{\tan^{-1}\left[\frac{x(z-Z_i-b')}{(y+S)\sqrt{x^2+(y+S)^2+(z-Z_i-b')^2}}\right]-\tan^{-1}\left[\frac{x(z+Z_i+b')}{(y+S)\sqrt{x^2+(y+S)^2+(z+Z_i+b')^2}}\right]\right\}$$

where *S* is the half-width of a grid cell in the along shore direction. The first two lines of (61) represent the bound segment of the horseshoe vortex system that is attached to the grid cell surface, the next two lines are the $+\Gamma_i$ trailing vortex filament (right hand side of Figure 44) , while the last two lines are the $-\Gamma_i$ trailing vortex filament (left hand side of Figure 44). As the pair of trailing vortex filaments extend cross shore, their circulation decreases due to diffusion of vorticity, as prescribed by Peace and Riley (1983),

$$\Gamma_n = \Gamma_o f(x) \tag{62}$$

The trailing filaments decay downstream due to ground effect friction over the seabed, as expressed by the decay function:

$$f(x) = 1 - \frac{1}{u_m} \int_0^{N\Delta x} \left\{ u^{(1)} + u^{(2)} \left(\frac{x\sigma}{u_m S^2} \right)^{1/2} + \left(\frac{x\sigma}{u_m S} \right) \left(u^{(1)} + S^2 \frac{\partial^2 u^{(2)}}{\partial x^2} \right) \right\} dx \qquad (63)$$

where N is the number of grid cells in the Torrey Pines Sub-Cell. The factor b' in (61) is the displacement thickness associated with the rms vorticity of the bound vortex of a grid cell. From Peace and Riley (1983) we take

$$b' = \int_0^{\infty} \left(1 - \frac{\Gamma_o}{u\delta} \right) dz \cong 1.344\delta \qquad (64)$$

The release of trailing vortex filaments from each grid cell causes scour of the neighboring seabed. When viewed in any along shore plane (Figure 44) each pair of filaments induces a downwash flow that converges on the seabed and results in lateral bedload scour proportional to the cube of the vortex strength Γ_i, and inversely proportional to the cube of the grain size D. Beyond the lateral extent of the bedload scour, the vortex filaments induce an upwashing flow of suspended load, proportional to Γ_i^4 / D^4. The bedload scour rate for any given vortex filament (i-vortex) is given by

$$i_{bi} = \frac{\varepsilon_b C_D \rho \Gamma_i^3}{D^3 (\tan\varphi - \tilde{u}\beta / |\tilde{u}|)} \qquad (65)$$

and the suspended load scour is

$$i_{si} = \frac{\varepsilon_s C_D \rho \Gamma_i^3 |\Gamma_i|}{D^4 (W_o - \tilde{u}\beta)} \qquad (66)$$

where ε_b is the bedload transport efficiency, ε_s is the suspended load transport efficiency, C_D is the seabed drag coefficient which is a function of bed roughness, W_o is the settling velocity for any given sediment grain size bin represented by a characteris tic grain diameter D and β is the local slope of the seabed. The scour

rates calculated for each vortex filament from (63) and (64) are summed over all the vortex filaments in the Torrey Pines Sub-Cell grid to calculate the complete scour field around the mine. Note that the scour due to (65) and (66) selectively removes the finer grained fraction of the bed material (winnowing of fines) and leaves behind the coarser grained fraction that becomes basal conglomerate (Figure 45).

The scour rates per unit length of grid cell from (65) and (66) are integrated over the length of the grid cell Y_L to determine the scour volume flux

$$Q_{scour} = \int_0^{Y_L} \frac{(i_{bi} + i_{si})}{(\rho_s - \rho)} g N_0 dy \tag{67}$$

When the scour volume flux is added to the loss terms in (6), the disequilibrium profile at any time $t = j\Delta t$ at the j^{th} time step in the simulation becomes

$$x = \frac{2r\, I_e^{(k_{1,2})}}{\pi\, \varepsilon} (\theta - \sin\theta) - \int_0^{j\Delta t} \frac{(J + Q_{L1} - Q_{RE} - Q_{L1} - Q_{scour})}{Y_L (Z_1 + h_c)} dt \tag{68}$$

Equation (68) provides a coupling mechanism between the LCM and BCM, whereby the disequilibrium profile represents a sour perturbation of the critical mass envelope.

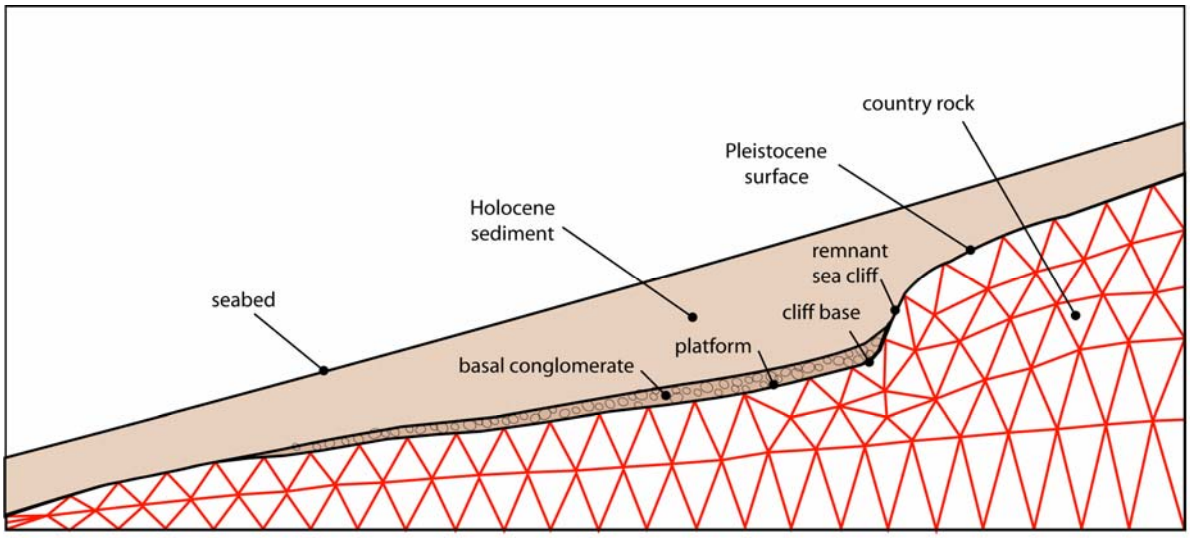

Figure 45. Illustration of wave-cut terrace notched into the country rock and now found on the shelf by seismic profiling below a cover of Holocene surface sediment.

3.3 Scour Codes for the Bedrock and Sediment Cover

The scour algorithms (58)-(68) have been coded to run on the sediment and bedrock surfaces of the Torrey Pines Sub-Cell in the the **cn_scour_osc.for** codes found in Appendix-K. These compute the disequilibrium profile and bottom friction over the bedrock surface using initial inputs of GIS shape files for the sediment surface (**bot20.txt)** and for the bedrock surface (**subbot20.txt).** The input parameters output files which are required by **cn_scour_osc.for** are :

bottom20.txt *datin …… 3-d xyz bathymetry shape file Torrey Pine Sub-cell

subbot20.txt *datin_2…...3-d xyz sub-bottom shape file Torrey Pine Sub-cell

bot20_s.dat…….. *datout - 3 dimension scour file

bot20_b.dat…….. *dato_2 - 3 dimension bottom file

201…….. *ix number of x-grid cells

20.0 …….. *xinv (in cm) x-grid cell dimension

201…….. *jy number of y-grid cells

20.0 …….. *yinv (in cm) y-grid cell dimension

0.0…….. *z vertical datum (0.0 for m MSL)

4.951…….. *eps momentum diffusivity (cgs)

1.524…….. *delx (in cm)

9.144 …….. *dely (in cm)

0.5 …….. *cl vortical coefficient

1.0 …….. *cf friction coefficient

60.0 …….. *u0 (in cm/sec) max longshore mean current (cgs)

980.0 …….. *g acceleration of gravity (cgs)

1.023 …….. *rhom density of seawater (cgs)

0.0002185…….. *alpha cross-flow angle

150.0 …….. *tauc threshold shear stress

0.75 …….. *str vortex stretching factor (ala, Peace & Riley)

0.0 …….. *r_test first marker point -20.7264

0.0 …….. *s_test first marker point -3.6576

-20.0 …….. *ak_bot max thickness of sediment cover (m)

10.0 …….. *bur max elevation of bedrock platform (m MSL)

-40.0…….. *u2 (cm/sec) max cross-shore mean current

50 …….. *jsy y grid cell number of the seaward end of control cell

The **cn_scour_osc.for** code inputs the 20 x 20 meter resolution bot20.txt bottom file and generates a scour and bottom friction file called **bot20_s.dat** and a revised bottom file for the disequilibrium profile called **bot20_b.dat.**

Figure 46 gives an example of a disequilibrium profile computed by **cn_scour_osc.for** at range line TP 470 in the Torrey Pines Sub-cell (location noted on Figures 41 and 42). These simulations are based on continuous looping of the 20 year CDIP wave record (Figure 12) with all water shed sediment source terms (J) in (5), (6) and (68) zeroed out (as during protracted drought). In the absence of new sediment input from rivers (J=0) we find partial denuding of the bedrock after 46 years of simulation. With incremented equilibrium profile change using just the LCM we get denuding of the bedrock in 2 segregated inshore zones (see colored profile lines in Figure 46). Between these two denuded zones we find an intermediate bar covering the bedrock where the bar berm and shorerise profiles conjoin. This result is an ephemeral equilibrium state, with no subsequent equilibrium states possible once the thermodynamic solution intersects the bedrock surface. This ephemeral equilibrium does not conform to observations that show total denuding of the inner shorezone once the bedrock is exposed anywhere in the inner shorezone (according to the classic disequilibrium condition reported in Inman, et al, 1993). However, subsequent disequilibrium profiles are obtained with the coupled LCM/BCM using the **cn_scour_osc.for** code based on (58)-(68). One such subsequent state is shown by the dashed black line in Figure 46 representing a disequilibrium profile with all the classic features, namely: a steep foreshore berm section that intercepts the bedrock at it's seaward toe; complete denuding of the inner shore zone between the foreshore berm and closure depth; and a closure depth bar formation. In the denuded portion of the shorezone, the output file

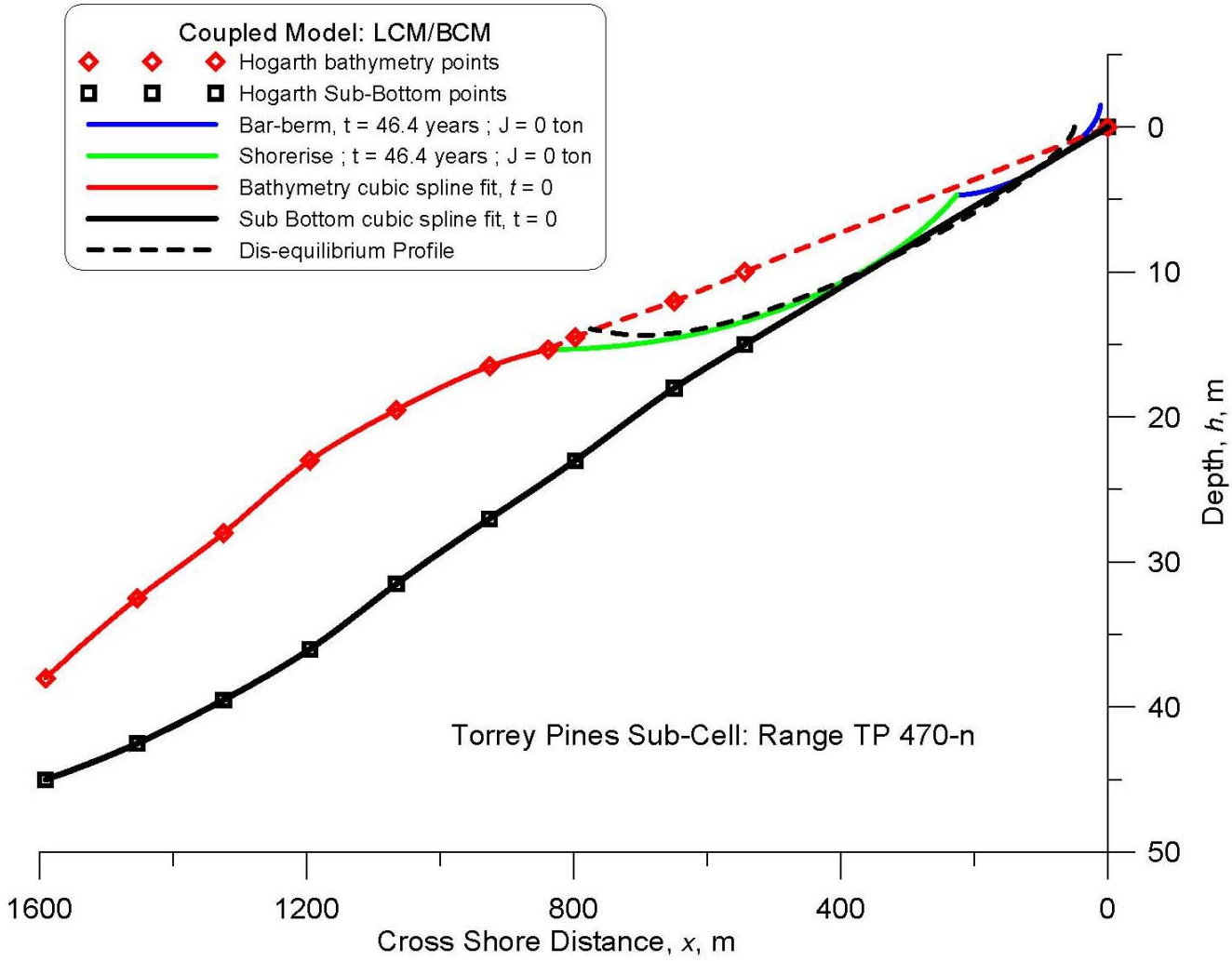

Figure 46: Profiles of sediment cover and bedrock surface at range TP-470 north in the Torrey Pines Sub-cell. Present surface of sediment cover (from bot20.txt) indicated by red profile lines (solid and dashed) with recent bathymetric 2004 updates by Hogarth shown as red diamonds. Bedrock surface (from subbot20.txt) shown as black line profile with black diamonds indicating bathymetric 2004 updates by Hogarth. The 46.4 year simulation of the LCM equilibrium profile change shown as blue and green curves. Coupled LCM/BCM simulation of the disequilibrium scour profile shown as dashed black curves. Both simulations based on no river sediment input to littoral cell.

bot20_s.dat provides the bottom friction solutions for use in the bedrock cutting algorithms.

3.4 Bedrock Cutting Algorithms for Wave-Cut Platforms and Seacliffs.

The governing equations and the boundary conditions (1-4) are cast as a set of integral functionals in a variational scheme, [Boas, 1966]. The bedrock cutting algorithms are applied to vertical bedrock planes oriented cross-shore along the boundary sides of each control cell in the Torrey Pines Sub-cell, as shown schematically in Figure 3. These cross-shore bedrock planes are gridded into a mesh of 3-node triangular elements bounded by the bed rock surface along one side as shown in Figure 45. Within the domain of each of "i" elements that make up the bedrock gridded mesh, the unknown solution $\mathbf{A_i}$ to the governing equations is simulated by a set of ***trial functions*** $(\hat{H}, \hat{q})$ having adjustable coefficients. The trial functions are substituted into the governing equations to form ***residuals*****, ($\mathbf{R_H}$, $\mathbf{R_q}$)**. The residuals are modified by ***weighting functions,*** **(ΔH, Δq)**. The coefficients of the trial functions are adjusted until the weighted residuals vanish. The solution condition on the weighted residuals then becomes:

$$\iint_{A_i} R_H \Delta H dA = 0$$
$$\iint_{A_i} R_q \Delta q dA = 0 \qquad (69)$$

By the Galerkin method of weighted residuals, [Finlaysen, 1972], the weighting functions are set equal to nodal ***shape functions***, **<N>**, or:

$$\begin{aligned} \Delta H &\sim N_i \\ \Delta q &\sim N_j \end{aligned} \qquad (70)$$

The shape function, <N>, is a polynomial of degree which must be at least equivalent to the order of the highest derivative in the governing equations. The shape function also provides the mechanism to discretize the governing equations. Figure 47 gives the shape function polynomial in terms of ***global (California)*** coordinates for the first nodal point, $\mathbf{N_1}$ of a generalized 3-node triangular element of area $\mathbf{A_i}$. Wang (1975) obtained significant numerical efficiency in computing the weighted residuals when the shape functions of each nodal point, $\mathbf{N_i}$, are transformed to a system of ***natural*** coordinates based upon the unit triangle, giving $\mathbf{N_i} \rightarrow \mathbf{L_i}$ as detailed in Figure 47b. The shape functions also permit semi-discretization of the governing equations when the trial functions are posed in the form:

$$\begin{aligned} \hat{H}(x,y,t) &= \sum_i H_i(t) N_i(x,y) \\ \hat{q}(x,y,t) &= \sum_j q_j(t) N_j(x,y) \end{aligned} \qquad (71)$$

Discretization using the weighting and trial functions expressed in terms of the nodal shape functions allows the distribution of dependent variables over each element to be obtained from the values of the independent variables at discrete nodal points. However, the shape function at any given nodal point, say $\mathbf{N_1}$, is a function of the independent variables of the two other nodal points which make up that particular 3-node triangular element, see Figure 47a & b. Consequently, the

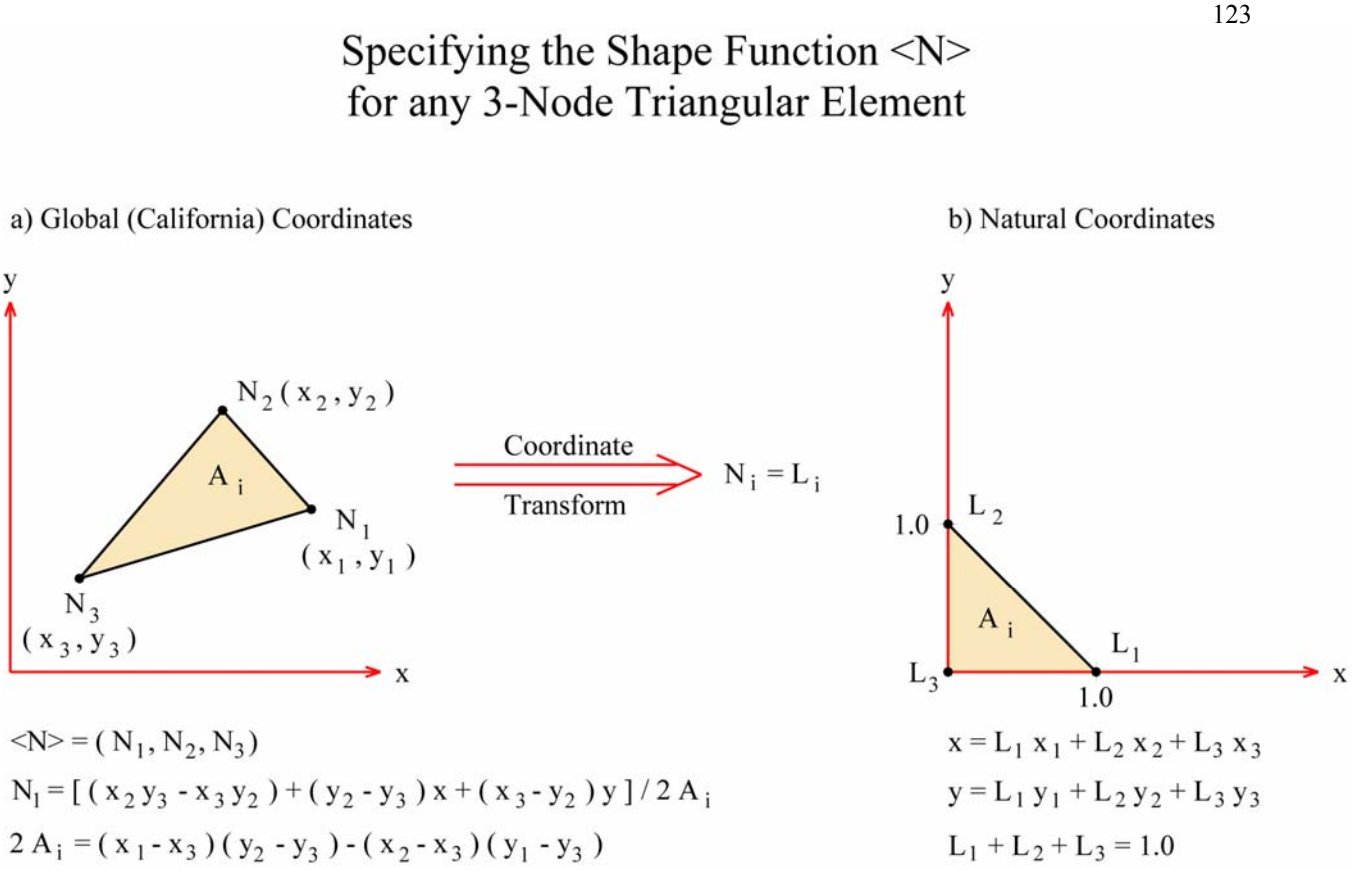

Figure 47: Bedrock shape function polynomial and transform to natural coordinates for a generalized 3-node triangular element in the cross shore bedrock plane (see Figure 45).

computations of the weighted residuals leads to a series of influence coefficient matrices defined

$$
\begin{aligned}
a_{ij} &= \frac{1}{A_i}\iint N_i N_j dA \\
s_{ij} &= \frac{1}{A_i}\iint N_i \frac{\partial N_j}{\partial x} dA \\
t_{ij} &= \frac{1}{A_i}\iint N_i \frac{\partial N_j}{\partial y} dA \\
g_{ijk} &= \frac{1}{A_i}\iint N_i N_j \frac{\partial N_k}{\partial x} dA \\
h_{ijk} &= \frac{1}{A_i}\iint N_i N_j \frac{\partial N_k}{\partial y} dA
\end{aligned}
\tag{72}
$$

The influence coefficient matrices given by equation (72) are evaluated in both global and natural coordinates. Once the influence coefficients have been calculated for each 3-node element in the bedrock plane, the weighted residuals reduce to a set of order-one ordinary differential with constant coefficients. The bedrock mass continuity equation for the ith element in the bedrock plane becomes:

$$
\begin{aligned}
\sum\left(a_{ij}\frac{dH_i}{dt}\right) &= -\sum_i\sum_k\left[g_{ijk}\left(H_i q_{xk} + H_k q_{xi}\right) + h_{ijk}\left(H_i q_{yk} + H_k q_{yi}\right)\right] \\
\sum\left(a_{ij}\frac{dq_{xj}}{dt}\right) &= -\sum_j\sum_k\left[g_{ijk}\left(q_{xk} q_{xj}\right) + h_{ijk}\left(q_{yj} q_{xk}\right)\right] + N_i\sum_j N_j S_{fj} + g\sum_i s_{ij} H_i \\
\sum\left(a_{ij}\frac{dq_{yj}}{dt}\right) &= -\sum_j\sum_k\left[g_{ijk}\left(q_{xj} q_{yk}\right) + h_{ijk}\left(q_{yj} q_{xk}\right)\right] + N_i\sum_j N_j S_{fj} + g\sum_i t_{ij} H_i
\end{aligned}
\tag{73}
$$

Equations (73) are essentially simple strain equations forced by the collection of algebraic terms appearing on the right hand side; and are therefore easily integrated over time. The time integration scheme used over each time step of the bedrock

cutting simulation is based upon the ***trapezoidal rule***, see Gallagher (1981) or Conte and deBoor (1972). This scheme was chosen because it is known to be unconditionally stable. It replaces time derivatives between two successive times, $\Delta t = t_{n+1} - t_n$, with a truncated Taylor series. For the bedrock recession in (1) it would take on the form:

$$\frac{dR}{dt} = \xi(t) = \frac{\rho}{\rho_s} f_e(t) E(t) Cn(t)$$
$$R_{n+1} - R_n = \frac{\Delta t}{2}\left(\xi_{n+1} + \xi_n\right) + \Psi \Delta t \qquad (74)$$
$$\Psi = \frac{1}{12}(\Delta t)^2 \left|\frac{d^2\xi}{dt^2}\right|$$

To solve equation (74), iteration is required involving successive forward and backward substitutions.

3.5 Bedrock Cutting Codes for Wave-Cut Platforms and Seacliffs.

The recession function *R* in (1) and (74) is computed by the **bedrock_cutting-3.for** codes in Appendix-L. The computations are made in cross-shore bedrock planes taken from the GIS shape files for the bedrock surface (**subbot20.txt).** The input parameters output files which are required by **bedrock_cutting-3.for** are:

tp_subbot20.txt……*ifile1 gis elevation file (including 6 lines of header)
dp_80-00.dat …… *ifile2 cdip proxy wave file height, per, dir, file
50149…… *nlines number of time steps
tp_subbot50_xyz.txt …… *ofile1 extracted xyz file
tp_subbot50_grd.txt ……*ofile2 gridded z values (eliminate excess -9999)

s2_subbot50_grd.txt ……*ofile3 gridded z values (eliminate excess -9999)

241 …… *ncols node number elevation

665 …… *nrows node number cross-shore position

464474.53 …… *xllcorner California coordinate

3628298.25…… *yllcorner California coordinate

20.0 …… *cellsize element resolution

-9999 …… *NODATA

6 …… *ixst number of column to start xyz

241 …… *ixnd number of column to end xyz

118 …… *iyst number of row to start xyz

558 …… *iynd number of row to end xyz

0.01 …… *slrate sealevel rise rate

10.0 …… *depcrit seaward depth limit of exposed bedrock

10.0 …… *iloop number of times cdip wave record is looped

1.0 …… *akb abrasion factor Ka

0.01 …… *tanbeta slope of bedrock at seaward limit of exposure

274 …… *jstart starting plane

354 …… *jstop stopping plane

2.0 …… *akshale notching factor Kn

The bedrock cutting algorithms operate on the exposed portion of bedrock surface computed by the **cn_scour_osc.for** codes. These algorithms proceed in successive forward and backward substitutions in time while stepping through the cdip proxy wave record that is looped over and over again for as many cycles as prescribed by the **iloop** input parameter. The recession function ***R*** in (1) and (74) is

plotted in Figure 48b, showing the time stepped progressive retreat of the bedrock surface at 0 m MSL as computed by the **cn_scour_osc.for** and **bedrock_cutting-3.for** codes for one pass through the CDIP proxy wave record in Figure 48a. This simulation uses the disequilibrium profile from TP 470 in Figure 46 as the initial condition; and then runs the CDIP proxy wave progression 20 years forward from that point in time, representing a simulation of 64.4 years in total duration. It is interesting to note that singular, short lived events of high waves (as occurred during January 1988) do not produce significant abrasion and recession of the bedrock surface. This is due to the fact that short lived extreme event waves do not persist long enough for the relatively slow abrasion processes to produce a large cumulative effect on the bedrock surface. Instead, the preponderance of bedrock recession occurs during protracted periods of intermediate high waves, that are large enough to denude the sediment cover and persistent enough to produce significant cumulative recession. The most notable period of these types of waves was 1983. Altogether, the bedrock recession rate averages $\boldsymbol{R}$=8 cm/yr during a 20 year period of denuded sediment cover over the inner shorezone.

When the CDIP proxy wave record is looped 200 times continuously across the Torrey Pines Sub-Cell, a dramatic widening of the wave-cut platform above 5m depth (on the order of 160 meters) is simulated by the **cn_scour_osc.for** and **bedrock_cutting-3.for** codes as shown in Figure 49b. To add realism to this simulation, the empirical Ka factor in (2) was increased by an order of magnitude for the portion of the Torrey Pines Sub-cell that lies south of Bathtub Rock (located in the upper portion of Figure 49b). This alongshore variation in erodibility was introduced into the model through the input parameter **akb** in the

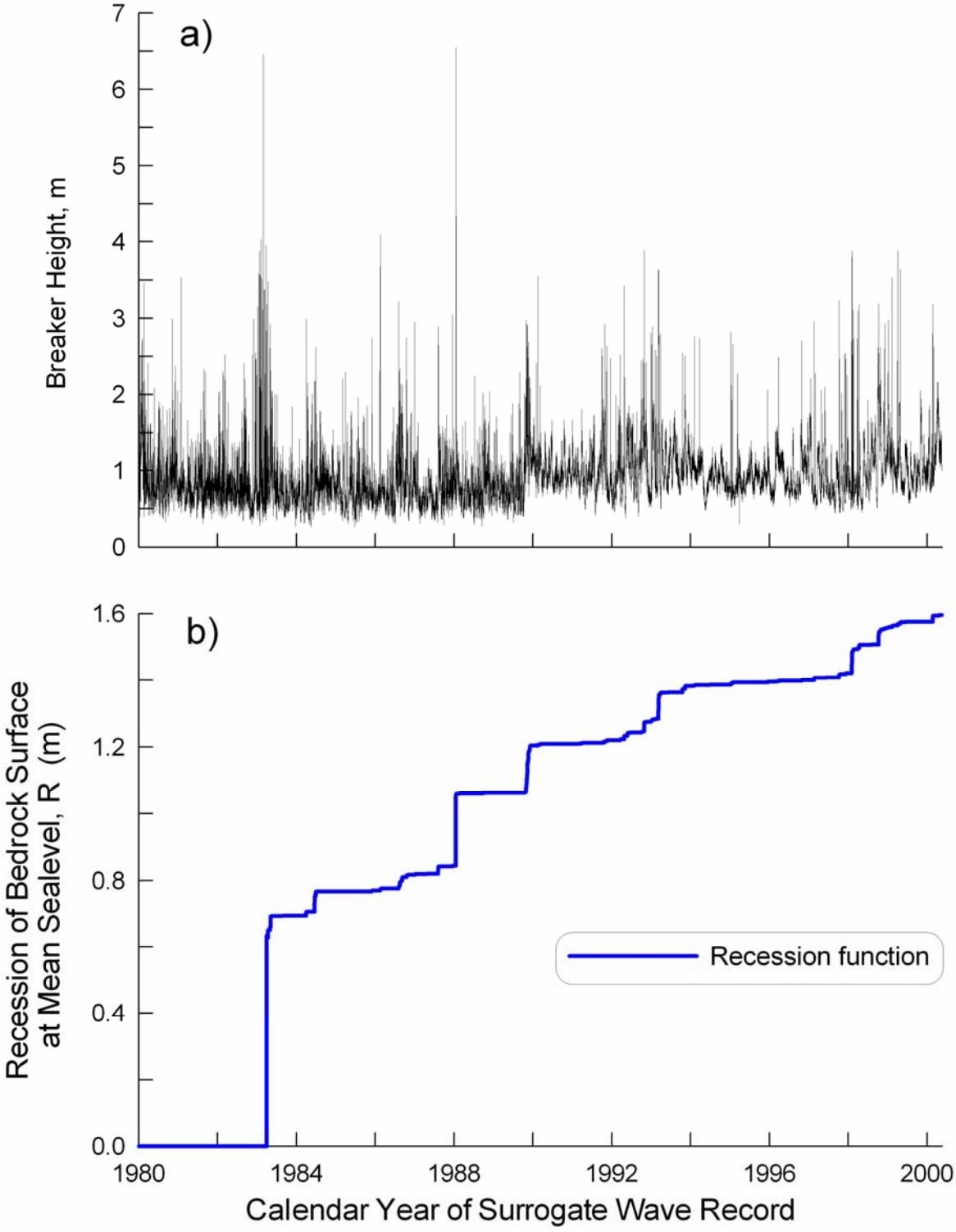

Figure 48. Recession of bedrock surface at mean sealevel on a 2% shelf slope at constant sea level, a) breaker height: 1980-2000, Torrey Pines Sub-Cell, b) recession function, R(t), positive values indicate landward shift.

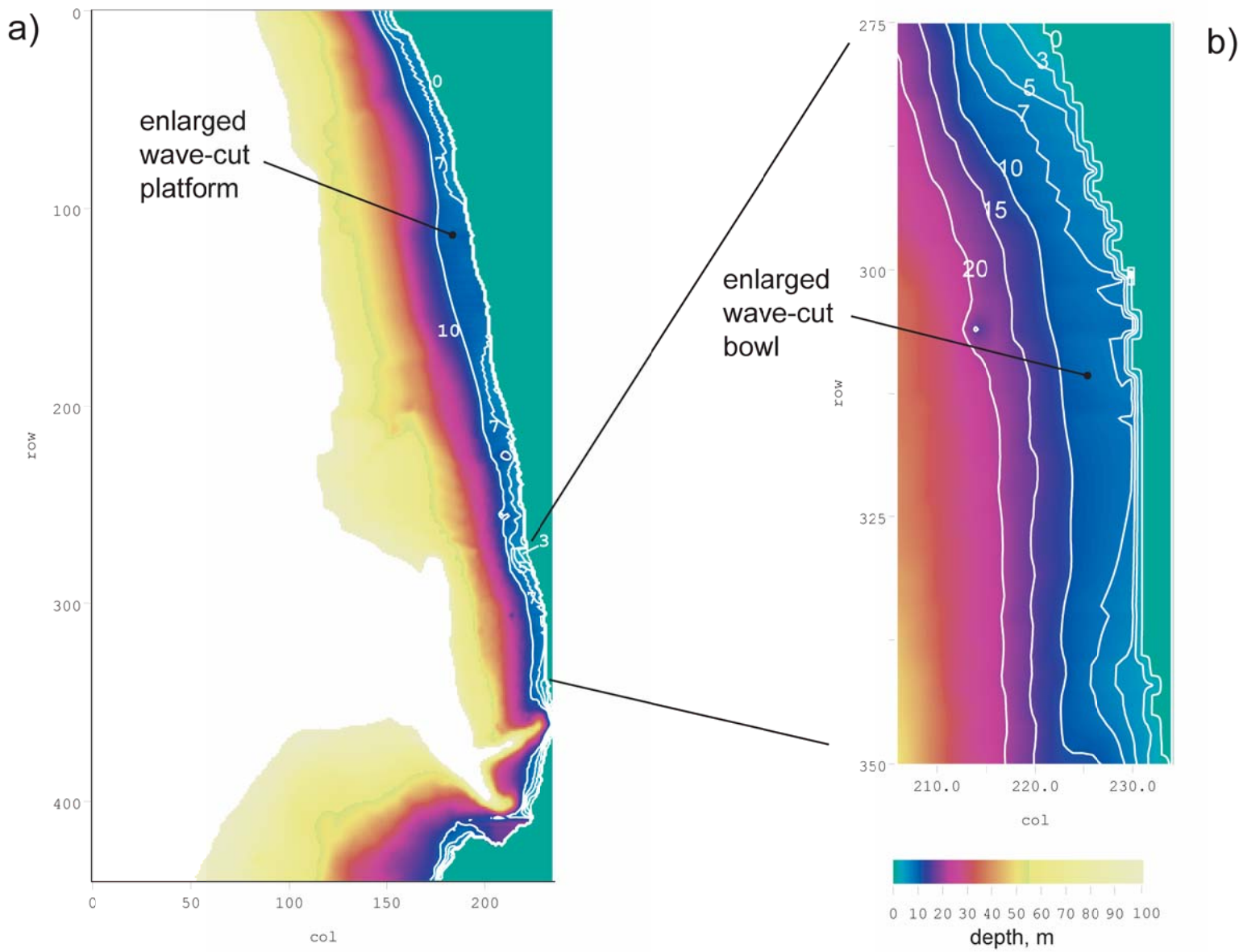

Figure 49: Subbottom shelf bathymetry of Torrey Pines Subcell a) BCM modeled condition for 2000 years in the future based on constant sea level and uniform erosion resistant bedrock (Td) north of Bathtub Rock and friable bedrock (Tt) south of Bathtub Rock. b) enlargement of friable bedrock region.

bedrock_cutting-3.for code, and was done to reflect the transition between the erosion resistant Del Mar formation (Td) to the north of Bathtub Rock and the friable Ardath Shale and Torrey Sandstone (Tt) to the south. As a consequence of the along shore variation in **akb**, the **cn_scour_osc.for** and **bedrock_cutting-3.for** codes produced a 160 meter wide bowl in the inner shorezone at depths between mean sea level and -10m south of Bathtub Rock during this 2000 year long simulation that allowed no new river sediment input into the littoral system (J=0). Interestingly enough, a similar bowl is found in the sub bottom at the same location

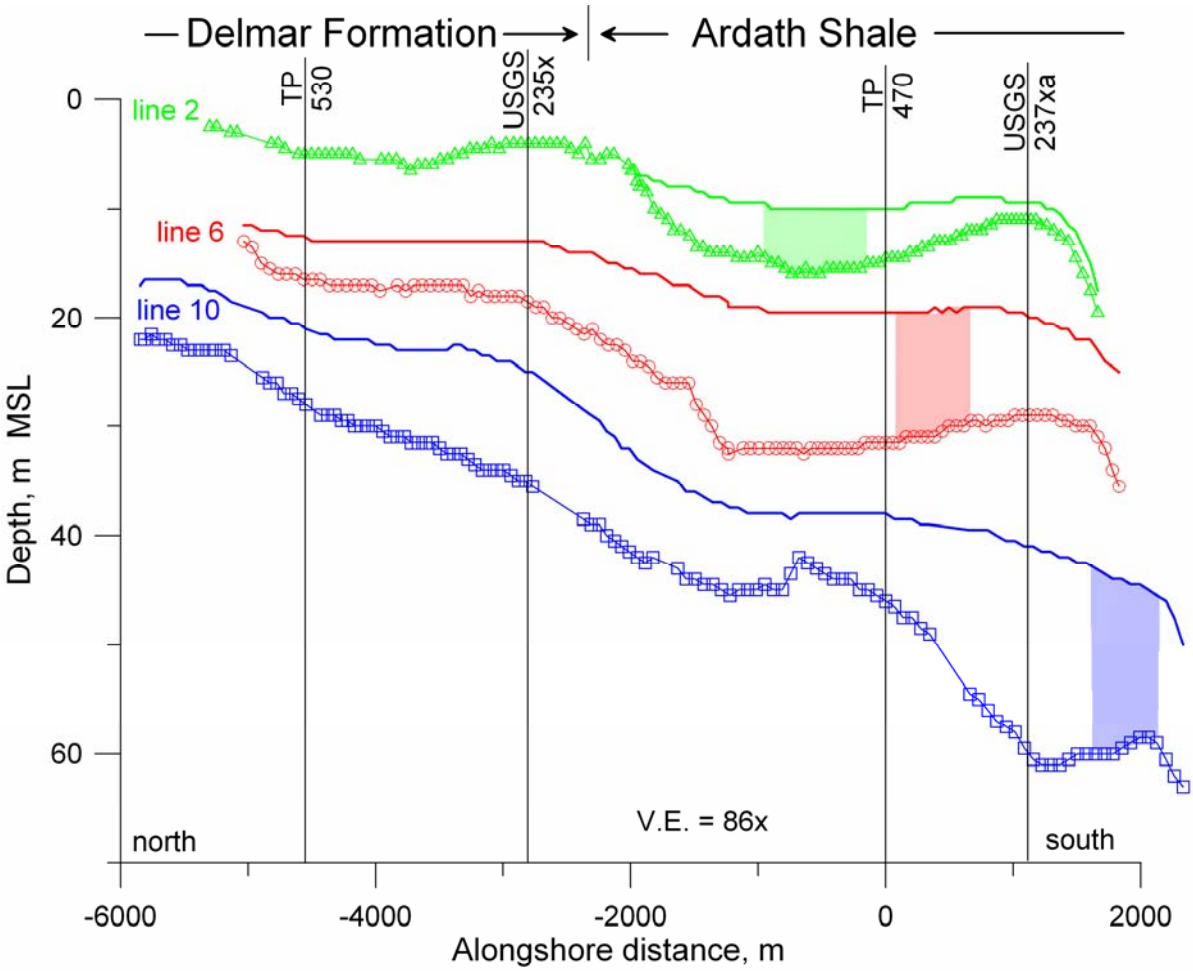

Figure 50. Bathymetry (line) and subbottom (open symbol) sections along shore-parallel seismic lines 2, 6, 10.

in the 20-40m depth range (Figure 50) that was formed during the 1200 year long still stand of the 8.2ka cold event (see Figure 4).

The effect which the rate of sea level change can have on bedrock cutting can be studied by adjusting the input parameter **slrate** in the **bedrock_cutting-3.for** codes. A sensitivity analysis was done sweeping the parameter space of **slrate** while the CDIP proxy wave record was looped 450 times. Figure 51 shows the results of that sensitivity analysis for rates of sealevel change that varied between $0\,cm/century \le d\eta/dt \le 400\,cm/century$. With the empirical friability factor in (2) set for f_e = 1.2 x 10^{-7} m/N at a threshold wave height H = 2m, the recession rate reduces to an analytic approximation:

$$\frac{dR}{dt} \cong \frac{dx}{dt} \cong 1700 \frac{\left\{2\left[1-\left(0.002\frac{d\eta}{dt}\right)^{0.2}\right]\right\}}{\left[3-\left(0.002\frac{d\eta}{dt}\right)^{2}\right]} \qquad (75)$$

As shown in Figure 51a, the rate of bedrock recession declines as the rate of sealevel rise increases, with a recession rate at still stand ($d\eta/dt = 0$) of about dR/dt =840 cm/century, or about 1.68 meters ever 20 years, commensurate with the result in Figure 48. Recession rates for bedrock decline with increasing rate of sealevel rise because bedrock cutting is limited to depths above 5m by the depth decay of oscillatory wave motion from the second and third lines of the bedrock continuity equation (73). With rapid sealevel rise, the depth limited cutting zone remains over a given cross section of bed rock for a relatively brief period, thereby diminishing the cumulative recession over time.

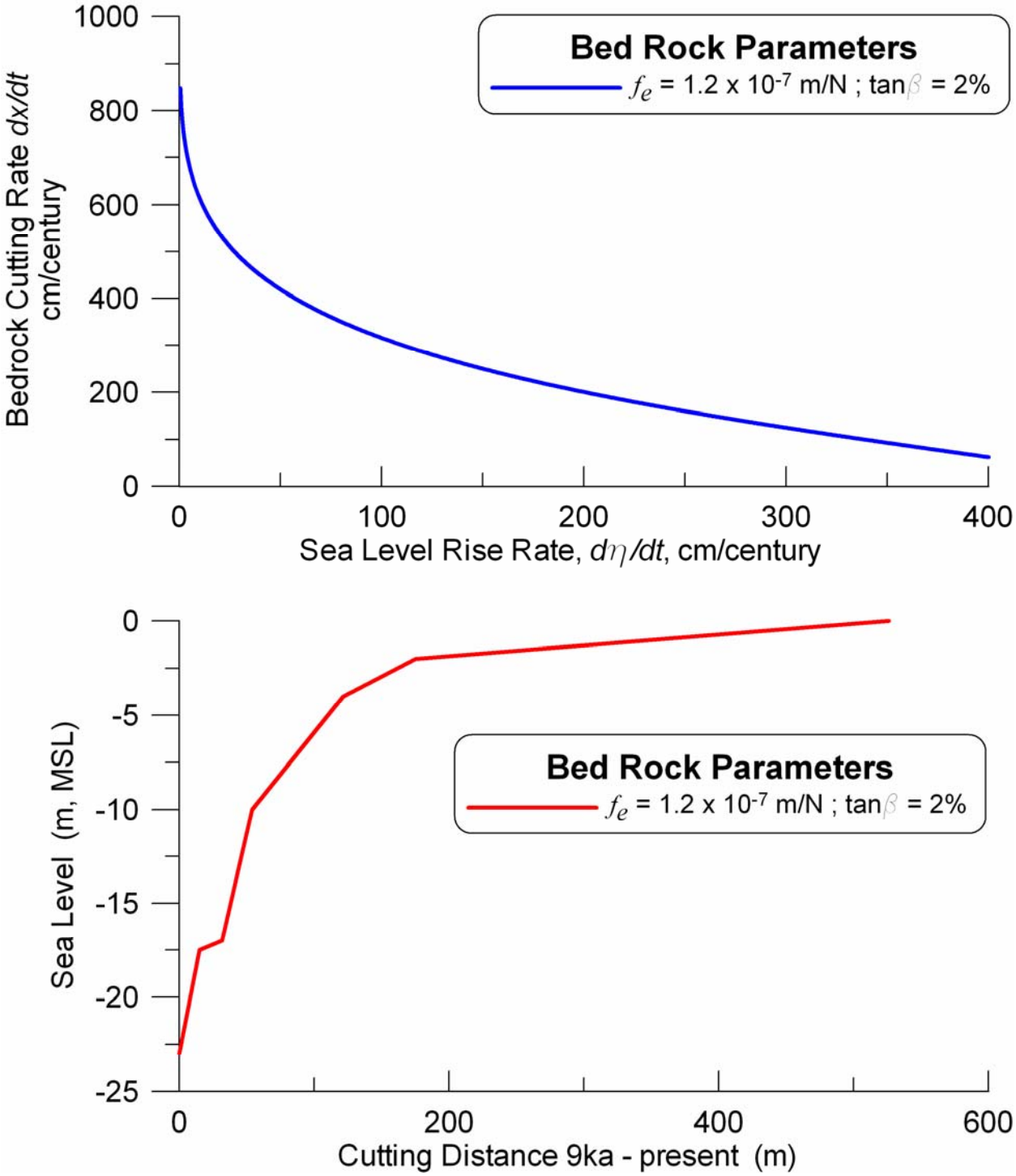

Figure 51: Effects of rate of sealevel rise on bedrock recession. a) recession rate as a function of rate of rise of sea level; and b) Cumulative recession 9ka to present obtained by applying recession rate function (75) to sea level function in Figure 4.

When the recession rate function in Figure51a is applied continuously to the sealevel function in Figure 4, (by coupling **bedrock_cutting-3.for** to **sea_level_waz.for** through the **slrate** parameter), we obtain a vertical distribution of the horizontal increment of bedrock surface that is abraded from the native bedrock plane over the last nine thousand years (Figure 51b). This result shows 350 meters of recession in the last five thousand years, corresponding roughly to the average width of the modern wave cut platform appearing at depths less than 5 m in the Torrey Pines Subcell. However, we also find about 25 meters of incremental recession at about 18 m depth corresponding to the brief still stand of the 8.2 ka cold event. These favorable comparisons to features apparent in the sub-bottom map of the Torrey Pines Subcell (Figures 42 and 50), indicate that assumptions of empirical factors in **bedrock_cutting-3.inp** are appropriate.

To deal with the compound bedrock cutting problem that arises at the intersection of the wave-cut platform and sea cliff, we invoke the notching algorithms (3) and (4) and specialized shape file logic found in the **cliffing_model_4_leg1-4a.for** family of codes of APPENDIX-M. These codes are prescribed for a variety of sealevel scenarios. The **cliffing_model_4_leg1a.for** code was developed for bedrock cutting on sea cliff faces during sea level transgressions only. The **cliffing_model_4_leg2b.for** code was formulated for bedrock cutting on sea cliff faces during still stands that follow sea level transgressions. The **cliffing_model_4_leg2c.for** code is for bedrock cutting on sea cliff faces during still stands that follow sea level transgressions. The **cliffing_model_4_leg2d.for** code computes bedrock cutting on sea cliff faces for sea level transgressions that follow still stands. The **cliffing_model_4_leg3a.for** code computes bedrock cutting on sea cliff faces for sea level regressions that follow still stands. The input files for these codes are nearly identical except for

input file naming protocol designed to differentiate the various sealevel scenarios. The common input file format for the **cliffing_model_4_leg1-4a.for** family of codes is:

dp_80-00.dat…….*ifile1 Torrey Pines breaker file from CDIP proxy

50149 ……. *nlines # of time steps in proxy wave record

1980.0 ……. *tcon=1980 for CDIP wave data file

0.0 ……. *vcon river sediment input

340.0 ……. *winu north wave window

140.0 ……. *winl south wave window

270.0 ……. *cdir direction of bedrock plane

0.00085 ……. *effic Kn knothcing efficiency

0 ……. *jetty switch for jetty structure (0=none)

0.00058 ……. *beach1 initial erodibilty of bedrock

1.8 ……. *steep tangent of revetment slope

0.57 ……. *ret fraction of talus that is beach grade sand

56.0 ……. *bozspl horizontal datum of bench mark

0.0 ……. *axbwid user specified profile offset

0.23 …….*bfac spreading factor of talus retained as basal conglomerate

0.01 ……. *akamp Ka abrasion efficiency factor

0.0 ……. *dredge dredge volume input

6regr_lg2d_1.dat ……. *ofile1 t_tot,slop output file, bedrock slope

6regr_lg2d_2.dat ……*ofile2 x0,y0 output file, initial bedrock profile

6regr_lg2d_3.dat ……..*ofile3 x1,y1 output file, final bedrock profile below sealevel

6regr_lg2d_4.dat ……. *ofile4 x1n,y1n output file, final bedrock profile above sealevel

6regr_lg2d_5.dat ……. *ofile5 x1n,t_tot output file, sediment flux profile from eroded bedrock

6regr_lg2d_6.dat ……. *ofile6 output file, time(n),slop(n) 1st 20 years

200.0 ……. *wh_thr threshold breaker height (cm)

0.7 ……. *sh_amp gamma factor, Hunt's formula

.53 ……. *a_shore Ka notching efficiency factor

1.0 …… *dirmut wave directional factor (1.0= from oceanrds breaker file)

0.00001 ……. *beach2 initial erodibilty with jetty

1984.6 ……. *bchtim first time marker

0.000112 ……. *beach3 initial erodibility with revetment

1985.5 ……. *bchtim2 second time marker

970.0 ……. *wh_thr2 max breaker height trhshold

0.4 ……. *beach4 initial erodibility of bluff toe

1.0 ……. *akt time compression factor (1.0 gives CDIP proxy record)

1982.9 ……. *tim_dir third time marker

1.0 ……. *fix time offset (1.0 gives CDIP proxy record)

0 ……. *i_rev 1=with revetment, 0=no revetment

1983.36 ……. *clf_tim forth time marker

0.0 ……. *bch_clf user specified bluff offset

1992.5 ……. *bchtim3 fith time marker

0.000108 ……. *beach5 initial erodibilty of bluff face

1983.247 ……. *tslop1 bottom slope re set time

1983.25 ……. *tslop2 top slope re set time

0.15 ……. *akslop initial cliff top slope

91 ……. *iloop number of times CDIP wave record looped

0.01 ……. *sl_rate sealevel rate of change(cm/yr)

3.4 ……. *wv_rate (controls slope of initial terrace cut bigger=flatter)

0.02 ……. *beta (initial shelf slope)

0.7 ……. *slump1 (controls onset of terrace rise, bigger=wider)

24.0 ……*slump2 (controls slope of terrace toe, bigger=wider and rounder)

0.02 ……. *bthresh initial threshold slope

1373.140 ……. *x0_st starting position in cross shore, m

85628 ……. *y0_st starting position in longshore, m

250.003 ……*x1_st starting position in cross shore m of initial cliff toe, m

-85628 ……*y1_st starting position in cross shore m of initial cliff toe, m

1 ……. *icrest *1=round bluff top, 0=bluff top intersects slope

10.0 ……*rknol (controls slope of top of bluff face, small=vertical big=sloping

1.09 ……. *acut2 factor controlling wave abrasion of bluff face

0 ……. *ireg (0=runs to the end, 1=runs to xstop)

250.0 …… *xstop used in ireg=1, xstop = rshift from cliffing_model_4_leg1a

-55.0 ……. *z_start starting depth for initial sealevel sweeps

0.02 ……. *alpha (controls slope of initial terrace cut smaller=flatter)

0.020 ……. *bubba controls slop of bottom of terrace face

The **cliffing_model_4_leg1-4a.for** family of codes output the initial and final bedrock profiles, as well as the cross shore distribution of sediment flux that recharges each control cell from bluff erosion talus. The parameter **ret** specifies the fraction of eroded bluff volume that is beach grade sand and contributes to the recharge sediment flux. The parameter (1.0-**ret**) specifies the fraction of eroded bluff volume that becomes basal conglomerate and is added to the bedrock profile

and proportional distributed cross shore by the spreading parameter **bfac**. to the recharge sediment flux. The **cliffing_model_4_leg1-4a.for** family of codes also provide allowances for user specified shore protection including jetties and revetments. These features are activated by the integer switches **jetty** and **rev** that interdict in the bluff erosion calculations according to assumed reductions in erodibility as specified by the parameters, **beach2** and **beach3**. The **cliffing_model_4_leg1-4a.for** family of codes utilize a number of empirical parameters that are used to produce realistic cliff morphology (eg, rounding at the toe and crest) from the numerical simulations. A great deal of trial and error went into the specification of such parameters above, and we recommend that the user treat them as "hard-wired".

To demonstrate the bluff and terrace morphologies that can be simulated with the **cliffing_model_4_leg1-4a.for** family of codes, a series of sealevel transgressions and regressions were modeled in Figure 52 acting on a shelf rise bedrock slope (**beta**) of 2%. This simulation involved 3 still stands occurring between 90 ka and 84 ka (Figure 53) that produced a series of terraces in the sub bottom known as the "5a terraces". The simulation in Figure 52 begins with the 5a transgression 94 thousand years before present during which sea level rose at a rate of about 110 cm/century until stopping at a brief still stand of about a thousand years at 90ka. Following this still stand, there was a slight recession to another brief still stand 86ka, (Figure 53), followed by a rapid transgression to a third, higher still 84 ka. The combined action of these three still stands acting in close proximity to one another and persisting for about 16 thousand years, cut a large, complex platform and terrace system in our simulation indicated by the blue line in Figure 52. The stillstand/regression sequence that occurred between 90 ka and 86 ka produced an initial bluff and terrace cut in the 2% bedrock slope that was

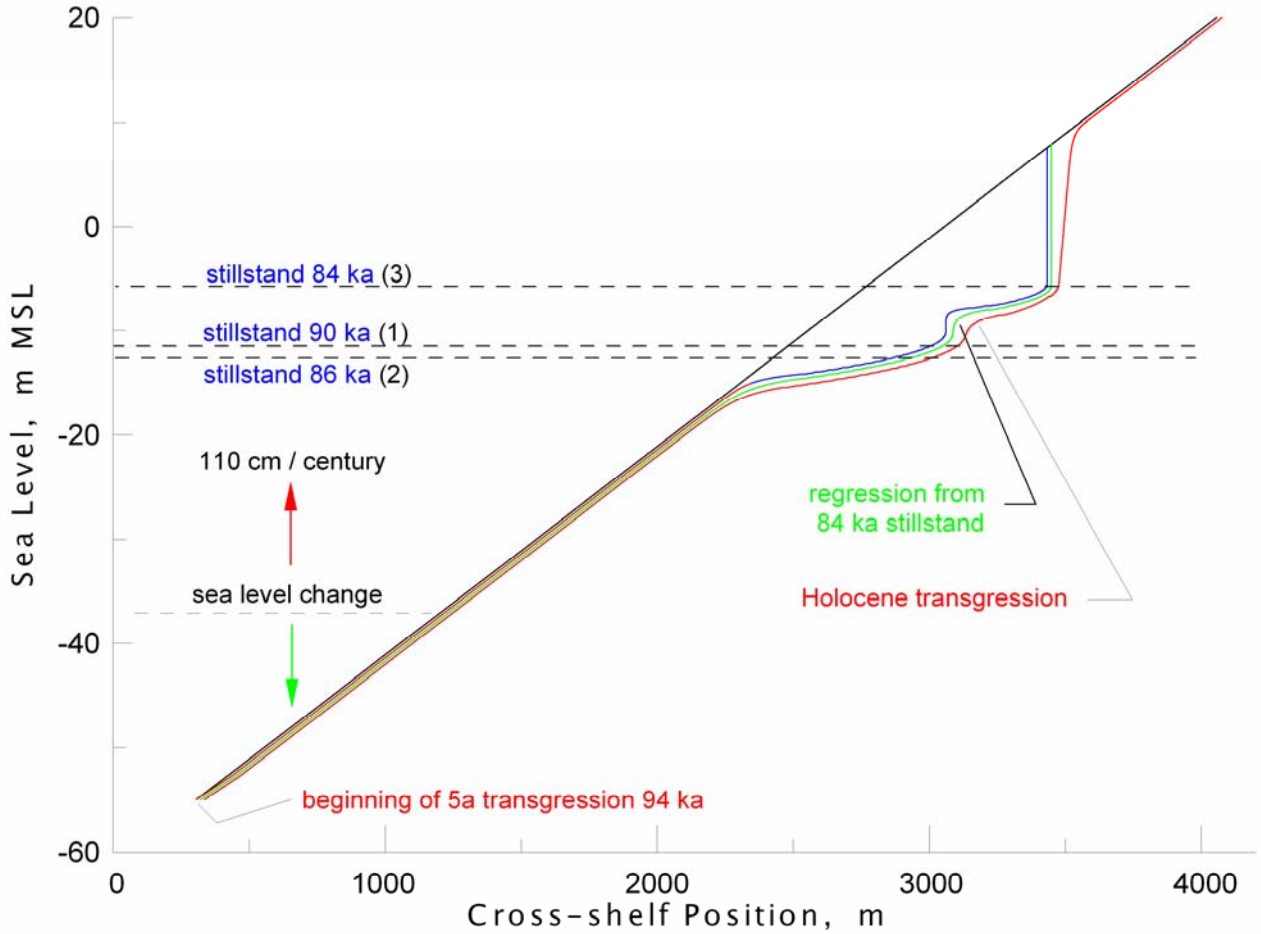

Figure 52. Simulation of MIS 5a terraces with Bedrock Cutting Model (BCM) showing change in initial 2% shelf slope (black) due to wave cutting during a transgression/triple stillstand sequence (red and blue), followed by a regression/transgression cycle (green/red).

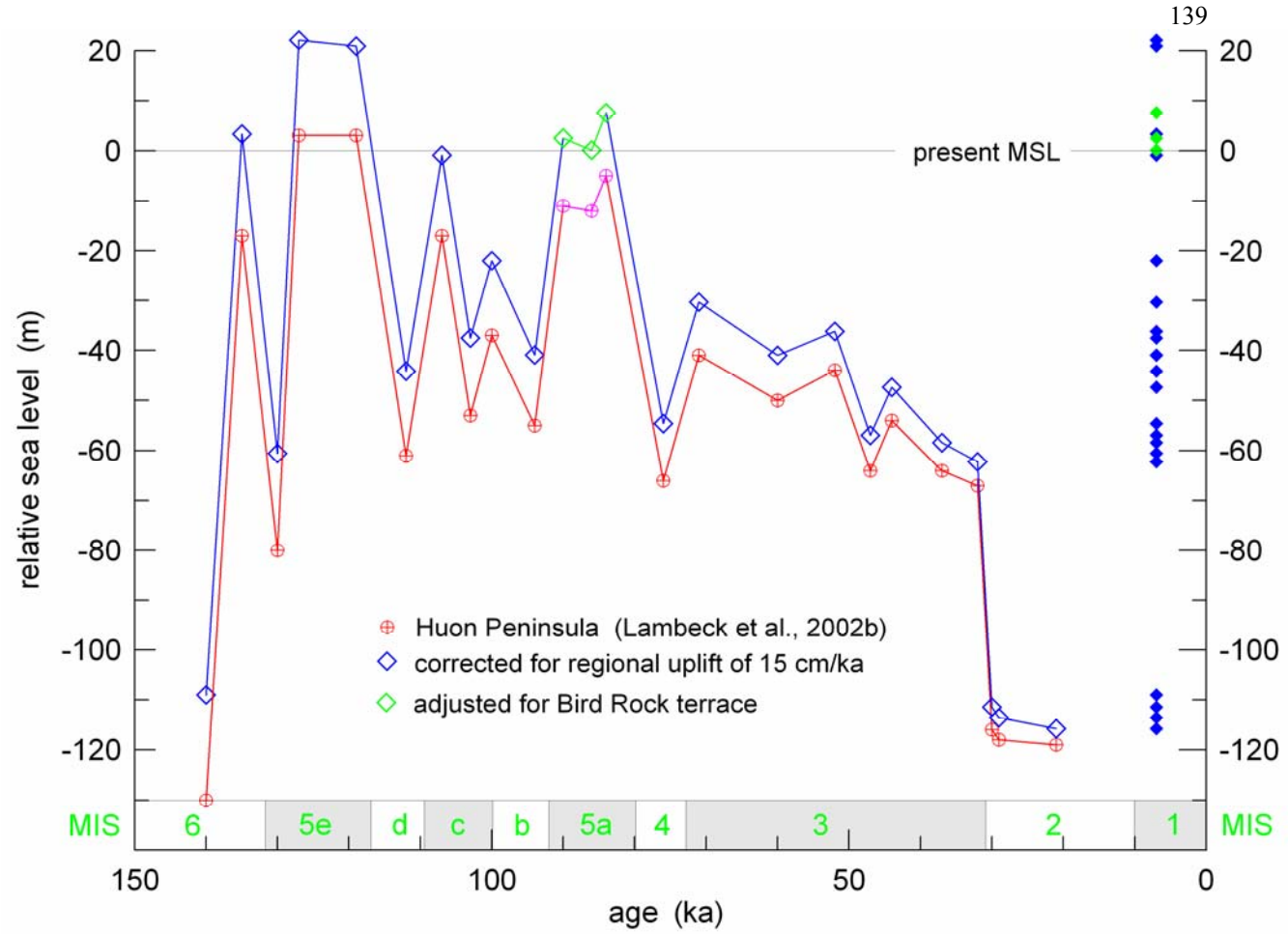

Figure 53. Relative high- and lowstands of sea level (⊕) from the Huon Peninsula (Lambeck, 2002b) and adjusted to Bird Rock terrace elevation, as a proxy for a Southern California Bight sea level curve during the Wisconsinan regressions. Present elevations (◇) where terracing may occur on the shelf of the Oceanside Littoral Cell, corrected for regional uplift of 15 cm/ka (see text). Cumulative effects of expected terracing projected to the right margin (◆).

subsequently planed off by the 90-86 ka transgression, leaving the distinctive bench in the otherwise broad platform. This demonstrates how sequences of sealevel transgressions, still stands and regressions can lead to complexes of terraces like those found in the subbottom record at the northern end of the Oceanside Littoral Cell in Figure 54. While the dimensions of these terraces are in rough agreement with those of the blue-line simulation in Figure 52, the observed terraces in Figure 54 have more rounded features. The resolution of this discrepancy is provided by the multiple excursions sealevel has exhibited since the 5a terraces were cut. Following the 84 ka still stand sea level was lowered by a deep glacial period that produced a protracted regression (Figure 53). The regression from the 84 ka still stand allowed the depth limited bedrock cutting zone to rapidly run back over all the terrace features generated by the 90-84 ka series of still stands, producing the green profile shown in Figure 52. We note how this rapid regression produced more rounding of the features in the 5a terrace complex as shown by the green profile. Sealevel recovered from this regression and entered into the Holocene transgression, whence sealevel rose back up and over the 5a terraces. In the model simulation shown by the red profile in Figure 52, the Holocene transgression produced additional rounding of the 5a terrace complex, nearly obliterating the relict bench left by the 90 ka still stand. Hence, increasing the amount of paleo history input to the model improves the fidelity of model simulations relative to observations of ancient terraces like those found in the subbottom record (ala, Figure 54). We take this as an indication that the BCM physics appear sound and that the model is relatively well calibrated. With this calibration, we proceed into forecasts of the fully integrated CEM.

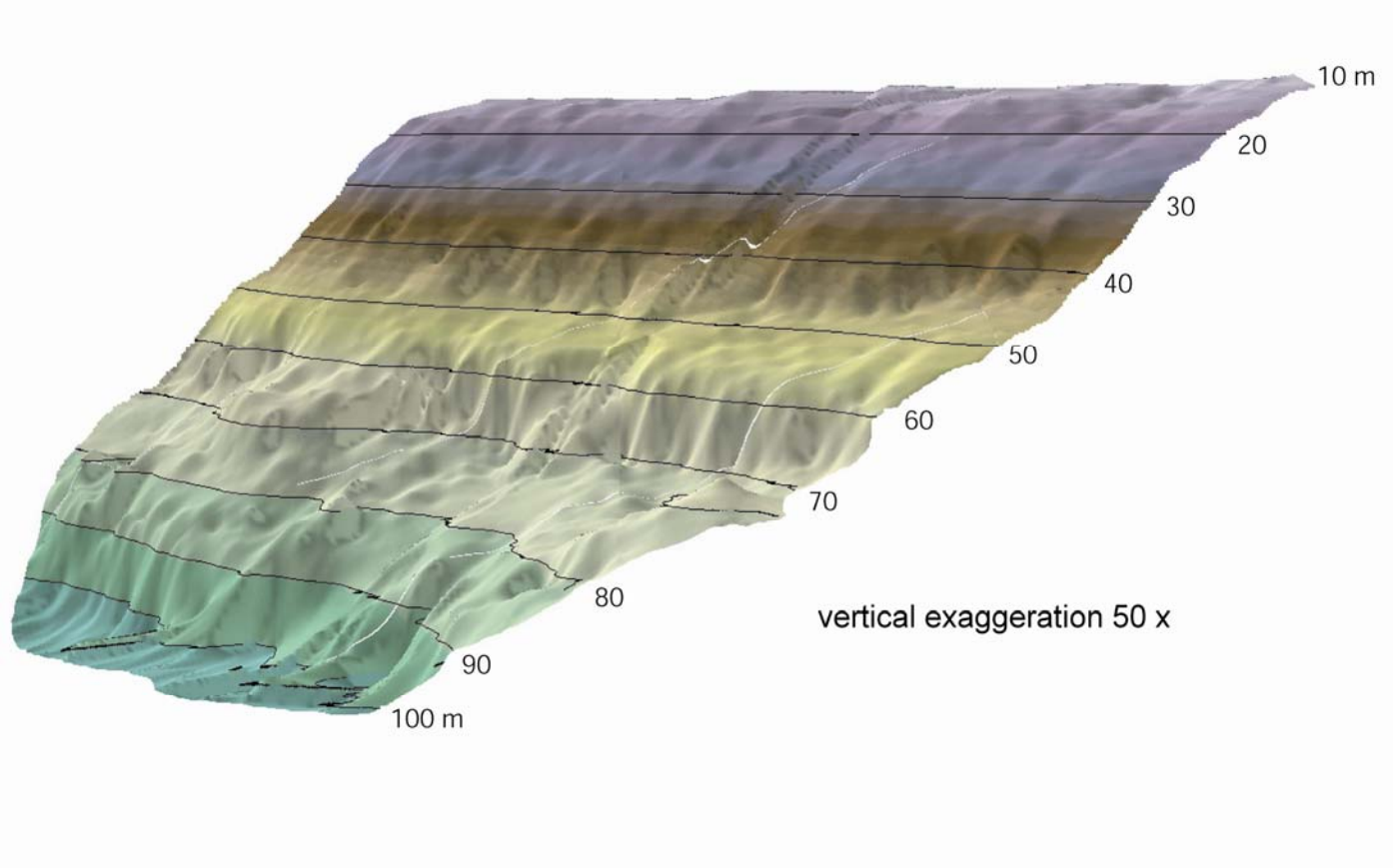

Figure 54: Subbottom surface off San Onofre , CA showing multiple terraces cut in bedrock near the -50m and -80m MSL elevation contours (data from R.L. Kolpack (ed) 1991).

4. Coastal Evolution Model (CEM) Integration and Code Documentation

The Coastal Evolution Model represents a coupled set of LCM and BCM with 3-dimensional graphics capability. The LCM and BCM codes detailed in Sections 2 and 3 are coupled in fully 3-dimensional solutions to (5) by the **CEM_sedxport3.for** code. This code is used to render 3-dimensional forecasts of the coastal evolution within the Torrey Pines Sub-Cell 200 years into the future, and to study how diminished sediment influx into the Oceanside Cell from dam building (Figure 5) may affect the coastal morphology of this region in the future.

4.1 Coastal Evolution Model (CEM) Code Detail

The **CEM_sedxport3.for** code is a time stepped finite element model which solves the advection-diffusion equations (5)-(8) over a fully configurable 3-dimensional grid. The vertical dimension is treated as a two-layer ocean, with a surface mixed layer and a bottom layer separated by a pycnocline interface. The code accepts any arbitrary density and velocity contrast between the mixed layer and bottom layer that satisfies the Richardson number stability criteria and composite Froude number condition of hydraulic state.

The river source initializations for sediment input are handled by a subroutines called **RIVXPORT** and are augmented by local source input from erosion and bedrock cutting by the subroutines **BOTXPORT** and **SURXPORT.** The subroutine **BOTXPORT** derives its local source input by coupling with the **cn_scour_osc.for** and **bedrock_cutting-3.for** codes while the source coupling for **SURXPORT** is the **cliffing_model_4_leg1-4a.for** family of codes. The **CEM_sedxport3.for** codes time split advection and diffusion calculations between decadal scales from **cn_scour_osc.for** source coupling, and millennial scales for **bedrock_cutting-3.for** and **cliffing_model_4_leg1-4a.for** source coupling (Figure

1). The **CEM_sedxport3.for** codes will compute advective field effects arising from spatial gradients in eddy diffusivity, i.e., the so-called "gradient eddy diffusivity velocities" after Armi (1979). Eddy mass diffusivities are calculated from momentum diffusivities by means of a series of Peclet number corrections for the surface and bottom boundary layers derived from the work of Stommel (1949) with modifications after Nielsen (1979), Jensen and Carlson (1976), and Jenkins and Wasyl (1990). Peclet number correction for the wind-induced mixed layer diffusivities are calculated from algorithms developed by Martin and Meiburg (1994), while Peclet number corrections to the interfacial shear at the pycnocline are derived from Lazara and Lasheras (1992a;1992b). The momentum diffusivities to which these Peclet number corrections are applied are due to Thorade (1914), Schmidt (1917), Durst (1924), and Newman (1952) for the wind-induced mixed layer turbulence and to Stommel (1949) and List, et al. (1990) for the current-induced turbulence. The primitive equations for the **CEM_sedxport3.for** codes may be found in APPENDIX-N.

CEM_sedxport3.for has been built in a modular computational architecture with a set of subroutines divided into two major clusters: 1) those which prescribe hydrodynamic forcing functions; and, 2) those which prescribe the mass sources acted upon by the hydrodynamic forcing to produce dispersion and transport. The cluster of modules for hydrodynamic forcing ultimately prescribes the velocities and diffusivities induced by wind, waves, and tidal flow for each depth increment at each node in the grid network. The subroutines **RIVXPORT** and **BOTXPORT-** solve for the mixing and advection of the negatively buoyant sediment suspension in response to the wave transport using an rms vorticity-based time splitting scheme. Both **BOTXPORT** and **RIVXPORT** solve the eddy gradient form of (5).

The eddy diffusivity, ε, in (5) controls the strength of mixing and dilution of the concentrated seawater and flood water constituents, and varies with position in the water column relative to the pycnocline interface. Vertical mixing includes two mixing mechanisms at depths above and below the pycnocline: 1) fossil turbulence from the bottom boundary layer, and 2) wind mixing in the surface mixed layer. The pycnocline depth is treated as a zone of hindered mixing and varies in response to the wind speed and duration. Below the pycnocline, only turbulence from the bottom wave/current boundary layer contributes to the local diffusivity. Nearshore, breaking wave activity also contributes to mixing. The surf zone is treated as a line source of turbulent kinetic energy by the subroutine **SURXPORT**. This subroutine calculates seaward mixing from fossil surf zone turbulence, and seaward advection from rip currents embedded in the line source. Both the eddy diffusivity of the line source and the strength and position of the embedded rip currents are computed from the shoaling wave parameters evaluated at the breakpoint, as throughput from **oceanrds_socal.for** and **oceanrds_tp.for** in the LCM (Figure 1).

The input parameters output files which are required by **CEM_sedxport3.for** codes are:

TorreyPines……. * site name 8 characters (name)
200……. * number of points in grid (nx)
200 ……. * number of points in grid (ny)
80 ……. * x column number of selected grid point, 1-200 W-E (igrdx)
100 ……. * y row number of selected grid point, 1-200 S-N (igrdy)
77.5……. * x dimension meters of grid cell spacing (sx)
92.6 ……. * y dimension meters of grid cell spacing (sy)

12.0 ……. * swell wave period sec (persw)

8.0 ……. * wind wave period sec (perwin)

0.470916……. * swell wave height in meters (hsw)

0.352958……. * wind wave height in meters (hwin)

.03 ……. * beach slope (tanbeta)

.78 ……. * suspended load efficiency (aks)

.01 ……. * beach packing parameter (akb)

0.001……. * upper layer mixing length coefficient (ak2)

1.68 ……. * total bottom sediment concentration g/cc (rci)

1.69 ……. * beach bulk density (rszi)

0.0001 ……. * verticle diffusion coefficient (ak)

126.76……. * river 1 discharge rate cubic meters/s (q)

112 ……. * x grid cell number of river mouth 1 (irx)

98 ……. * y grid cell number of river mouth 1 (iry)

1.0 ……. * river 1 depth at it's mouth meters (dr)

100.0 ……. * width of river 1 meters (rwidth)

0.002 ……. * river 1 suspended load bulk density gm/cc (rrsi)

24.6 ……. * river 2 discharge rate cubic meters/s (q2)

144 ……. * x grid cell number of river mouth 2 (irx2)

64 ……. * y grid cell number of river mouth 2 (iry2)

1.0 ……. * river 2 depth at it's mouth meters (dr2)

100.0……. * width of river 2 meters (rwidth2)

0.002 ……. * river 2 suspended load bulk density gm/cc (rrsi2)

0.0000000005 ……. * horizontal mixing length coefficient (ak3)

10000.0 ……. * surfzone mixing length coefficient (ak4)

1000.0 ……. * river plume mixing length coefficient (ak5)

9 ……. *number of grain size bins (ibins)

1 …… *verticle datum 1 = surface, 0 = local bottom boundary layer (verdat)

2 ……. *total number of layers for grain# output 2-4(numlay)

0.0 ……. *layer 1 hardwired to surface - 1 meter (alay1)

0.0 ……. *layer 2 hardwired to local bottom + 1 meter (alay2)

4.0 …… *layer 3 hardwired to alay3=dmix+100 if two_layer.NE.0 (alay3)

6.0 …… *layer 4 hardwired to alay4=dmix-100 if two_layer.NE.0 (alay4)

0 ……. *surfzone resuspension switch 1=yes 0=no (surf)

0 ……. *river switch 1=yes 0=no (river)

0 …… *river 2 switch 1=yes 0=no (1 if 2nd river output considered) (river2)

1 ……. *bottom resuspension switch 1=yes 0=no (bottom)

2.65……. *mean grain density offshore g/cc (rhos)

2.65 ……. *mean grain density river g/cc (rhosr)

2.65 ……. *mean grain density river 2 g/cc(rhosr2)

1.0 ……. *coefficient to modify settling for time step model (tcon)

631.3 ……. *coefficient to modify river settling time step model (tconriv)

2.0 ……. *size of time step in hours (deltat)

0 ……. *number of time step 0=nowcast initialization (timestep)

10.0 ……. *background number of grains far offshore mg/l (n0)

2.5 ……. *slope of hyperbolic distribution far offshore (gamma)

33.0 ……. *ocean salinity in ppt (salo)

.00103 ……. *verticle mixing fresh water (w0sal)

1.0 …….*ocean salinity horizontal mixing length coefficient (ak3s)

62.0 ……. * river plume salinity coefficient (ak5s)

500000.0 ……. *reciprocal saline diffusivity (aksal)

0.07161……. *slope of cdom absorption with salinity (domslope)

2.266 ……. *intercept of cdom absorption with salinity (dominter)

0.07 ……. *minimum value of cdom absorption (domback)

25.6203 ……*coefficient to modify salinity decay for timestep model (tconsal)

0.1 ……. *null point coefficient (ak7)

33 ……*Upper Left corner latitude degrees (ilat1) also used by oceanbat*****

30.0……. *****& decimal minutes (z) also used by oceanbat*****

1 ……. *2 layer calculation switch 0=single layer system (two_layer)

5.0 …… *surface wind speed knots (v) **from time step variation menu

1.0 ……. *wind friction coefficient (ak8)

1013.0 *atmospheric pressure in millibars (p_mbar)*from time step variation menu

1…… *dmix forecast switch 0=mixed layer depth calculated internally (dmix_for)

20.0……. *mixed layer depth meters**0=single -1 =wind dep(dmix)

0.0001 ……. * lower layer mixing length coefficient (ak2_l)

0.01……. * lower layer verticle diffusion coefficient (ak_l)

1.0……. * lower layer horizontal mixing length coefficient (ak3_l)

1000.0 ……. *lower layer river plume mixing length coefficient (ak5_l)

1.0 ……. *coefficient to modify settling for time step model (tcon_l)

631.3…… *coefficient to modify river settling time step model (tconriv_l)

15.0 …… *default mixed layer depth when wind calculated mld selected (n0_l)

2.5 ……. *slope of hyperbolic distribution far offshore (gamma_l)

0.1… *ocean salinity difference between surface & bottom layers in ppt (delsal_l)

.00103 ……. *verticle mixing fresh water (w0sal_l)

0.000236 …… *ocean salinity horizontal mixing length coefficient (ak3s_l)

62.0 ……. * river plume salinity coefficient (ak5s_l)

100000.0 ……. *reciprocal saline diffusivity (aksal_l)

25.6203 ……*coefficient to modify salinity decay for timestep model (tconsal_l)

4.2 Forecast Simulation with Coastal Evolution Model (CEM)

In this section we describe a 3-dimensional simulation of the evolution of shorezone change in the Torrey Pines Sub-Cell. The co-registration of the 3-dimensional computational domain for these simulations is found in Figure 55. It includes the reach of shelf and shorezone between the USGS survey range 237x at the southern end of the Torrey Pines Sub-Cell adjacent the Scripps Submarine Canyon, and extends north the USGS survey range 230x at the northern end of the sub-cell at the San Elijo lagoon. Along this reach there are complex variations in the shelf geometry that create a high degree of variability in the wave shoaling and divergence of drift, as evidenced by the refraction/diffraction pattern in Figure 13. An oblique 3-dimensional view in Figure 56 shows the sediment surface (gray) from the bottom20.txt input file and the bedrock surface (brown) from the subbot20.txt input file. These surfaces prescribe the initial "time-zero" condition for the Torrey Pines Sub-Cell simulation. Note the rocky outcropping along the shelf break at the northern end of the sub-cell off Solana Beach in Figure 56, indicating that the sediment cover is very thin in this region. This is in part due to the erosion resistant Del Mar (Td) formation that comprises the bedrock in this region. The erosion resistant nature of this bedrock has resulted in a relatively narrow wave cut platform that limits the carrying capacity for sand here and contributes to the well known tendencies for denuded beaches in Solana Beach. The simulation will be run forward in time 200 years beginning with the initial condition shown in Figure 56. To provide 200 years of wave forcing, the CDIP proxy wave record from Section 2.3 was looped twenty times. During this period, the river sediment flux input to the Oceanside Cell was shut off ($J = 0$), providing a worst case scenario of the combined effects of drought and anthropogenic impacts

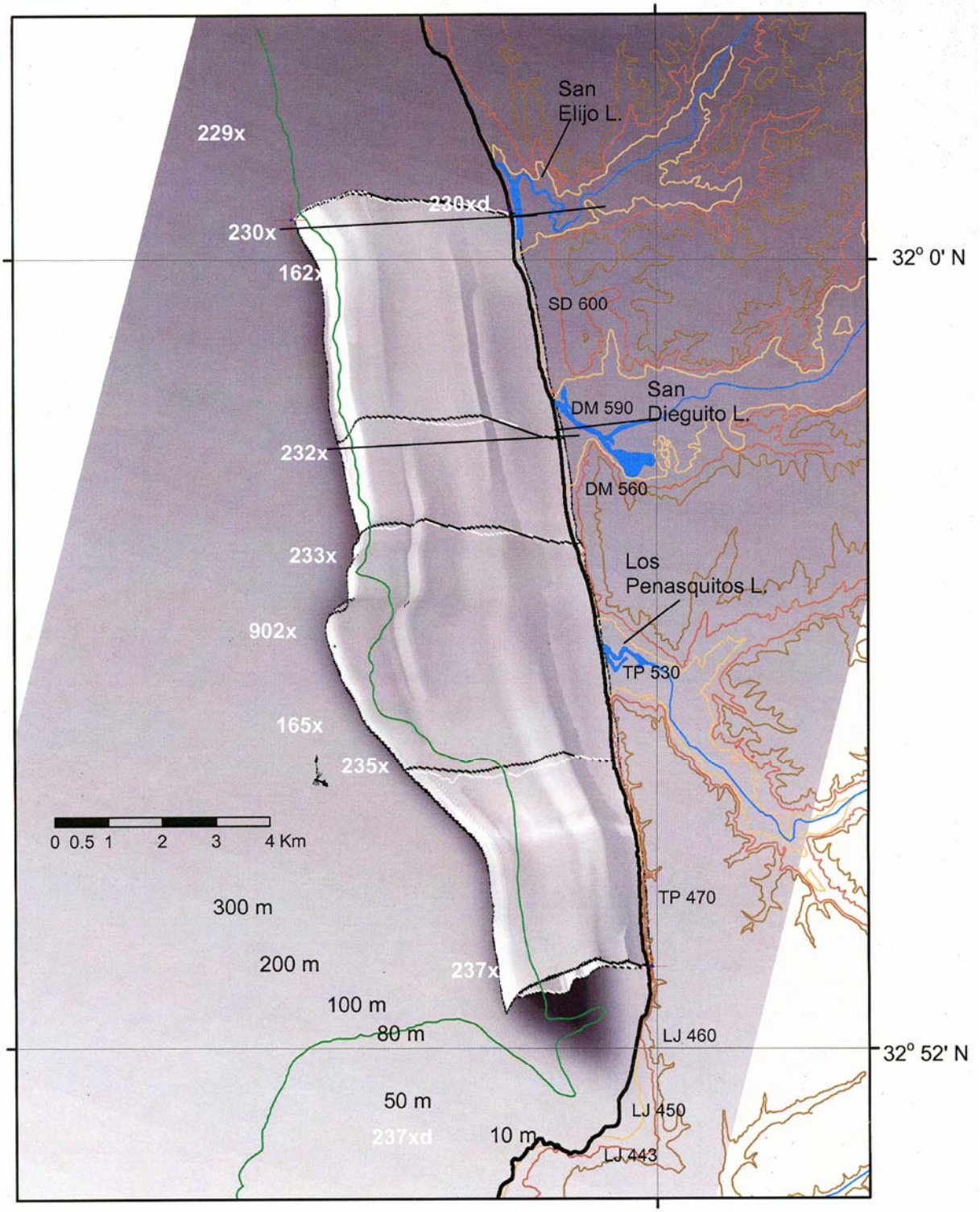

Figure 55: Co-registration of the 3-dimensional CEM grid in the Torrey Pines Sub-Cell.

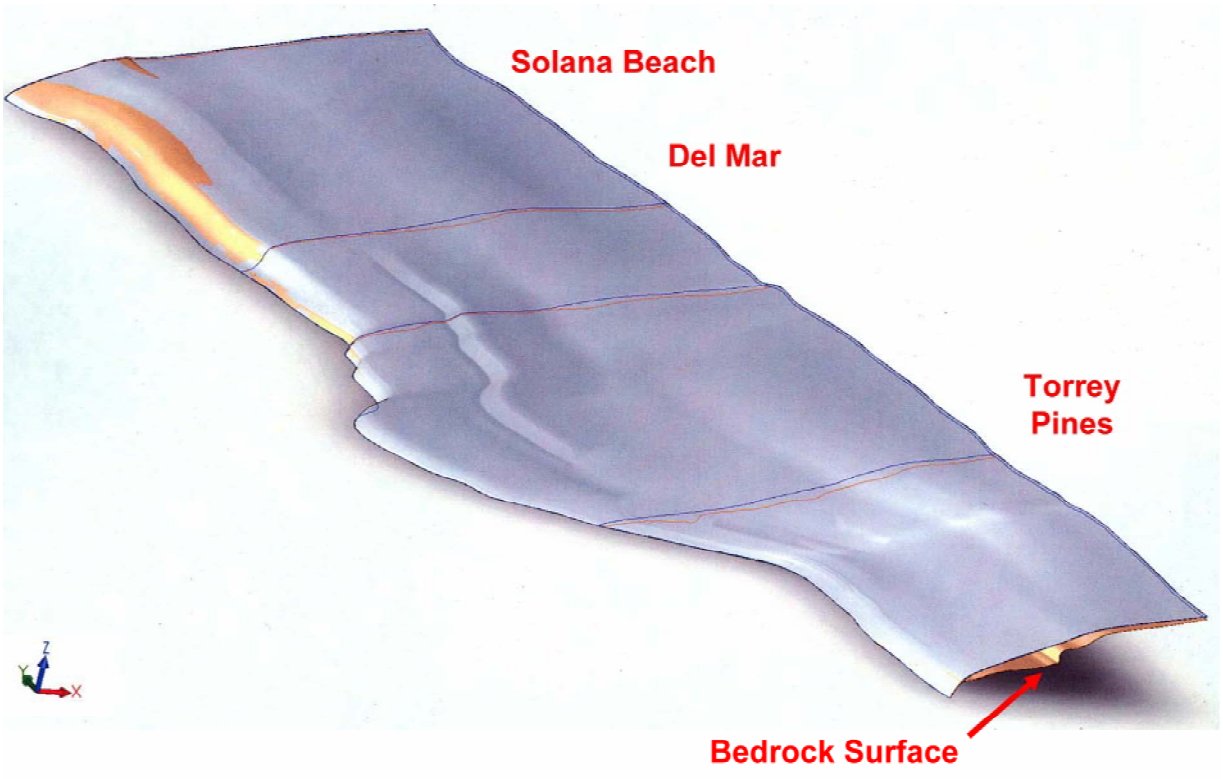

Figure 56: Initial (*t* = 0 yr) 3-dimensional sediment (gray) and bedrock (brown) surfaces for CEM forecast simulation in Torrey Pines Sub-Cell.

through inland dam construction and watershed intervention. To isolate the effects of anthropogenic impacts, the sealevel remains constant during these simulations.

Figure 57 shows a 3-dimensional simulation of the Torrey Pines Sub-Cell 56 years into the future from the initial condition in Figure 56. The effects of 56 years of on-going wave erosion in the absence of new sediment influx from water sheds is apparent, with denuding of the shorezone occurring from Solana Beach southward to Torrey Pines State Beach. Presently beaches along this section of coast are sustained in large part by sediment influx from the San Dieguito River. This simulation shows how those beaches would be lost of sediment flux from the San Dieguito River were cut off. Only a small reserve of shorezone sand and beach remains at the southern end of the Torrey Pines Sub-Cell (along Blacks Beach) after 56 years of sediment starvation.

If sediment starvation were continued for 200 years into the future, the Torrey Pines Sub-Cell would loose all of its beaches and shorezone sediment reserves out to closure depth, as revealed by the CEM forecast simulation in Figure 58. A few transient patches of thin deposits remain, but these structures are not stable in the model forecasts from one time step to the next. They may represent numerical instabilities in the model. We do not have sufficient run time experience with the model at this time of writing to assess those stability issues.

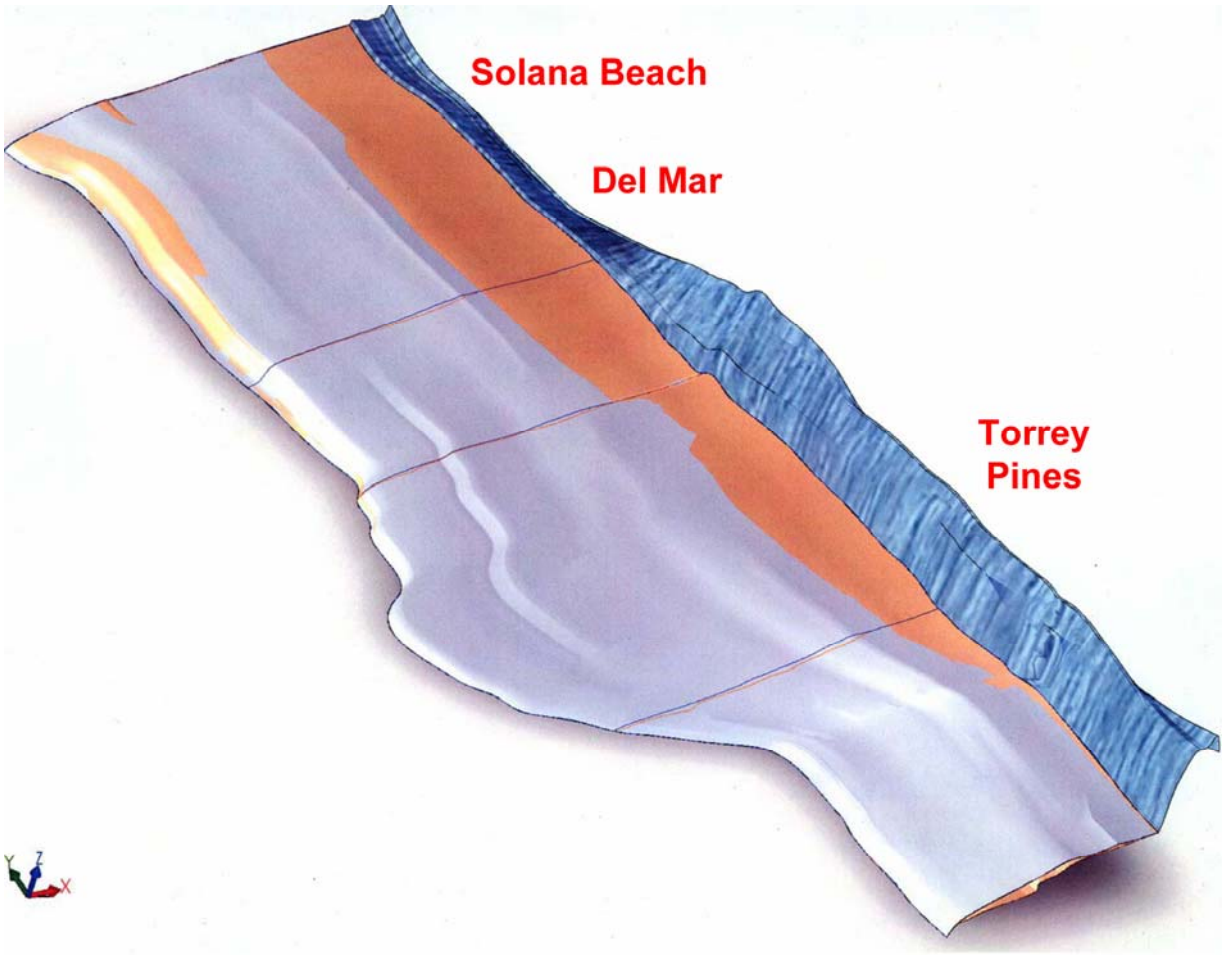

Figure 57: Three-dimensional Torrey Pines Sub-Cell forecast of sediment (gray) and bedrock (brown) surfaces from CEM simulation at time *t* = 56 yr forward from initial condition in Figure 56.

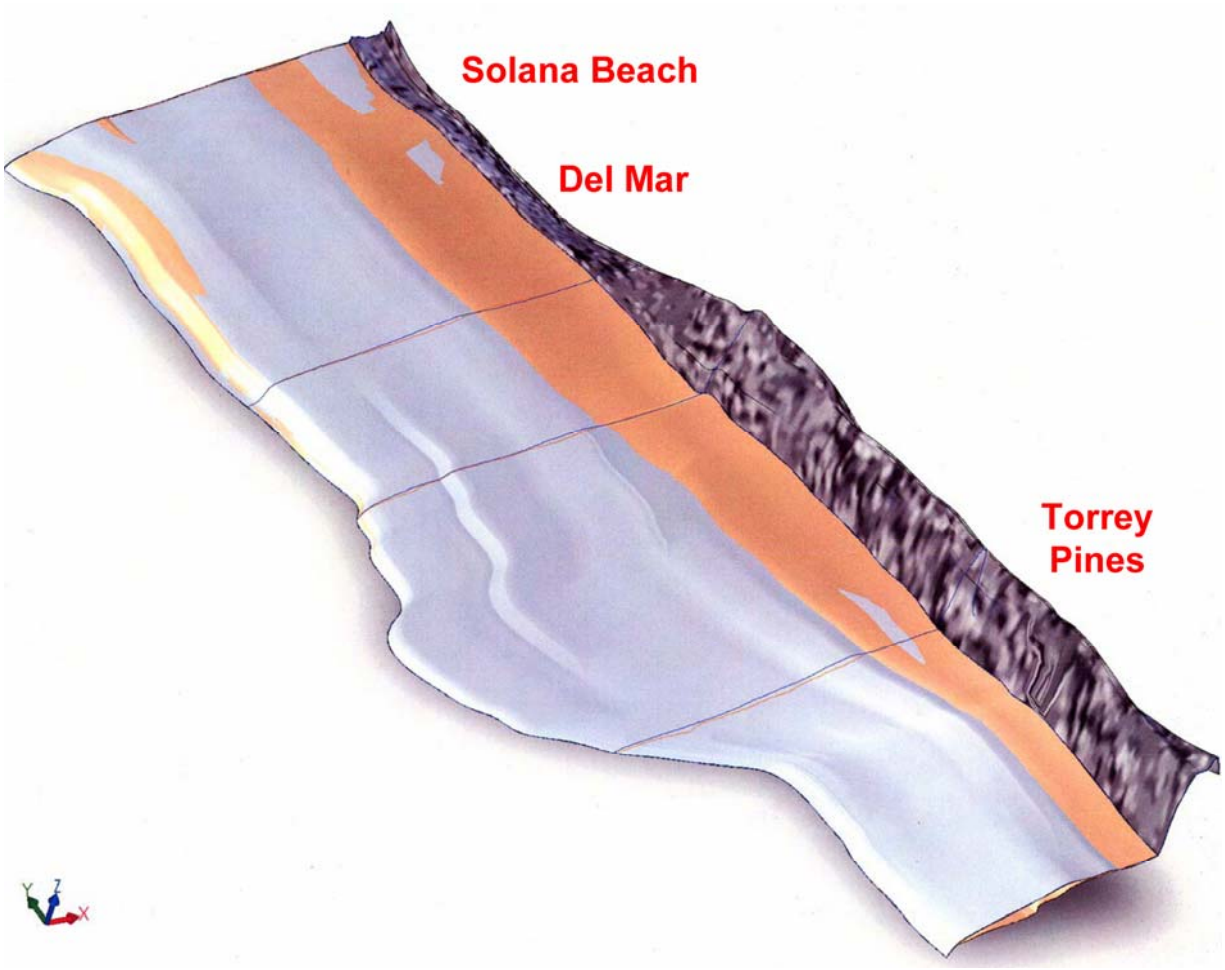

Figure 58: Three-dimensional Torrey Pines Sub-Cell forecast of sediment (gray) and bedrock (brown) surfaces from CEM simulation at time *t* = 56 yr forward from initial condition in Figure 56.

5. Conclusions

We have developed and successfully tested a coastal evolution model on a limited reach of coastline in the southern end of the Oceanside Cell (Torrey Pines Sub-Cell). From the results of those tests and the data bases developed to run them, we have been able to make extrapolations to the entire Oceanside Cell that may have profound implications for the future.

We have developed computational principles that indicate beaches must maintain a minimum supply of sand referred to as the *critical mass* in order to sustain stable equilibrium forms. Extrapolating our simulations to the 84 km of coast that make up the Oceanside Cell, we estimate the critical mass of the cell to be 117 million m^3 of sand. From our streamflow and sediment flux databases, we estimate that dam building and hardening of the watersheds of the Oceanside Cell have reduced sediment input to the cell by 12 million m^3, a deficit of 10% of the critical mass.

Our simulations of beach equilibrium change in the presence of rising sealevel indicate that the critical mass required to sustain equilibrium grows with rising sealevel. Assuming a consensus estimate that sealevel will rise 50 cm in the coming century, the critical mass requirements will increase by 34 million m^3 of sand.

Our forecast simulations with the CEM under sediment starved conditions indicate we will loose all the beaches in the southern portion of the Oceanside Littoral Cell within 200 years, and 90% of those beaches within 50 yrs. Between the combined effects of anthropogenic impacts in the watersheds, and sealevel rise under global warming scenarios, the Oceanside Littoral Cell is facing a 46 million m^3 deficit of sand or 39 % of the present critical mass requirements.

Our data bases of the sub-bottom and sediment cover in the southern portion of the Oceanside Littoral Cell indicate several ancient terrace formations containing ancient beaches. Some of these ancient beaches have formed large pools of sand deposited in bowls hollowed out in the friable formations of Ardath shale. These ancient beach reserves are at depths accessible by modern hopper dredges and could be recovered to replenish the projected deficit in critical mass. Using the SANDAG beach restoration project as a cost model, it would require an investment of $500 million amortized over the next 100 years to recover the projected critical mass deficit form off shore reserves. While a seemingly daunting expenditure of public funds, these beach nourishment/preservation requirements should be weighed against the following economic realities. Roughly, 27 million people in California live within 50 km of the coast (Resources Agency, 2001). The state's population is projected to grow by 32.8% in the next 20 years (California Dept. of Finance, 2001). Presently, recreational spending at California's beaches is estimated at $61 billion, including $15 billion/year in tax revenues (CDBW and SCC, 2002). Therefore, the economic value of the coast in tourism alone is double the state's agricultural output (CDFA, 2000) which is the highest in the nation. Not reflected in this estimate of the value of the coast is the net worth of the property and infrastructure located there.

6. References

Abbott, M. B., A. Damsgaard, and G. S. Rodenhuis, 1973, "System 21, Jupiter," Jour. Hydraulic Res., vol. 11, no. 1.

Aijaz, S. and S. A. Jenkins, 1994, "On the electrokinetics of the dynamic shear stress in fluid mud suspensions, Jour. Geophys. Res., vol. 99, no. C6, p. 12,697-12,706.

Allen, J. R. L., Sedimentary Structures, Their Character and Physical Basis. Amsterdam: Elsevier, 1984.

_____, 1985, Principles of Physical Sedimentology. London, Boston: George Allen & Unwin.

Bagnold, R. A., 1939. Committee on wave pressure: Interim report on wave-pressure research. Journal Institution of Civil Engineers, 12, 201-26.

Bagnold, R. A., 1947, "Sand movement by waves: Some small-scale experiments with sand of very low density," J. Inst. Civ. Eng., 27, p. 447-469,

Bagnold, R. A., 1963, "Mechanics of marine sedimentation," in The Sea, v. 3, The Earth Beneath the Sea, edited by M. N. Hill, p. 507-528, Wiley-Interscience, New York, London, 963 pp.

Bailard, J. A. and D. L. Inman, 1981, "An energetics bedload model for a plane sloping beach: local transport," J. Geophys. Res., 86(C3), 2035-2043,

Bascom, W. N., 1951, "Relationship between sand size and beach face slope," EOS Trans. AGU, 32(6) p. 866-874.

Batchelor, G. K., 1970, An Introduction to Fluid Dynamics, Cambridge at the University Press, 615 pp.

Baumgartner, T. R., Soutar, A. and Ferreira-Bartrina, V., 1992, "Reconstruction of the history of Pacific sardine and northern anchovy populations over the past two millennia from sediments of the Santa Barbara Basin, California," CalCOFI Reports, v. 33, p. 24-40.

Baumgartner, T. R., V. Ferreira, J. Cowen & A. Soutar, 1992a, "Reconstruction of a twentieth century wave chronology from the central Gulf of California," p. 606-616 in J. P. Dauphin & B. Simoneit, eds, The Gulf and Penninsular Province of the Californias, Amer. Assoc. Pet. Geol., Memoir 47,

Baumgartner, T. R., A. Soutar & V. Ferreira-Bartrina, 1992b, "Reconstruction of the history of Pacific sardine and northern anchovy populations over the past two millennia from sediments of the Santa Barbara Basin," CalCOFI Reports, v. 33:24, 40 pp.

Baumgartner, T. R., & seven others, in preparation 1997, "A sedimentary record of small pelagic fish abundances from the west coast of Vancouver Island," Canadian Jour. Fisheries.

Berger, W. H. and Labeyrie, L. D., 1987, "Abrupt climate change - an introduction," p. 3-22, in W. H. Berger and L. D. Labeyrie (eds), Abrupt Climate Change, D. Reidel Pub. Co., Dordrecht & Boston, 425 pp.

Berkoff, J. C. W., N. Booij and A. C. Radder, 1982, "Verification of numerical wave propagation models for simple harmonic linear water waves," Coastal Engineering, 6, p. 255-279.

Bjerkness, J., 1969, "Atmospheric teleconnections from the equatorial Pacific," Monthly Weather Rev., v. 97, p. 163-172.

Boas, M. L., 1966, Mathematical Methods in the Physical Sciences, John Wiley & Sons, Inc., New York, 778 pp., 1966.

Bond, G. and 9 Others, 1997, "A pervasive millennial-scale cycle in North Atlantic Holocene and glacial climates," Science, v. 278, p. 1257-66.

Bowen, A. J., 1980, "Simple models of nearshore sedimentation, beach profiles and longshore bars," in The Coastline of Canada, Littoral Processes and Shore Morphology, edited by S. B. McCann, p. 1-11, Geological Survey of Canada, Paper 80-10.

Brownlie, W. R. and Taylor, B. D., 1981a, "Coastal sediment delivery by major rivers in southern California, Sediment Management of Southern California Mountains, Coastal Plains, and Shorelines, Part C," California Institute of Technology, Pasadena, CA, Environmental Quality Laboratory Report No. 17-C, 314 pp.

Brownlie, W. R. & B. D. Taylor, 1981b, "Sediment management of southern California mountains, coastal plains and shoreline, Part C," Coastal Sediment Delivery by Major Rivers in southern California, California Institute of Technology, Pasadena, CA, Environ. Quality Lab. Report 17-C, 314 pp.

Brunn, P., 1954, "Coast erosion and the development of beach profiles," Tech. Memo 44, 79 pp. + appendix, U. S. Army Corps of Engineers, Beach Erosion Board, Washington, D. C., 1954.

Burt, W. V., M. C. Powers, and D. W. Pritchard, 1952, “Operation Mud – Results of Studies of Mine Penetration in the York River,” Chesapeake Bay Institute: Johns Hopkins Univ., Ref. No. 52-25.

California Department of Water Resources, 1967, “Groundwater resources of the San Diego Region”, 2 volumes.

California Department of Boating and Waterways and State Coastal Conservancy (CDBW and SCC). (2002). *California Beach Restoration Study,* Sacramento, CA http://www.dbw.ca.gov/beachreport.htm

California Department of Finance. (2001). *Interim County Population Projections*, Sacramento, CA, http://www.dof.ca.gov

California Department of Food & Agriculture (CDFA). (2000). *Agriculture Statistical Review*, http://www.cdfa.ca.gov/docs/CAStats01/pdf

California Department of Water Resources (CDWR). (2003) "California Water Plan, Update 2003." Bulletin 160-03, Sacramento, CA, http://www.waterplan.water.ca.gov/b160/indexb160.html

Cayan, D. R. and Peterson, D. H., 1989, "The influence of North Pacific atmospheric circulation on streamflow in the west," p. 375-397 in D. H. Peterson, ed., Aspects of Climate Variability in the Pacific and the Western Americas, Amer. Geophysical Union, Monograph 55, Washington, D. C.

Cayan, D. R., 1996, "Interannual climate variability and snowpack in the western United States," Jour. of Climate, v. 9, p. 928-948.

CDIP, 1984-1988, "Coastal data information program, monthly reports," U. S. Army Corps of Engineers, California Department of Boating and Waterways, Monthly Summary Reports #97-#150.

CDIP, 1976-1995, "Coastal Data Information Program, Monthly Reports," U. S. Army Corps of Engineers, California Department of Boating and Waterways, SIO Reference Series, 76-20 through 95-20.

CDIP, 1993-1994, "Monthly Summary Report," SIO Reference Series (93-27) through (94-19).

Chen, D., S. E. Zebiak, A. J. Busalacchi & M. A. Cane, 1995, "An improved procedure for El Niño forecasting: implications for predictability," Science, v. 269, p. 1699-1702.

Chu, P. C., A. F. Gilles, C. Fan, and P. Fleischer, 2002, “Hydrodynamics of Falling Mine in Water Column,” J. Counter-Ordnance Tech., (5th Int. Symposium on Tech. and Mine Problem).

Cialdi, A., 1866. Sul moto ondoso del mare e su le correnti di esso specialmente su quelle littorali pel comm., Roma.

Cole, J. E., G. T. Shen, K. G. Fairbanks & M. Moore, 1992, "Coral monitors of El Niño/Southern Oscillation dynamics across the equatorial Pacific," p. 349-375 in H. F. Diaz and V. Markgraf, eds., El Niño, Historical and Paleoclimatic Aspects of the Southern Oscillation, Cambridge Univ. Press, Cambridge, U. K., 476 pp.

Cole, J. E., R. G. Fairbanks & G. T. Shen, 1993, "Recent variability in Southern Oscillation: isotopic results from a Tarawa Atoll coral," Science, v. 260, p. 1790-93.

Collins, T. J., 1980, “Investigating bridge scour,” Railway Track and Structure.

Connor, J. J. and J. D. Wang, 1973, "Finite element modeling of two-dimensional hydrodynamic circulation," MIT Tech Rpt., #MITSG 74-4, p. 1-57.

Conte, S. D. and C. de Boor, 1972, Elementary Numerical Analysis, Second Edition, McGraw-Hill Book Co., New York.

Chiew, Y. M. and B. W. Melville, 1987, “Local scour around bridge piers,” J. Hydraulic Res, vol. 25, pp. 15–26.

Dalrymple, R. A. J. T. Kirby and P. A. Hwang, 1984, "Wave diffraction due to areas of energy dissipation," Jour. Waterway Port, Coast, and Ocean Engineering, vol. 110, p. 67-79.

Dean, R. G., 1977, "Equilibrium beach profiles: U. S. Atlantic and Gulf Coasts," Univ. of Delaware, Ocean Engineering, Report 12, 30 pp. + appendix.

Dean, R. G., 1991, "Equilibrium beach profiles: characteristics and applications," J. Coastal Res., 7(1), 53-84.

de Beaumont, L. E., 1845. Levees de sable et de galet, Lecons de Geologie Pratique, (Septieme lecon). v. 1. In Bertrand, P., Paris [Excerpted in part In Schwartz, M. L. (ed.) 1973 Barrier Islands. Stroudsburg: Dowden, Hutchison & Ross].

deGroot, S. R. & P. Mazur, 1984, Non-Equilibrium Thermodynamics, Dover Pub., Inc., New York, 510 pp., 1984.

Desmond, J. S., Zedler, J.B., and G.D. Williams, 2000, "Fish use of tidal creek habitat in two southern California salt marshes", Ecological Engineering, vol. 14, p. 233-252.

Dickinson, W. R., 1988, "Provenance and sediment dispersal in relation to paleotectonics and paleogeography of sedimentary basins," in Kleinspehn, K. L. and Paola, C., ed., New Perspectives in Basin Analysis: New York, Springer-Verlag, p. 3-25.

Dill, R. F., 1958, "The Burial and Scouring of Ground Mines on a Sandy Bottom," San Diego, CA: U. S. Navy Electronics Laboratory, Research Report NEL 861.

DNOD, 1977-1978, "Deep water wave statistics for the California coast," station 5," Dept. of Nav. and Ocn. Dev., Sacramento, CA, 1037 pp.

Donohue, J.J. and L. E. Garrison, 1954, "An Evaluation of Mine Behavior Observations in Four Test Areas," Narragansett Marine Laboratory: Univ. Rhode Island, Reference 54-13.

Escoffier, F.F., 1977, "Hydraulics and stability of tidal inlets", GITI Report 3, U.S. Army Corps of Engineers, February 1976, 55 pp.

Douglas, A. V., Cayan, D. R. and Namias, J., 1982, "Large-scale changes in North Pacific and North American weather patterns in recent decades," Monthly Weather Review, v. 110, n. 12, p. 1851-62.

Emery, K. O., 1960. The Sea off Southern California. New York: John Wiley & Sons.

Finlayson, B. A. and L. E. Scriven, 1965, "The method of weighted residuals and its relation to certain variational pricniples for the analysis of transport processes," Chemical Engineering Science, vol. 20.

Finlayson, B. A., 1972, The Method of Weighted Residuals and Variational Principles, Academic Press.

Fisher, O., 1866. On the disintegration of a chalk cliff. Geological Magazine, 3, 354-6.

Flick, R. E., 1978, “Study of shoaling waves in the laboratory,” University of California, San Diego, Ph. D. Dissertation, 159 pp.

Flick, R. E., 1993, "The myth and reality of southern California beaches," Shore & Beach, v. 61, n. 3, p. 3-13.

Flick, R. E., R. T. Guza and D. L. Inman, 1981, "Elevation and velocity measurements of laboratory shoaling waves," J. Geophys. Res., 86(C5), 4149-4160.

Flick, R. E. and D. R. Cayan, 1984, "Extreme sea levels on the coast of California," Coastal Eng. 1984, Proc. 19th Int. Conf. (Houston), Amer. Soc. Civil Eng., New York, p. 886-896.

Foxwell, D., 1991, “New technology Takes on the Sea Mine,” Int. Defense Review,

pp. 1097–99/1101–1102.

Frazier, D. E., and C. E. Miller, 1955, “Geological and Engineering Characteristics at Mine Behavior Test Sites,” Narragansett Marine Laboratory: Univ. Rhode Island, Reference 55-16.

Fujita, H., 1962, Mathematical Theory of Sedimentation Analysis, York, Academic 315 pp.

Gallagher, E. L., S. Elgar, and R. T. Guza, 1998, “Observations of Sand Bar Evolution on a Natural Beach,” J. Geophysical Res., vol. 103, no. C2, pp. 3203–3215.

Gallagher, R. H., 1981, Finite Elements in Fluids, John Wiley & Sons, New York, 290 pp.

Garrels, R. M. and MacKenzie, F. T., 1971, Evolution of Sedimentary Rocks, W. W. Norton & Co., Inc., New York, 397 pp.

Gilbert, G.K., 1885. The topographic features of lake shores. In U. S. Geological Survey. Fifth Annual Report, 1883-84, Washington, D.C.

Griggs, G. B. and Trenhaile, A. S., 1994. Coastal cliffs and platforms. In Carter R. W. G. and Woodroffe, C. D. (eds.), Coastal Evolution: Late Quaternary shoreline morphodynamics. Cambridge, UK: Cambridge University Press.

Grotkop, G., 1973, "Finite element analysis of long-period water waves," Computer Methods in Applied Mechanics and Engineering, 2, p. 147-157.

Gu, D. & S. G. H. Philander, 1997, "Interdecadal climate fluctuations that depend on exchanges between the tropics and extratropics," Science, v. 275, p. 805-807.

Guymon, G., 1973, "Finite element solution for general fluid motion," J. Hyd. Div., ASCE, vol. 99, no. HY 6, June

Guza, R. T. and E. B. Thornton, 1985, "Velocity moments in nearshore," Jour. of Waterway, Port, Coastal and Ocean Eng., 111(2),

Haigh, J. D., 1996, "The impact of solar variability on climate," Science, v. 272, p. 981-984.

Hancock, G. S. and Anderson, R. S., 2002. Numerical modeling of fluvial strath-terrace formation in response to oscillating climate. Geological Society of America, Bulletin, 114, 1131-42.

Havelock, T. H., 1940. The pressure of water waves upon a fixed obstacle. Proceedings of the Royal Society, London, A, 175, 409-21.

Hay, W. W., 1994, "Pleistocene-Holocene fluxes are not the Earth's norm," p. 15-24 in Material Fluxes on the Surface of the Earth, National Academy Press, Washington, D. C., 170 pp.

Heun, M. and (6) others, 1997, "Site of einkorn wheat domestication identified by DNA fingerprinting," Science, v. 278, p. 1312-14.

Heusser, L. E. & F. Sirocks, 1997, "Millennial pulsing of environmental change in southern California from the past 24 k.y.: a record of Indo-Pacific ENSO events," Geology, v. 25, n. 3, p. 243-246.

Holmgren-Urba, D. and Baumgartner, T. M., 1993, "A 250-year history of pelagic fish abundances from the anaerobic sediments of the central Gulf of California," CalCOFI Reports, v. 34, p.60-68.

Horrer, P. L., 1950, "Southern hemisphere swell and waves from a tropical storm at Long Beach, California," Beach Erosion Bull., v. 4, n. 3, p. 1-18.

Hunt, J. N. and B. Johns, 1963, "Currents induced by tides and gravity waves," Tellus, 15(4), p. 343-51, 1963.

Hunt, I. A., Jr., 1959, "Design of seawalls and breakwaters," J. Waterways, Harbors Div., 85, p. 123-152, 1959.

Hurst, H. E., 1951, "Long-term storage capacity of reservoirs," American Soc. Civil Engineers, Trans. v. 116, p. 770-799.

Hurst, H. E., 1957, "A suggested statistical model of some time series which occur in nature," Nature, v. 180, n. 4584, p. 494.

Inman, D. L., 1953, "Areal and seasonal variations in beach and nearshore sediments at La Jolla, California," Tech. Memo. 39, 134 pp. Beach Erosion Board, U. S. Army Corps of Eng., Washington, D. C.

Inman, D. L. and T. K. Chamberlain, 1953, "Particle-size distribution in nearshore environments," Jour. Sed. Petrology, v. 23, p. 127-128.

Inman, D. L., 1960, "Shore Processes," McGraw-Hill Encyclopedia of Science and Technology, v. 12, p. 299-306.

Inman, D. L. and A. J. Bowen, 1962, "Flume Experiments on Sand Transport by Waves and Currents," in Proc. 8th Conf. on Coastal Engin., Council on Wave Research, Univ. of California, San Diego, pp. 137–150.

Inman, D. L. and R. A. Bagnold, 1963, "Littoral processes," p. 529-553 in The Sea, v. 3 of The Earth Beneath the Sea, edited by M. N. Hill, Interscience, John Wiley & Sons, New York, London.

Inman, D. L., Gayman, W. R. and Cox, D. C., 1963, "Littoral sedimentary processes on Kauai, a sub-tropical high island," Pacific Science, v. 17, n. 1, p. 106-130.

Inman, D. L. and Nordstrom, C. E., 1971, "On the tectonic and morphologic classification of coasts," Jour. of Geology, v. 79, n. 1, p. 1-21.

Inman, D. L. and Brush, B. M., 1973, "The coastal challenge," Science, v. 181, n. 4094, p. 20-32.

Inman, D. L., 1983. Application of coastal dynamics to the reconstruction of paleocoastlines in the vicinity of La Jolla, California. In Masters, P. M. and Flemming, N. C. (eds.), Quaternary Coastlines and Marine Archaeology. London: Academic Press.

Inman, D. L. and S. A. Jenkins, 1983, "Oceanographic Report for Oceanside Beach Facilities," prepared for City of Oceanside, Oceanside, California, August, 1983, 206 pp.

Inman, D. L., and R. Dolan, 1989, "The Outer Banks of North Carolina: Budget of Sediment and Inlet Dynamics Along a Migrating Barrier System," J. Coastal Research, vol. 5, no. 2, pp. 193–237, 1989.

Inman, D. L. and Masters, P. M., 1991, "Coastal sediment transport concepts and mechanisms," Chapter 5 (43 pp.) in State of the Coast Report, San Diego Region, Coast of California Storm and Tidal waves Study, U. S. Army Corps of Engineers, Los Angeles District Chapters 1-10, Appen. A-I, 2 v.

Inman, D. L. and P. M. Masters, 1991, "Budget of sediment and prediction of the future state of the coast," Chapter 9 (105 pp.) in State of the Coast Report, San Diego Region, Coast of California Storm and Tidal Waves Study, U. S. Army Corps of Engineers, Los Angeles District, Chapters 1-10, Appen. A-I; 2v.

D. L. Inman, D. L., M. H. S. Elwany, and S. A. Jenkins, "Shorerise and Bar-Berm Profiles on Ocean Beaches," J. Geophysical Res., vol. 98, no. C10, pp. 18,181–18,199, Oct. 1993. Available: http://repositories.cdlib.org/sio/cmg/11/

Inman, D. L. and Masters, P. M., 1994. Status of research on the nearshore. Shore & Beach, 62, 11-20.

Inman, D. L., M. H. S. Elwany and S. A. Jenkins, 1993, "Shorerise and bar-berm profiles on ocean beaches, Jour. Geophys. Res., 98(C10), p. 18, 181-199.

Inman, D. L. and P. M. Masters, 1994, "Status of Research on the Nearshore," Shore & Beach, vol. 62, no. 3, pp. 11–20.

Inman D. L. and S. A. Jenkins, 1996, “A chronology of ground mine studies and scour modeling in the vicinity of La Jolla," University of California,San Diego, Scripps Institution of Oceanography, SIO Reference Series 96-13, 26 pp.

Inman, D. L., Jenkins, S. A. and Elwany, M. H. S., 1996, "Wave climate cycles and coastal engineering practice," Coastal Eng., 1996, Proc. 25th Int. Conf., (Orlando), Amer. Soc. Civil Eng., New York, v. 1, Ch 25, p. 314-327.

Inman, D. L. and Jenkins, S. A., 1997, "Changing wave climate and littoral drift along the California coast," California and the World Ocean '97, San Diego, CA, 12 pp.

Inman, D. L., S. A. Jenkins & M. H. S. Elwany, 1996, "Wave climate cycles and coastal engineering practice," Coastal Eng., 1996, Proc. 25th Int. Conf., (Orlando), Amer. Soc. Civil Eng., New York, v. 1, Ch 25, p. 314-327.

Inman, D. L. and S. A. Jenkins, 1996, "A chronology of ground mine studies and scour modeling in the vicinity of La Jolla," SIO Reference Series, n. 96-13, 26 pp.

Inman, D. L. and S. A. Jenkins, 1999, “Climate Change and the Episodicity of Sediment Flux of Small California Rivers,” J. Geology, vol. 107, no. 3, pp. 251–270, May. Available: http://repositories.cdlib.org/sio/cmg/2/

Inman, D. L. and Jenkins, S. A., 2002. Scour and burial of bottom mines, a primer for fleet use. University of California, San Diego, Scripps Institution of Oceanography, SIO Reference Series 02-8, text, fig. & appen. http://repositories.cdlib.org/sio/reference/02-8/

Inman, D. L., Masters, P. M. and Jenkins, S. A., 2002. Facing the coastal challenge: Modeling coastal erosion in southern California. In Magoon, O.

T., et al., (eds.), California and the World Ocean '02. American Society of Civil Engin., Reston, VA.

Inman, D. L. and S. A. Jenkins, 2005, "Scour and Burial of Objects in Shallow Water," in Encyclopedia of Coastal Science, M. Schwartz, Ed. Dordrecht, Netherlands: Kluwer Academic Publishers, pp. 1020–1026.

Inman, D. L. and S. A. Jenkins, 2005, "Accretion and Erosion Waves on Beaches," in Encyclopedia of Coastal Science, M. Schwartz, Ed. Dordrecht, Netherlands: Kluwer Academic Publishers, pp. 1–4. Available: http://repositories.cdlib.org/sio/cmg/6/

Jarrett, J.T., 1976, "Tidal prism – inlet area relationships, GITI Report 3", U.S. Army Corps of Engineers, February 1976, 55 pp.

Jenkins, S. A., 1980, "Sedimentation control experiments at Mare Island Naval Shipyard," Proc. Dredging Sed. Control, P. Shelly, ed., Pub. EG&G, Washington, p. (4-1) - (11-6).

Jenkins, S. A., D. L. Inman and J. A. Bailard, 1980, "Opening and maintaining tidal lagoons and estuaries," Proc. 17th Int. Coastal Eng. Conf., Amer. Soc. Civil Eng., v. 2, p. 1528-1547.

Jenkins, S. A., D. L. Inman and W. G. Van Dorn, 1981, "Evaluation of sediment management procedures," SIO Reference Series No. 81-22, 212 pp.

Jenkins, S. A. and D. W. Skelly, 1983, "Jet array site suitability study at Charleston Naval Station," SIO Reference Series, No. 83-20, 146 pp.

Jenkins, S. A. and D. L. Inman, 1985, "On a submerged sphere in a viscous fluid excited by small-amplitude periodic motions," Jour. Fluid Mech., v. 157, p. 199-224.

Jenkins, S. A. & J. A. Bailard, 1989, Anti-sedimentation system for harbors, *World Wide Shipping,* v. 52, n. 1, p. 70-75..

Jenkins, S. A. and J. Wasyl, 1990, "Resuspension of estuarial sediments by tethered wings," Jour. Coastal Res., v. 6, no. 4, p. 961-980.

Jenkins, S. A., J. Wasyl & D. W. Skelly, 1992, Tackling trapped sediments, *Civil Engineering,* v. 62, n. 2, p. 61-64.

Jenkins, S. A. & D. L. Inman, 1999, Sand transport mechanics for equilibrium tidal inlets, *Shore & Beach* (Magoon Volume, Jan 99), v. 67, n. 1, p. 53-58.

Jenkins, S. A. and D. L. Inman, 2002, "Model for Mine Scour and Burial: An Illustrated Abstract with Technical Appendix," Scripps Institution of Oceanography: University of California, San Diego, SIO Reference Series 02-2.

Jenkins, S. A. and D. L. Inman, in press, "Analytic solutions for equilibrium profiles on ocean beaches, Jour. Geophys. Res., 32 pp.

Johnson, J.W., 1973, "Characteristics and behavior of Pacific Coast Tidal Inlets", *Journal of Waterways, Harbors and Coastal Engineering Division,* ASCE, August 1973, p. 325-339.

Johnson, J. W. and P. S. Eagleson, 1966, "Coastal processes," p. 404-492, in Estuary and Coastline Hydrodynamics, edited by A. T. Ippen, McGraw-Hill, New York, 744 pp.

Jonsson, I. G. and N. A. Carlsen, 1976, "Experimental and Theoretical Investigations in an Oscillatory Turbulent Boundary Layer," J. Hydraulic Res., vol. 14, no. 1, pp. 45–60.

K ajiura, K., 1968, "A Model of the Bottom Boundary Layer in Water Waves," Bull. of the Earthquake Res. Institute (Tokyo), vol. 46, pp. 75–123.

Kerr, R. A., 1996, "A new dawn for sun-climate links," Science, v. 271, p. 1360-61.

Keulegan, G. H. and W. C. Krumbein, 1949, "Stable configuration of bottom slope in a shallow sea and its bearing on geological processes," Trans. AGU, 30(6), 855-861, 1949.

Kirby, J. T., 1986a, "Higher-order approximations in the parabolic equation method for water waves," Jour. Geophys. Res., vol. 91, C1, p. 933-952.

Kirby, J. T., 1986b, "Rational approximations in the parabolic equation method for water waves," Coastal Engineering, 10, p. 355-378.

Kirby, J. T., 1986c, "Open boundary condition in the parabolic equation method," Jour. Waterway, Port, Coastal, and Ocean Eng., 112 (3) p. 460-465.

Kleeman, R., R. A. Colman, N. R. Smith & S. B. Power, 1996, "A recent change in the mean state of the Pacific basin climate: observational evidence and atmospheric and oceanic responses," Jour. Geophys. Res., v. 101, n. C9, p. 20,483-99.

Komar P. D. and D. L. Inman, 1970, "Longshore sand transport on beaches," Jour. Geophys. Res., vol 75, no. 30, p. 5914-5927.

Kraus, N. C. and S. Harikai, 1983, "Numerical model of the shoreline change at Oarai Beach," Coastal Eng., 7(1), p. 1-28, 1983.

Krone, R. B., 1962, Flume Studies of the Transport of Sediment in Estuarial Shoaling Processes, Final Report," Hydraulics Engineering Laboratory and Sanitary Engineering Research Laboratory, University of California, Berkeley.

Krone, R. B., 1978, "Aggregation of suspended particles in estuaries," in Estuarine Transport, Processes, B. Kjerfve, (ed.). University of South Carolina Press, Columbia, SC, p. 177-190.

Kump, L. R. and Alley, R. B., 1994, "Global chemical weathering on glacial time scales," p. 46-60 in Material Fluxes on the Surface of the Earth, National Academy Press, Washington, D. C., 170 pp.

Langbein, W. B. and Schumm, S. A., 1958, "Yield of sediment in relation to mean annual precipitation," Trans. Amer. Geophys. Union, v. 39, p. 1076-1084.

Laronne, J. B. and Mosely, M. P., 1982, "Editors comments," p. 146-154 in Laronne & Mosley, eds., Erosion and Sediment Yield, Benchmark Papers in Geology/63, Hutchinson Ross, Stroudsburg, PA, 377 pp.

Latif, M. & T. P. Barnett, 1994, "Causes of decadal climate variability over the North Pacific and North America," Science, v. 266, p. 634-637.

Leendertse, J. J., 1967, Aspects of a Computational Model for Long-Period Water-Wave Propagation, Rand Corporation, Santa Monica, California, Memorandum RM 5294-PR, May.

Leendertse, J. J., 1970, "A water quality model for well-mixed estuaries and coastal seas," vol. I, Principles of Computation, Memorandum RM-6230-RC, The Rand Corporation, Santa Monica, California, Feb.

Longuet-Higgins, M. S., 1970, “Longshore currents generated by obliquely incident waves," Jour. Geophys. Res., v. 75, n. 33, p. 6778-6789.

Longuet-Higgins, M. S., 1953, "Mass transport in water waves," Philos. Trans. Roy. Soc. London, Ser. A245, 535-581, 1953.

Lyell, C., 1873, Principles of Geology, Volume 1, D. Appleton and Company, New York.

Mantua, N. J., Hare, S. R. Zhang, Y, Wallace, J. M. and Francis, R. C., 1997, "A Pacific interdecodal climate oscillation with impacts on salmon production," Bull. Amer. Meteor. Soc., v. 78, n. 6, p. 1069-79.

Marine Advisors, 1961, "A statistical survey of ocean wave characteristics in southern California waters," prepared for the U. S. Army Corps of Eng., Los Angeles District by Marine Advisors, Inc., La Jolla, CA, 30 pp.

McMaster, R. L., L. E. Garrison, and S. D. Hicks, 1955, "Marine Sedimentation Project; Mine Behavior Studies," Narragansett Marine Laboratory: Univ. Rhode Island, Reference 55-15.

McCormick, B. W., 1979, Aerodynamics, Aeronautics and Flight Mechanics. New York: John Wiley & Sons.

Mehta, A. J., 1989, "On estuarine cohesive sediment suspension behavior, Jour. Geophys. Res., 94, (C10), p. 14303-14,314.

Mehta, A. J., E. J. Hayter, W. R. Parker, R. B. Krone and A. M. Teeter, 1989, "Cohesive sediment transport. I: Process description," Jour. Hyd. Eng., vol. 115, no. 8, p. 1076-1093.

Mehta, A. J., W. H. McAnally, Jr, E. J. Hayter, A. M. Teeter, D. Scholellhamer, S. B. Heltzel and W. P. Carey, 1989, "Cohesive sediment transport. II: Application," Jour. Hyd. Eng., vol. 115, no. 8, p. 1094-1112.

Meko, D. M., 1992, Spectral properties of Tree-Ring Data in the United States Southwest as Related to El Niño, Historical and Paleoclimatic Aspects of the Southern Oscillation, Cambridge Univ. Press, Cambridge, U. K., 476 pp.

Miller, A. J. D. R. Cayan, T. P. Barnett, N. E. Graham & J. M. Oberhuber, 1994, "The 1976-77 climate shift of the Pacific Ocean," Oceanography, v. 7, n. 1, p. 21-26.

Milliman, J. D. and Meade, R. H., 1983, "World-wide delivery of river sediment to the oceans," Jour. Geology, v. 91, n. 1, p. 1-21.

Milliman, J. D. and Syvitski, J. P. M., 1992, "Geomorphic/tectonic control of sediment discharge to the ocean: the importance of small mountainous rivers," Jour. Geology, v. 100, p. 525-544.

Monastersky, R., 1995, "Tropical trouble, two decades of Pacific warmth have fired up the globe," Science News, v. 147, p. 154-155.

Monastersky, R., 1997, "1996: year of warmth and weather reversals," Science News, v. 151, p. 38.

Mulhearn, P. J., 1993, "Experiment on Mine Burial by Scour," Maribyrnong, Victoria 3032, Australia: Materials Research Laboratory, MRL-TN-632, 1993.

_____"Experiments on Mine Burial on Impact-Sydney Harbour," U. S. Navy J. of Underwater Acoustics, vol. 43, no. 3, pp. 1271–1281.

National Oceanic and Atmospheric Association (NOAA), 1998, "Verified/Historical Water Level Data," http://www.opsd.nos.noaa.gov/data_res.html

National Oceanic and Atmospheric Association (NOAA), National Data Buoy Center, 2003. Available: http://ndbc.noaa.gov/

Norris, R. M. and Webb, R. W., 1990, Geology of California, second ed., John Wiley & Sons, 541 pp.

O'Brien, M. P., 1931, "Tidal prisms related to entrance areas," The Journal Civil Engineering, vol. 1, no. 8, p. 738-739.

O'Brien, M. P. and R. G. Dean, 1972, "Hydraulics and sedimentary stability of coastal inlets," Proc. 13th Conf. Coastal Eng., v. 11, Amer. Soc. Civil Eng., p. 761-780.

O'Brien, S. R., and 6 others, 1995, "Complexity of Holocene climate as reconstructed from Greenland ice core," Science, v. 270, p. 1962-64.

Oceanographic and Atmospheric Master Library (OAML), 2004. Available: http://navy.ncdc.noaa.gov/products/oaml.html

Oden, J. T. and E. R. A. Oliveira, 1973, Lectures on Finite Element Methods in Continuum Mechanics, The University of Alabama Press.

Peace, A. J. and N. Riley, 1983, "A Viscous Vortex Pair in Ground Effect," J. Fluid Mech., vol. 129, pp. 409–426.

Peterson, G.L., 1982, "The geologic setting of San Diego and vicinity." In Geologic Studies in San Diego, P.L. Abbot (ed.).

Pettijohn, F. J. and P. E. Potter, 1964, Atlas and Glossary of Primary Sedimentary Structures. New York: Springer-Verlag.

Picaut, J., M. Ioualalen, C. Menkes, T. Delcroix & M. J. McPhaden, 1996, "Mechanism of the zonal displacements of the Pacific warm pool: implications for ENSO," Science, v. 274, p. 1486-89.

Radder, A. C., 1979, "On the parabolic equation method for water-wave propagation," Jour. Fluid Mech., vol. 95, pt. 1, p. 159-176.

Raubenheimer, B. and R. T. Guza, 1996a, "Observations and predictions of run-up," J. Geophys. Res., 101 (C10), p. 25,575-25,587.

Raubenheimer, B. and R. T. Guza, 1996b, "Wave transformation across the inner surf zone," J. Geophys. Res., 101(C10), p. 25,589-25, 597.

A. J. Raudkivi, A. J., 1990, Loose Boundary Hydraulics. Oxford: Pergamon Press.

Reihl, H. and Meitin, J., 1979, "Discharge of the Nile River: a barometer of short-period climate variation," Science, v. 206, p. 1178-79.

Reineck, H. E. and I. B. Singh, 1975, Depositional Sedimentary Environments. New York: Springer-Verlag.

Renard, K. G., Foster, G. R. Weesies, G. A., McCool, D. K. and Yoder, D. C., 1997, "Predicting Soil Erosion by Water: A Guide to Conservation Planning

With the Revised Universal Soil Loss Equation (RUSLE)," U. S. Dept. Agriculture, Agriculture Handbook, 703, Washington, D. C., 384 pp.

Resources Agency of California. (2001). *Draft Policy on Coastal Erosion Planning and Response and Background Material.* Sacramento, CA, http://ceres.ca.gov/cra/ocean/coastal_erosion_draft.html

Ridgway, K. R. & J. S. Godfrey, 1996, "Long-term temperature and circulation changes off eastern Australia," Jour. Geophys. Res., v. 101, n. C2, p. 3615-27.

Roemmich, D. & J. McGowan, 1995, "Climatic warming and the decline of zooplankton in the California Current," Science, v. 267, p. 1324-26.

San Diego Association of Geologists, 1982, "Geologic studies in San Diego, P.L. Abbott (ed.).

Schick, A. P., 1995, "Fluvial processes on an urbanizing alluvial fan: Eilat, Israel," p. 209-218 in J. E. Costa et al, eds., Natural and Anthropogenic Influences in Fluvial Geomorphology, Amer. Geophys. Union, Washington, D. C., 239 pp.

Schumm, S. A. and Hadley, R. F., 1961, "Progress in the application of landform analysis in studies of semiarid erosion," U. S. Geol. Survey, Circ. 437, 14 pp.

Schumm, S. A., 1977, The Fluvial System, John Wiley & Sons, New York, 338 pp.

Shepard, F.P., 1963. Submarine Geology (2nd ed.). New York: Harper & Row.

Simon, Li & Associates, 1988, "River sediment discharge study San Diego region," Coast of California Storm and Tidal Waves Study, U. S. Army Corps of Engineers, Los Angeles District, Rpt. # CCS7WS, 88-3, 38 pp.

Sommerville, R. C. J., 1996, The Forgiving Air, Understanding Enironmental Change, University of California Press, Berkeley, 195 pp.

Soutar, A. & J. D. Isaacs, 1974, "Abundance of pelagic fish during the 19th and 20th centuries as recorded in anaerobic sediment off the Californias," Fishery Bull., v. 72, p. 257-294.

Storms, J. E. A., Weltje, G. J., Van Dijke, J. J., Geel, C. R. and Kroonenberg, S. B., 2002. Process-response modeling of wave-dominated coastal systems: Simulating evolution and stratigraphy on geological timescales. Journal of Sedimentary Res., 72, 226-39.

Sunamura, T., 1992. Geomorphology of rocky coasts. New York: John Wiley.

Taylor, G. I., 1946, "Note on R. A. Bagnold's empirical formula for the critical water motion corresponding with the first disturbance of grains on a flat surface," Proc. Roy. Soc. London Jour., A, vol. 187, p. 16-18.

Thornton, E. B. and R. T. Guza, 1983, “Transformation of Wave Height Distribution,” J. Geophysical Res., vol. 88, no. C10, pp. 5925–5938,.

Tunstall, E. B. and D. L. Inman, 1975, “Vortex Generation by Oscillatory Flow over Rippled Surfaces,” J. Geophysical Res., vol. 80, no. 24, pp. 3475–3484, Aug. 1975.

Trenhaile, A. S., 1987. The Geomorphology of Rock Coasts. New York: Oxford University Press.

Trenhaile, A. S., 2002. Modeling the development of marine terraces on tectonically mobile rock coasts. Marine Geology, 185, 341-361.

Trimble, S. W., 1997, "Contribution of stream channel erosion to sediment yield from an urbanizing watershed," Science, v. 278, p. 1442-44.

U.S. Army Corps of Engineers, 1981, “Tide and tidal datums in the United States”, U.S. Army Corps of Engineers Coastal Engineering Research Center Special Report No. 7, 382 p.

U.S. Army Corps of Engineers, 1985, “Littoral zone sediments, San Diego Region, October 1983 – June 1984”, Coast of California Storm and Tidal Wave Study, CCSTWS 85-11.

U. S. Army, Corps of Engineers (USACE), 1985, “Littoral Zone Sediments, San Diego Region: Dana Point to Mexican Border, October 1983-June 1984,” Los Angeles District, CA: Coast of California Storm and Tidal Waves Study, Interim Data Report 85-11.

_____, 1991, ”State of the Coast Report, San Diego Region,” Los Angeles District, CA: Coast of California Storm and Tidal Waves Study, Final Report 1.

U.S. Department of Commerce National Ocean Service, 1986, “Tide tables 1986, high and low water predictions for west coast of North and South America”, 234 pp.

USGS, 1911, “Geology and ground waters of the western part of San Diego County, California.” USGS Water Supply Paper 446.

USGS, 1997, "USGS Digital Data Series DDS-37 at INTERNET URL," http://wwwrvares.er.usgs.gov/wgn96cd/wgn/wq/region18/hydrologic unit code.

Van Atta, C. W. and Helland, K. N., 1977, "A note on the Hurst phenomenon in turbulent flows," Water Resources Res., v. 13, n. 6, p. 1003-5.

Van Dyke, M., 1964.“Listing-Line Theory as a Singular-Perturbation Problem,” J. Applied Mathematics and Mechanics, vol. 28, pp. 90−101.

Van Dyke, M., 1975, Perturbation Methods in Fluid Mechanics. Stanford, CA: Parabolic.

Walker, D. A., 1995, "More evidence indicates link between El Niño, and seismicity," EOS, v. 76, n. 4, p. 33-35.

Wallace, J. M. and Gutzler, D. L., 1981, "Teleconnections in the geopotential height field during Northern Hemisphere winter," Monthly Weather Rev., v. 109, p. 784-812.

Wang, H. P., 1975, "Modeling an ocean pond: a two-dimensional, finite element hydrodynamic model of Ninigret Pond, Charleston, Rhode Island," Univ. of Rhode Island, Marine Tech. Rpt., #40, p. 1-58.

Weiyan, T., 1992, Shallow Water Hydrodynamics, Water & Power Press, Hong Kong, 434 pp.

Wilson, L., 1973, "Variations in mean annual sediment yield as a function of mean annual precipitation," Amer. Jour. Sci., v. 273, p. 335-349.

Wischmeier, W. D. and Smith, D. D., 1965, Predicting Rainfall-Erosion Losses From Cropland East of the Rocky Mountains, U. S. Dept. of Agriculture, Agriculture Handbook, 282 pp., Washington, D. C., p. 1-47.

Wood, F. J., 1986, “Tidal dynamics: coastal flooding, and cycles of gravitational force,” Kluwer Academic Publishers, 558 pp.

Zemansky, M. W. and H. C. Van Ness, 1966, Basic Engineering Thermodynamics, McGraw-Hill, 380 pp.

Zienkiewicz, O. C., 1971, The Finite Element Method in Engineering Science, McGraw-Hill Book Co., London.

Zhang, Y., Wallace, J. M. and Battisti, D. S., 1997, ENSO-like interdecadal variability: 1900-93, Jour. Climate, v. 10, p. 1004-20.